A HIGH-GAIN PLANAR DIPOLE ANTENNA FOR ULTRA-WIDEBAND APPLICATIONS

by

Shahin Shadrokh

Submitted in partial fulfillment of the requirements
for the degree of Master of Applied Science

at

Dalhousie University
Halifax, Nova Scotia
March 2014

Dedication

This thesis is dedicated to my beloved parents

TABLE OF CONTENTS

LIST OF TABLES

LIST OF FIGURES

ABSTRACT

In this thesis, a loaded planar dipole antenna with two staircase rectangular arms and backed by a double-layer frequency selective surface (FSS) is proposed for ultra-wideband (UWB) radar and communication systems. For bandwidth enhancement, each staircase rectangular arm is loaded with an open complementary double concentric split-hexagonal-ring resonator (LC-Tank) and a pair of chip resistors at the end. A broadband microstrip to parallel-stripline transformer (or balun) is applied as the feeding structure of the proposed antenna to provide impedance matching as well as balanced-unbalanced transition. In addition, a double-layer FSS is designed and placed at the back of the planar dipole, contributing to a significant gain enhancement with in-phase reflection for the entire operation bandwidth of the proposed antenna. The measurement results show that the proposed antenna, integrated with the double-layer FSS, operates over a frequency bandwidth from 0.65 to 3.8 GHz with return loss S11< -10 dB and exhibits highly directive radiation patterns, with gains in the range of 6.2-9 dBi.

LIST OF ABBREVIATIONS USED

CST	Computer Simulation Technology
CSSR	Complimentary Split Ring Resonator
dB	Decibels
dBm	Decibel-Milliwatts
EM	Electromagnetic
FCC	Federal Communications Commotion
FET	Field Effect Transistor
FSS	Frequency Selective Surface
Gbps	Gigabit Per Second
GHz	Gigahertz
GPR	Ground Penetrating Radar
GSM	Global System for Mobile
IEEE	Institute of Electrical And Electronics Engineers
MHz	Megahertz
MWS	Microwave Studio
PCB	Printed Circuit Boards
PEC	Perfect Electric Conductors
PIN Diode	Positive-Intrinsic-Negative Diode
PSD	Power Spectral Density
RF	Radio-Frequency
SHF	Super-High Frequency
SSR	Split Ring Resonator
UHF	Ultra-High Frequency
UWB	Ultra-Wideband
VNA	Vector Network Analyzer
VSWR	Voltage Standing Wave Ratio
WiFi	Wireless Fidelity
WLAN	Wireless Local Area Network

ACKNOWLEDGMENTS

I would like to express my most sincere gratitude to my supervisor, Dr. Zhizhang Chen, for his support, guidance, patience and suggestions throughout my research under his direct supervision in this extraordinary field. I would also like to express my appreciation to my great co-supervisor, Dr. Yiqiang Yu, for his constant support, daily supervision of my work, sharing of productive ideas, and his dedication throughout our numerous productive meetings.

As well, I wish to thank my committee members, Dr. William Phillips and Dr. Kamal El-Sankary, for their time and efforts in the process and for their valuable advice and guidance.

I would like to thank my colleagues at the RF/Microwave Wireless Research Lab for their assistance and concern throughout the program. Special thanks go to Dr. Farid Jolani for his helpful conversations with me in this project. Thanks to all faculty and staff of the ECE Department at Dalhousie University for assistance and cooperation for my studies at Dalhousie University.

Finally, I would like to thank my father for his unconditional support, and my mother, for being my motivation to better myself and for her endless love throughout my studying journey.

Chapter 1 INTRODUCTION

1.1 Ground-Penetrating Radar Applications and Challenges

Over the past couple of decades, Ground-Penetrating Radar (GPR) has become one of the most common and promising nondestructive techniques in the detection of objects buried underground. GPR has been applied in various fields, such as archeology [1], civil engineering [2], military [3], topographic mapping [4], and the maintenance of bridges, pipes, railways. The integration of fundamental principles of electromagnetic waves into the GPR systems provides cross-section images from the desired mediums, which can then be further studied. This low-cost method is sensitive to electric conductivity, magnetic permeability, and electric permittivity of mediums. As a result, it is feasible to distinguish between conductive (metal) and nonconductive (nonmetal) materials, and a variety of applications could employ this feature in different areas.

Two important attributes of GPR systems are penetration depth, which locates a buried object in the soil, and resolution, which defines the shapes of the object. In general, these attributes are dependent on the frequency used and characteristics or properties of the soil and the environment. The frequency used could range from a couple of megahertz for applications with requirements of high penetration depth, to several gigahertzes for applications whose priority is high image resolutions. Attenuation of higher frequency field signals in soil (or lossy media) is very noticeable compared with lower frequency field signals. Moreover, energy dissipation is very high in lossy mediums with high conductivity (e.g., moist soil), since the penetration depth of the transmitting signal in these mediums reduces significantly.

Most ground-penetrating radars work in the time domain and use pulses. The typical resolution and penetration depth of this class of radar systems depend on frequency, pulses, and the transmitter/receiver antennas. The other class of GPR radars works in frequency domain, which is the stepped-frequency continuous wave GPR [5]. Both time- and frequency-domain classes have the same fundamental working principles in terms of

radiating and receiving electromagnetic waves, as illustrated in Figure 1-1. However, the two classes have different inputs and post-processing algorithms.

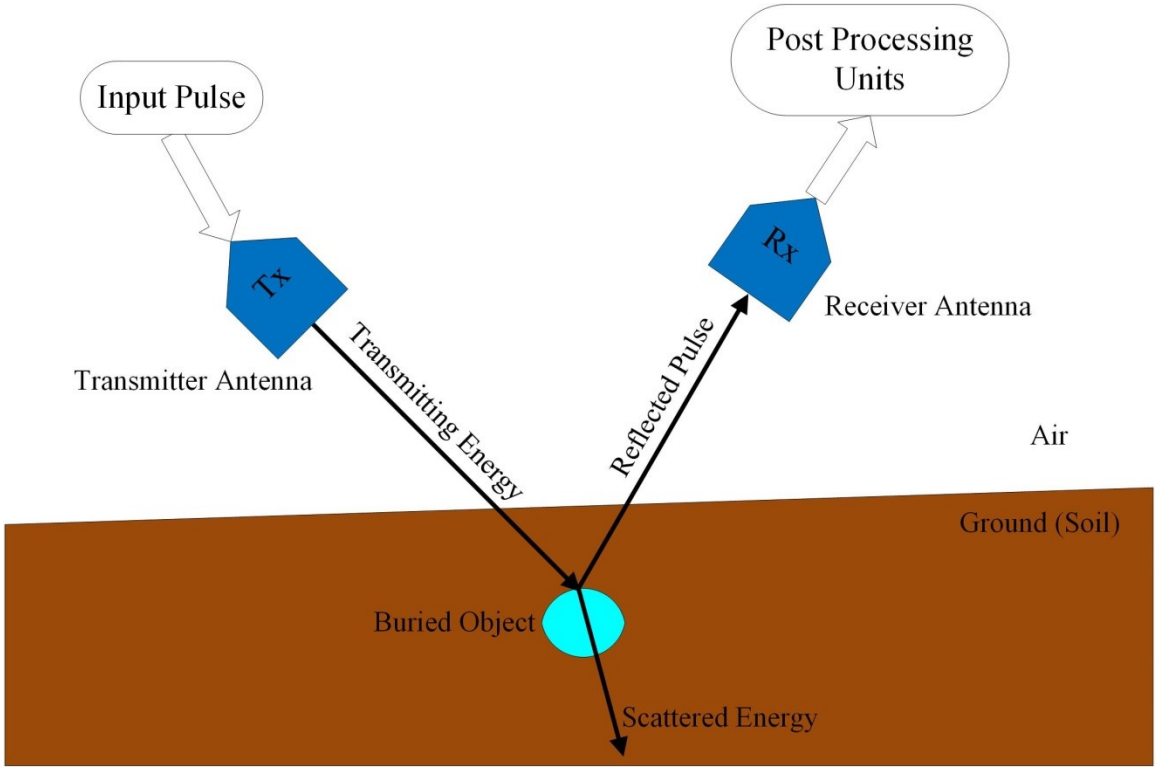

Figure 1-1 Basic schematic diagram of a time-domain GPR system

The transmitter antenna (Tx) in Figure 1-1 radiates a short electromagnetic pulse (for instance, a Gaussian pulse with a duration of a couple of nanoseconds) into the ground. A portion of the transmitted pulse is reflected on the subsurface of buried objects and the rest passes through buried objects underneath the ground until it scatters and fades away in the soil. The receiver antenna (Rx) collects reflected pulses partially and sends them to post-processing and image processing units to construct cross-section images from the objects.

In a practical example, the scenario is much more complicated and challenging when a buried object is in a lossy and nonhomogeneous medium with different electric permittivities and electric conductivities. Moreover, some objects absorb most of the transmitted pulse energy, and thus detecting them is almost impossible.

The transmitter and receiver antennas of a GPR radar system play critical roles in the functionality and overall performance of the system. In order to detect buried objects, the antenna should be capable of sending an electromagnetic pulse with an input pulse duration range of nanoseconds to avoid as much as possible late time ringing effects and echoes [6]. As a result, transmitter and receiver antennas in GPR applications should be ultra-wideband, high gain, high directivity, linear polarization, compact size, low late time ringing effect, low profile, less complexity and low fabrication cost.

1.2 Motivation for Applying Ultra-Wideband Techniques to GPR Radar Systems

Over the past two decades, ultra-wideband (UWB) technology has been increasingly employed for military radar detections and communications. Considering the numerous advantages of UWB, which are explained in this chapter, an increased demand for UWB wireless communication technology has emerged. As a result, a frequency band of 267MHz to 2655 MHz can be used for UHF (Ultra-High Frequency) applications and a frequency band of 2655MHz to 4990 MHz can be used for UHF/SHF (Super-High Frequency) applications. In February 2002, 7.5 GHz (from 3.1GHz to 10.6 GHz) of the entire bandwidth was allocated for unlicensed data communications, radars, and safety applications by the United States Federal Communications Commotion (FCC) [7].

Because UWB systems cover a large bandwidth, they have received more attention in a variety of wireless communication applications. Some important features of UWB systems are mentioned here, due to the scope of the thesis.

The first feature of the UWB systems for unlicensed wireless applications is that they are of low power systems. The power is divided across an entire operating frequency band; power density is very low and even under the noise floor limit. A rough comparison between a narrowband signal and a UWB signal is shown in Figure 1-2 [8]. Such a low

power density prevents the UWB signals from interfering the existing narrowband systems.

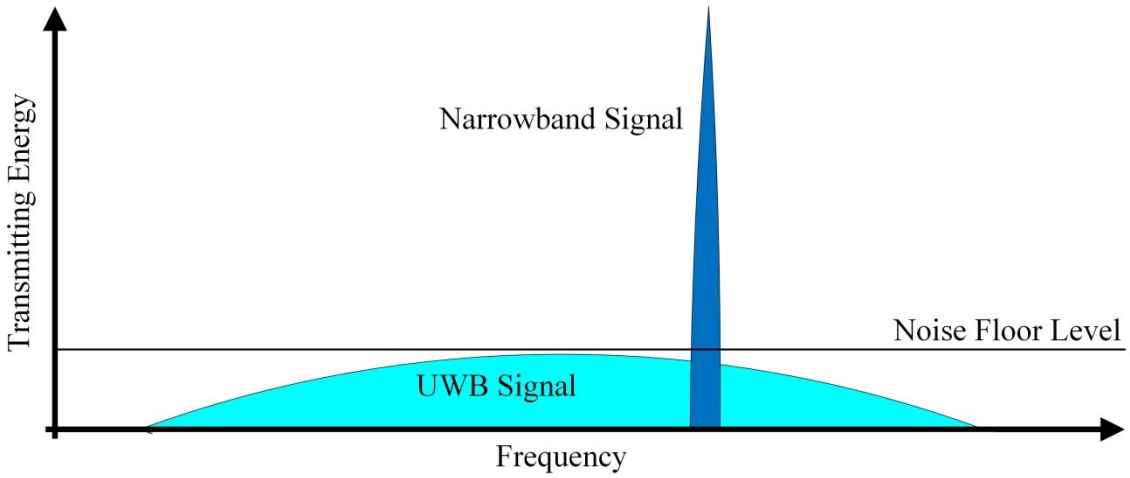

Figure 1-2 UWB energy distribution

Secondly, with a UWB system, there is a possibility to transmit the high data rate up to a few Gbps for short-range communications up to 10 meters [9]. This is due to the ultra-wide bandwidth that results in the possible high channel capacity as dictated by the Shannon-Hartley theorem.

$$C = W \times \log_2(1 + \frac{P}{N_0 \times W}) \qquad \text{Equation 1-1}$$

where C is the capacity of the channel, W is the channel bandwidth, P is the received power, and N_0 is the power spectral density of the noise [10].

In addition, UWB systems cover a large bandwidth of frequency spectrums and related pulses are in the range of nanoseconds. Thus, not only are UWB systems suitable for numerous applications in different frequency ranges, but extremely high resolution results could be obtained in terms of image processing because of narrow pulse durations.

Finally, UWB systems have low fabrication costs and are fairly lightweight. Due to the simple circuitry that may not require RF up- or down-conversion, basic UWB systems usually have less complexity and a low profile.

Taking all of this into consideration, the application of UWB techniques for GPR systems may provide solutions for increasing detection accuracy and imaging resolution whereas not sacrificing the penetration depth.

1.3 Objectives of This research

The development of an UWB GPR radar system requires a competent ultra-wideband antenna. One of the most challenging aspects of designing an ultra-wideband antenna for radar systems is to cover a wide range of frequencies whereas maintaining effective radiation of electromagnetic waves. Specific desirable properties of the antenna include linear gain, high radiation efficiency, great return loss and high directivity. Depending on applications of radar detection, additional desirable factors of the UWB antenna may include compactness, lightweight, low-profile, less complexity, and fabrication costs.

The prime goal of this research is to design a planar dipole antenna that operates in the ultra-wideband frequency range and has a compact size, stable radiation pattern, linearly increasing gain, low fabrication cost, and low profile. Ideally, a wide range of applications could use this antenna, including ground penetrating radars and short range communications. Since planar dipole antennas are naturally narrowband, techniques need to be developed to expand the bandwidth of the antenna. The second goal of this work is to design a proper wideband feeding segment. Since most existing antennas are fed via SMA connectors, a transformer is needed for the feeding part of the novel antenna to match the input impedance of the connector with the input terminal of the antenna. A third goal of this work is to make the proposed planar ultra-wideband dipole antenna highly directive and to enhance the overall gain. In doing, a double-layer frequency selective surface reflector is employed in this paper.

In this research, the proposed planar dipole antenna, wideband transformer (balun) and double-layer frequency selective surface are first simulated and designed with Computer Simulation Technology (CST) Microwave Studio (MWS) 2013. Then they are fabricated and measured in the RF/Microwave and Wireless Research Laboratory at Dalhousie University, Halifax, Canada.

1.4 Framework of the Thesis

This thesis is divided into six chapters. Chapter 2 discusses the fundamental principles, definitions and comprehensive background of ultra-wideband antenna parameters and properties. As well, several commonly used UWB antennas in literature are briefly described and their electromagnetic characteristics are reviewed.

Techniques and approaches have been developed in literature to improve and optimize the performance of the ultra-wideband antenna. Therefore, Chapter 3 covers the methodology and techniques used in this thesis. Chapter 4 introduces the proposed design with computed geometry parameters based on the techniques introduced in Chapter 3. Theoretical and experimental simulation and measurement results are shown in Chapter 5 to validate the performance of the proposed system. Finally, Chapter 6 concludes the obtained results from the previous chapter and highlights important improvements of the proposed designs. In addition, possible directions to extend this project for future work are pointed out.

Chapter 2 BACKGROUND AND LITERATURE REVIEW

2.1 Definition of Ultra-Wideband

According to the Federal Communications Commission (FCC) [11], ultra-wideband (UWB) is considered as any wireless communications technology that occupies 500MHz or more of absolute bandwidth or greater than 20% of the operating center frequency F_c .

$$F_c = \frac{F_l + F_h}{2} \qquad \text{Equation 2-1}$$

The operating bandwidth of an antenna is limited by the low point F_l and high point F_h, and the radiation emission outside the band is 10dB lower than that inside. The fractional bandwidth is defined in the equation below:

$$Fractional\ Bandwidth = 2 \times \frac{F_l - F_h}{F_l + F_h} \qquad \text{Equation 2-2}$$

In order to avoid communication interference scenarios, UWB applications have the restricted radiation power mask as defined by the FCC. The FCC mask for indoor and outdoor applications is shown in Figure 2-1, which shows measured emission level [dB] versus frequency [GHz] [12].

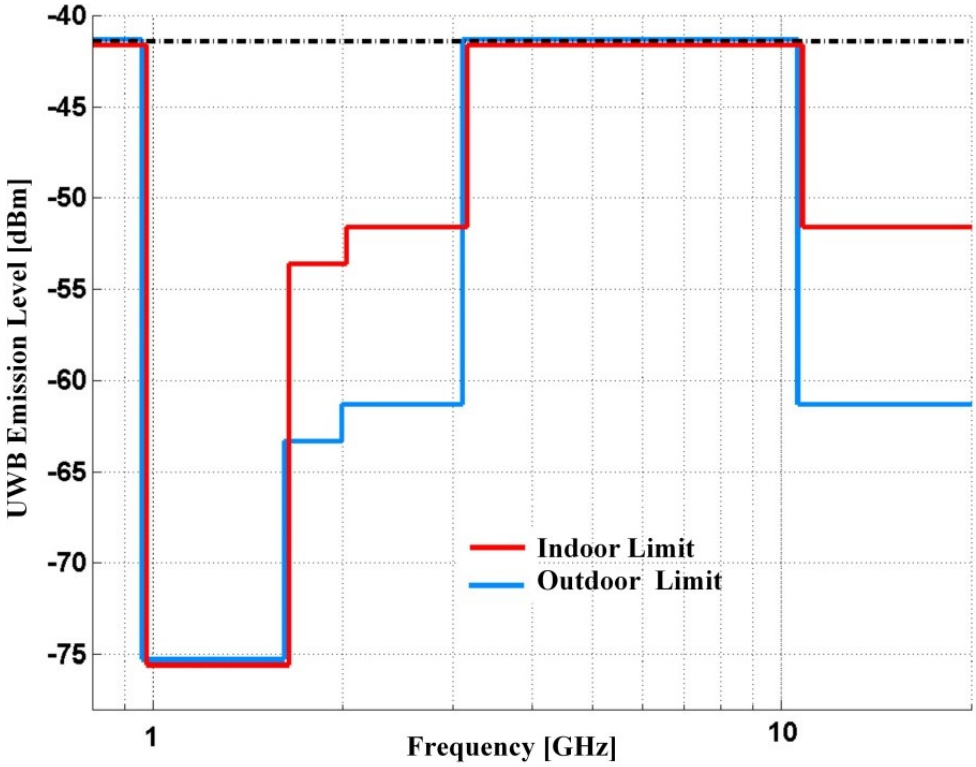

Figure 2-1 FCC mask for indoor and outdoor applications

In the FCC defined UWB for unlicensed applications, the maximum permitted power spectral density (PSD) for both indoor and outdoor UWB applications is –41.3 dBm/MHz for frequencies below 0.96 GHz and also from 3.1 to 10.6 GHz, respectively. The PSD from 0.96 to 1.66 GHz is below –75 dBm/MHz for both indoor and outdoor applications. In addition, From 1.66 to 3.1 GHz and at the frequency higher than 10.6GHz, the PSD should be below –51.3 dBm/MHz and –61.3 dBm/MHz for indoor and outdoor UWB systems, respectively. By having such low power levels, the UWB systems are not expected to interfere with the existing radio systems. However, it should be noted for licensed or other specifically defined UWB applications including the ground penetrating applications, such low power requirement may not necessary all the times.

2.2 Maxwell's Equations

In 1864, the fundamental theory of electromagnetic waves, based on the relation between electric and magnetic fields, was introduced by J.C. Maxwell with a well-known series of equations, named as Maxwell's equations. Maxwell's equations consist of Faraday's law, Ampere's law, Gaussian's law and magnetic field law [13] [14], which can be employed to solve and compute electromagnetic problems, current distribution, electromagnetic waves propagation, etc. The differential forms of Maxwell's equations are shown below:

$$\nabla \times E = \frac{\partial B}{\partial t} \qquad \text{Equation 2-3}$$

$$\nabla \times H = J + \frac{\partial D}{\partial t} \qquad \text{Equation 2-4}$$

$$\nabla \cdot B = 0 \qquad \text{Equation 2-5}$$

$$\nabla \cdot D = \rho_v \qquad \text{Equation 2-6}$$

where E is the electric field intensity vector (V/m), H represents the magnetic field intensity vector (A/m), B stands for the magnetic flux density vector (Wb/m^2), D shows the current displacement vector (C/m^2), J is the electric current density vector (A/m^2), and ρ_v is the electric charge density (C/m^3). Electric permittivity ε (F/m), magnetic permeability μ (H/m) and conductivity σ (S/m) link the flux density and field intensity in the above equations:

$$D = \varepsilon E \qquad \text{Equation 2-7}$$

$$B = \mu H \qquad \text{Equation 2-8}$$

$$J = \sigma E \qquad \text{Equation 2-9}$$

By assuming time dependence $e^{j\omega t}$ for Faraday's law, Equation 2-3, and magnetic field law, Equation 2-5, a harmonic plane wave equation for a lossy and source-free medium can be obtained as:

$$\nabla^2 E(\mathrm{r},\omega) + k^2 E(\mathrm{r},\omega) = 0 \qquad \text{Equation 2-10}$$

$$k = \omega\sqrt{\mu\varepsilon} \qquad \text{Equation 2-11}$$

where k is the wave number that defines the propagation direction. The wave number k and permittivity ε are the complex values in a lossy medium. The imaginary part of k defines the attenuation constant while the real part defines the phase constant.

2.3 Fundamental Characteristics of UWB Antennas

In order to design a suitable ultra-wideband antenna for a specific application, it is necessary to understand the fundamental characteristics and properties of UWB antennas. Accordingly, the basic antenna parameters, such as impedance bandwidth, voltage standing wave ratio, directivity, efficiency, gain, radiation pattern and half-power bandwidth, are explained in this section.

2.3.1 Impedance Bandwidth

The impedance bandwidth of an antenna is the range of operating frequency where 90% or more of the input power at the input terminal of the antenna is radiated and 10% (or less) of the incident pulse is lost due to unwanted reflections. The reason behind the reflections (loss) is mismatching between the transmission line impedance and the antenna input impedance. Therefore, when designing an antenna, matching should be taken into account, with the aim of having less reflectivity and radiating of the most energy via the antenna.

The voltage reflection coefficient Γ corresponds to the return loss S_{11} of the antenna and characterizes the Voltage Standing Wave Ratio (VSWR) (see Figure 2-2). The voltage reflection coefficient can be measured with a Vector Network Analyzer (VNA) and also can be related to the impedances of the transmission line and antenna as described by Equation 2-12:

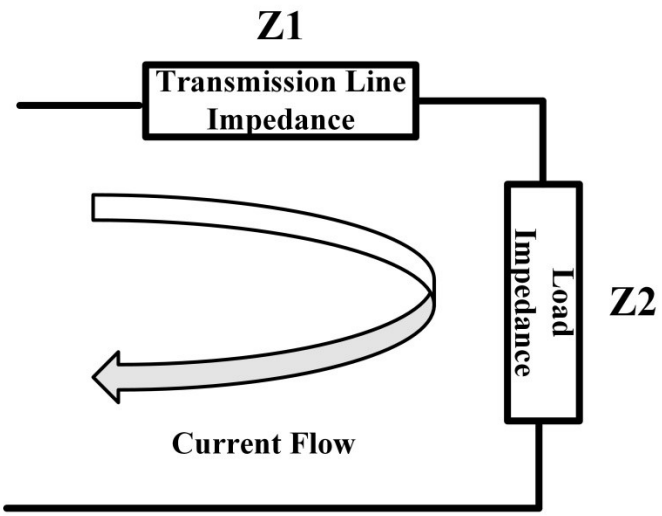

Figure 2-2 Equivalent circuit of antenna in terms of impedance

$$\Gamma = \frac{Z_1 - Z_2}{Z_1 + Z_2} \qquad \text{Equation 2-12}$$

where Z_1 is the transmission line impedance and Z_2 is the antenna input impedance. In an ideal case, the transmission line is matched with the antenna, and hence, $\Gamma = 0$. However, in reality, it is not the case. The worst case is when $\Gamma = 1$ or $\Gamma = -1$, in which the transmission line sees the antenna impedance as an open circuit or short circuit, respectively.

In dB,

$$\Gamma_{dB} = 20 \times log_{10}(|\Gamma|) \qquad \text{Equation 2-13}$$

$$Return\ Loss = -20 \times log_{10}(|\Gamma|) \qquad \text{Equation 2-14}$$

The absolute value of voltage reflection coefficient in dB can be defined as shown by Equation 2-13, or, in a more common way, as return loss, as shown by Equation 2-14.

2.3.2 Voltage Standing Wave Ratio (VSWR)

In antenna designing, the voltage standing wave ratio (VSWR) corresponds to antenna efficiency and performance. VSWR is expressed as the ratio of the maximum standing wave amplitude over the minimum standing wave amplitude.

In reality, transmission line impedance and antenna impedance do not perfectly match and the value of the voltage reflection coefficient is not zero. Therefore, a reflected wave flows backward from the load to the transmission line and causes undesired standing waves in the transmission line. Therefore, VSWR is related to the reflection coefficient as determined by Equation 2-15.

$$VSWR = \frac{1+|\Gamma|}{1-|\Gamma|} \qquad \text{Equation 2-15}$$

Depending on the system and antenna specifications, an acceptable numerical value is typically from 2.0 to 2.5 (or less) for the voltage standing wave ratio.

2.3.3 Directivity

In a non-isotropic power source, directivity is defined as a ratio between the radiation intensity over that by an isotropic source is known. In other words, and according to IEEE standards [15], "the ratio of the radiation intensity in a given direction from the antenna to the radiation intensity averages over all directions. The average radiation intensity is equal to the total power radiated by the antenna divided by 4π . If the direction is not specified, the direction of maximum radiation intensity is implied." Directivity D can be calculated from Equation 2-15.

$$D = \frac{U}{U_0} = \frac{4\pi}{P_{rad}} \qquad \text{Equation 2-16}$$

$$P_{rad} = \oiint_{\Omega} U_0 d\Omega = U_0 \oiint_{\Omega} d\Omega = 4\pi U_0 \qquad \text{Equation 2-17}$$

where U is the radiation intensity (*W/unit solid angle*) in Equation 2-16, and P_{rad} is the total radiated power intensity from an antenna in Equation 2-17. Thus, the radiation intensity of a desired antenna is the result of the directivity, gain, and efficiency of the antenna.

2.3.4 Efficiency

The total radiation efficiency of an antenna is defined as a multiplication of the reflection efficiency and radiation efficiency, as in Equation 2-18.The first factor is the radiation efficiency $\eta_{rad.}$, which takes the conduction efficiency and dielectric efficiency into account, and can be calculated through to Equation 2-19. The second factor to determine the total efficiency is the reflection efficiency $E_{ref.}$, which is related to the voltage reflection coefficient Γ of the antenna, as computed in Equation 2-20 [15].

$$\eta_{total} = \eta_{rad.} \times \eta_{ref.} \quad \text{Equation 2-18}$$

$$\eta_{rad.} = \frac{P_{rad.}}{P_{input}} \quad \text{Equation 2-19}$$

$$\eta_{ref.} = 1 - |\Gamma|^2 \quad \text{Equation 2-20}$$

where $P_{rad.}$ is the power radiated from the antenna and P_{input} is the input power at the antenna terminals point.

2.3.5 Gain

Antenna gain is to measure the performance of an antenna in concentrating energy in a narrow directive angular region [16]. According to the IEEE standard definition [17], gain in an antenna can be defined as "the ratio of the intensity, in a given direction, to the radiation intensity that would be obtained if the power accepted by the antenna were radiated isotropically". Antenna gain is directly related to the efficiency and directivity of the antenna and can be written mathematically as Equation 2-21:

$$G = e_{rad} D = 4\pi \frac{U(\theta,\phi)}{P_{in}} \text{ (dimensionless)} \quad \text{Equation 2-21}$$

This equation simply calculates the radiation intensity of the antenna over the total input power at the terminal of the antenna. Equation 2-21 is dimensionless, and the term "gain" is generally referred to the maximum gain at the direction of the maximum radiation of the antenna.

2.3.6 Radiation Pattern

In studying attributes and characteristics of an antenna, radiation patterns describe how an antenna radiate in different directions which can be measured by power flux density, radiation intensity, field strength, directivity, phase and polarization [17]. Thus, radiation patterns can determine if an antenna is suitable for a desired application. For instance, antennas employed in Wi-Fi rotors are omnidirectional because location of receivers in the network towards the antenna is unknown. Thus, the antenna should be capable of radiating energy in all directions. On the other hand, for applications like radars and ground penetrating radars where the location of an object is generally known, the antenna should be highly directed to radiate towards the objects and achieve a maximum radiation range and penetration depth.

Based on the IEEE standard definition [15], an antenna radiation pattern is explained as: a mathematical function or a graphical representation of the radiation properties of the antenna as a function of space coordinates. In most cases, the radiation pattern is determined in the far-field region and is represented as a function of the directional coordinates.

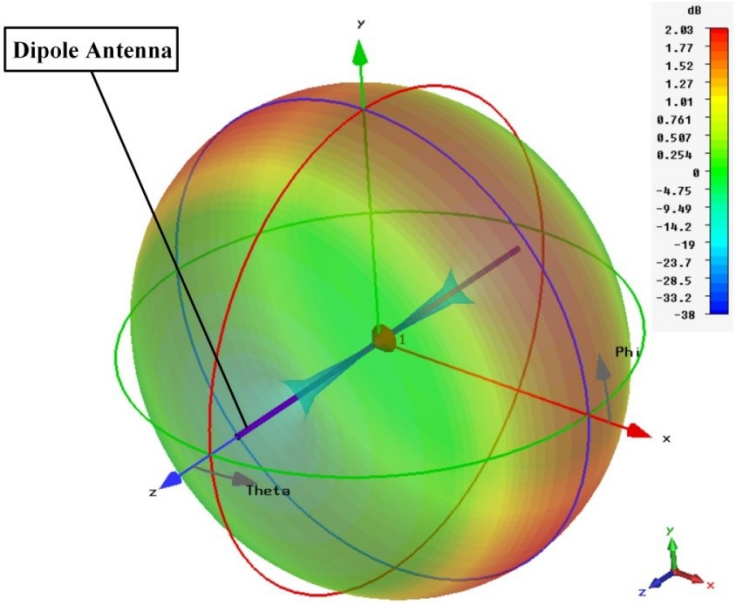

Figure 2-3 3D radiation pattern of a rod dipole antenna

A radiation pattern of an antenna can be illustrated in three-dimensional plots, according to the spherical coordinate system. In Figure 2-3, a simple dipole antenna is orientated along the z-axis and centered at the interception of the *x*, *y* and *z* coordinates. A radiation pattern can also be shown in a two-dimensional polar plot or a plane in a variety of working frequency bands of antennas. In Figure 2-3, the *x*-*z* plane in a spherical system is considered as the E-cut plane as the electric fields generated by the dipole lie on the plane. The radiation pattern on this plane is shown in Figure 2-4(a). The *x*-*y* plane in the spherical system is considered as the H-cut plane as the magnetic fields generated by the dipole lie on the plane. The radiation on this plane is shown in Figure 2-4(b) [18].

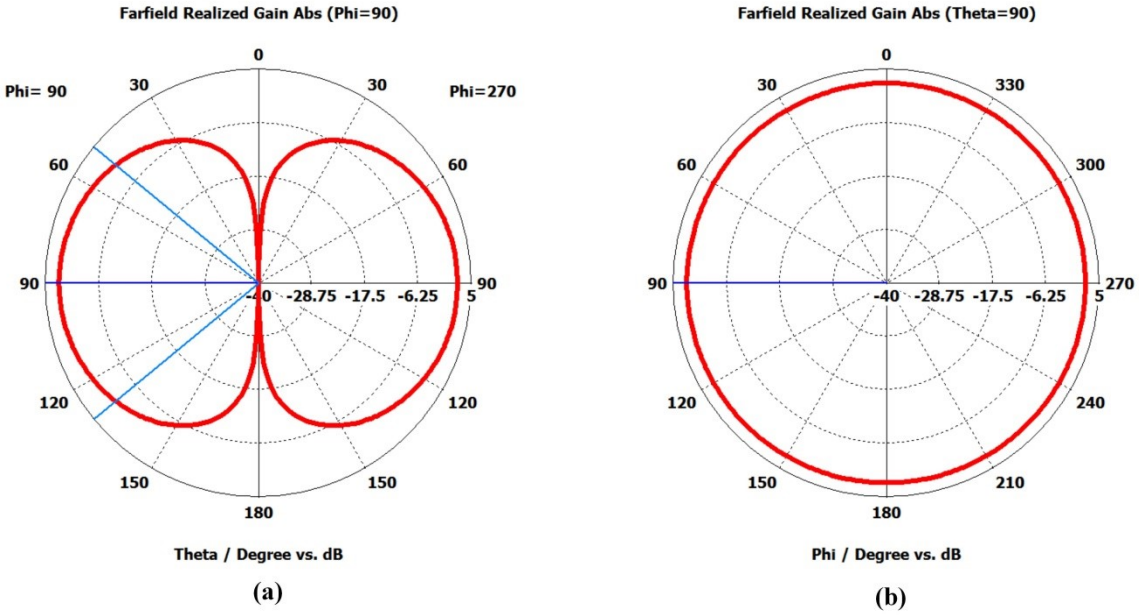

Figure 2-4 2D-Polar plots of a rod dipole antenna (a) E-cut and (b) H-cut

As illustrated in Figure 2-4(a), the electric field (E-cut) has a maximum radiation power on the *x*-*z* plane, where θ is changing and $\varphi = 0^o$. As well, there are two nulls along the *z*-axis, which represent the open ends of the dipole antenna. The *x*-*y* plane contains the magnetic field (H-cut) of the dipole antenna, where $\theta = 90^o$ and φ is changing.

2.3.7 Half-Power Beamwidth

According to the IEEE standard definition, half-power bandwidth is where, "in a plane containing the direction of the maximum of a beam, the angle between the two directions in which the radiation intensity is one-half value of the beam" [15]. The two directions are corresponding to 3 dB less than the main beam in power density and separated from each other an angular distance. Half-power beamwidth can be obtained mathematically with Equation 2-22.

$$Half-Power\ Beamwidth = \frac{k\lambda}{D} \qquad \text{Equation 2-22}$$

where k is a proportionality constant known as the beamwidth factor, λ is the wavelength of a desired frequency, and D is the aperture dimension of the antenna [16]. Figure 2-4(a) shows the angular beamwidth (79 degree) of a dipole with two blue lines. Here, the half-power beamwidth is directly related to the aperture of antenna. The half-power beamwidth not only decides how wide an antenna can radiate effectively, but also characterizes the antenna in terms of directivity.

2.4 Conventional UWB Antennas

In this section, a brief review of classical and commonly used ultra-wideband antennas for wireless communications, radars and ground-penetrating radars is presented. Several popular UWB antennas have been developed and reported in the open literature and they are reviewed in this section. Of the so-called conventional UWB antennas, the Monopole, the Dipole, the Spiral, the Log-periodic, the Vivaldi and the horn antennas are presented. Then, based on the required specifications for our research, a good candidate is selected as the starting point of the proposed antenna.

2.4.1 Monopole Antenna

A simple form of a monopole antenna is a straight wire of finite length that is located above a ground plane. In Figure 2-5, a straight-wire monopole antenna with a finite

length and an open-end arm is illustrated. In general, monopole antennas have linear polarization and an omnidirectional radiation pattern in the horizontal plane. Ideally, for a perfect monopole configuration, the wire is located above an infinitely large ground plane. The radiation pattern of a monopole antenna is thus above the x-y ground plane and one-half of a sphere, due to the ground plane.

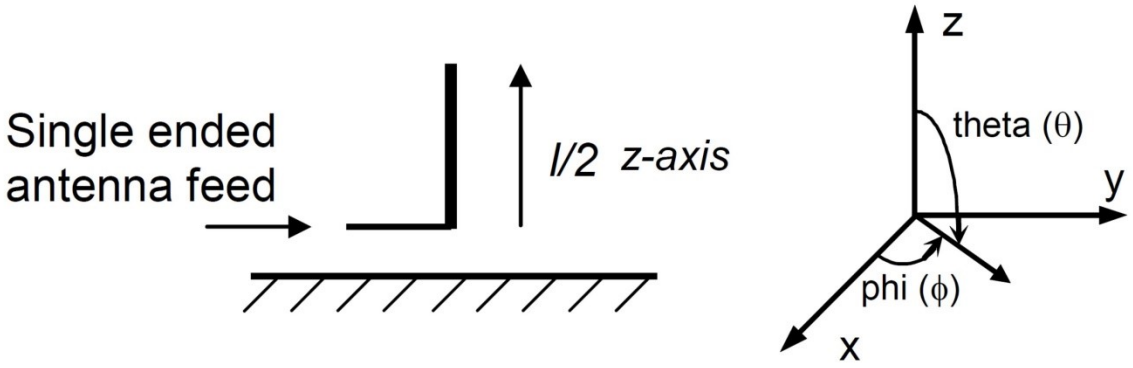

Figure 2-5 Straight wire monopole antenna [19]

In this example, the monopole antenna is excited with a sinusoidal pulse. The current flows along the wire through the feeding point, where the current distribution is not constant due to the characteristic of the input pulse. This oscillated current creates an electromagnetic field around the wire. The antenna pattern factor $F(\theta)$ is mathematically calculated in Equation 2-23:

$$F(\theta) = \frac{\cos\left(\frac{1}{2} kl\cos(\theta)\right) - \cos\left(\frac{1}{2} kl\right)}{\sin\theta} \qquad \text{Equation 2-23}$$

$$k = \frac{2\pi}{\lambda} \qquad \text{Equation 2-24}$$

where k is the wave number and l is the length of the wire. Thus, it is clear that the physical length of a monopole antenna and wavelength have critical compacts on the antenna pattern factor.

The introduced monopole antenna is a three-dimensional structure, which makes it less than ideal for applications with size and weight restrictions. In order to make the

monopole antenna structure planar (two-dimensional) and low profile, a planar monopole antenna was introduced. In Figure 2-6, a planar monopole antenna printed on a FR4 substrate with microstrip feeding is fabricated and shown.

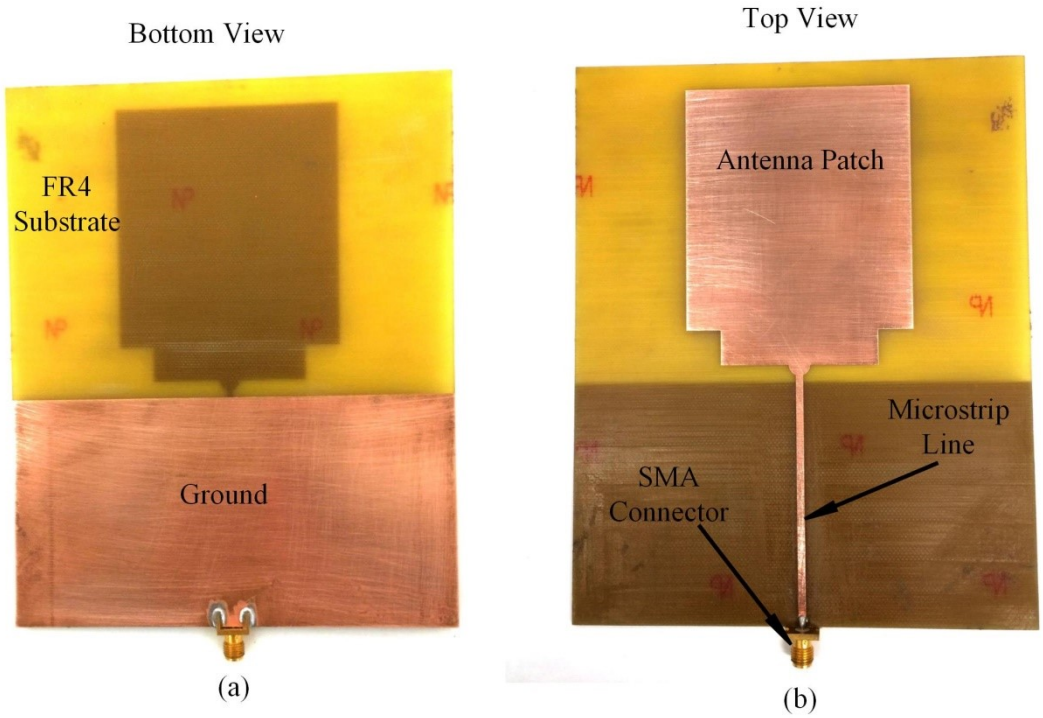

Figure 2-6 Fabricated planar monopole antenna

The physical length of a planar monopole antenna is often normalized by the wavelength of the lowest operation frequency. The ratio is called electrical length. The electric length of the planar monopole antenna depends on the electromagnetic properties of the antenna's substrate. The antenna wavelength is calculated by Equation 2-27 [20].

$$e_{eff} = \frac{e_r + 1}{2} + \frac{e_r - 1}{2}\left(\frac{1}{\sqrt{1 + \frac{12h}{w}}} + 0.04\left(1 - \frac{w}{h}\right)^2 \right) \qquad \text{Equation 2-25}$$

$$v_p = \frac{c}{\sqrt{e_{eff}}} \qquad \text{Equation 2-26}$$

$$\lambda = \frac{c}{f\sqrt{e_{eff}}}$$ Equation 2-27

where ε_{eff} is the effective permittivity that depends on the surrounding circumstances and the length, and width of the wire. v_p is the phase velocity, ε_r and μ_r are the relative permittivity and permeability of the substrate, respectively.

2.4.2 Dipole Antenna

The basic form of a dipole antenna is two straight wires of finite length, fed from the center. In Figure 2-7, two straight wire dipole antennas with a finite length and open-end arms are illustrated. Typically, dipole antennas have linear polarization and are capable of covering a wider bandwidth of operation frequency.

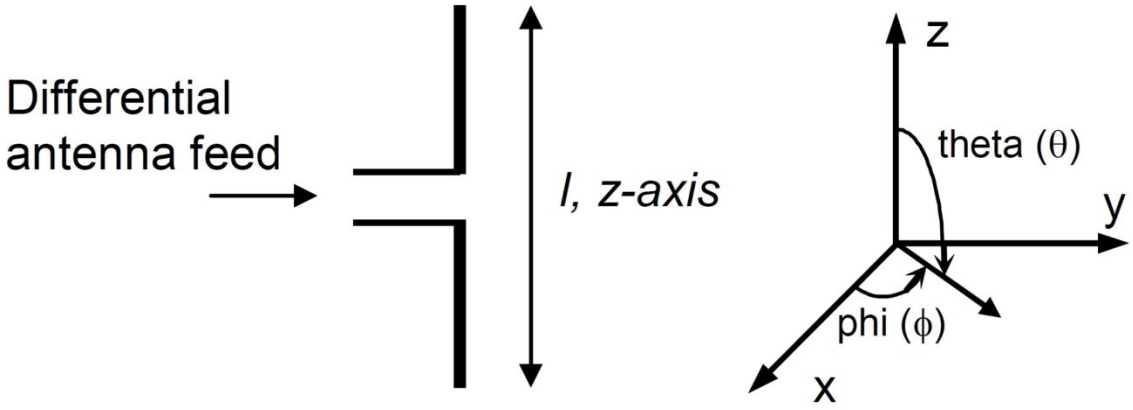

Figure 2-7 Straight-wire dipole antenna [19]

The two arms of the dipole antenna are identical and the feed is located at the center. Therefore, the phase distribution on each conductive arm of the dipole is constant, and the open end is seen as an open circuit from the feeding terminal. In an ideal situation, the current reaches zero at the open end of the arms. Radiation from each segment of the antenna arms has different phase delays, due to the physical length of the arms [20]. The same principles as planar monopole antennas can be applied to obtain the wavelength of the planar dipole. The antenna pattern factor $F(\theta)$ can be calculated from Equation 2-23.

Figure 2-8 illustrates a simulated planar dipole antenna on a single-sided substrate. In this design, the antenna is fed from the center of the substrate, as shown in Figure 2-8(a). Planar dipole antennas typically have a pair of symmetrical arms.

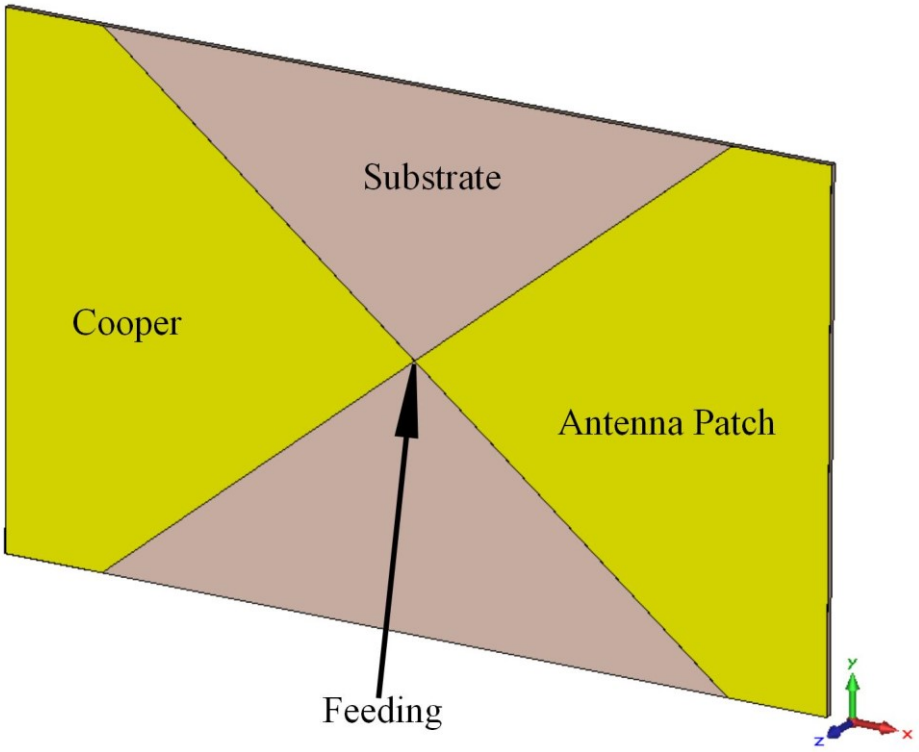

Figure 2-8 Planar dipole antenna

2.4.3 Spiral Antenna

The spiral antenna is a sub category of ultra-wideband antennas with relatively higher input impedance compared to dipole and monopole antennas. Spiral antennas are divided into two categories: two-dimensional (planar spiral antenna) and three-dimensional (helical spiral antennas). In general, these types of antennas have a wide operating bandwidth with a circular polarized radiation. For a planar spiral antenna, the inner and outer circumference of each leg of the spiral antenna determines the radiation properties of the antenna. Furthermore, the electric size of each leg should be long enough to provide a circumference with a length equal to two wavelengths or more.

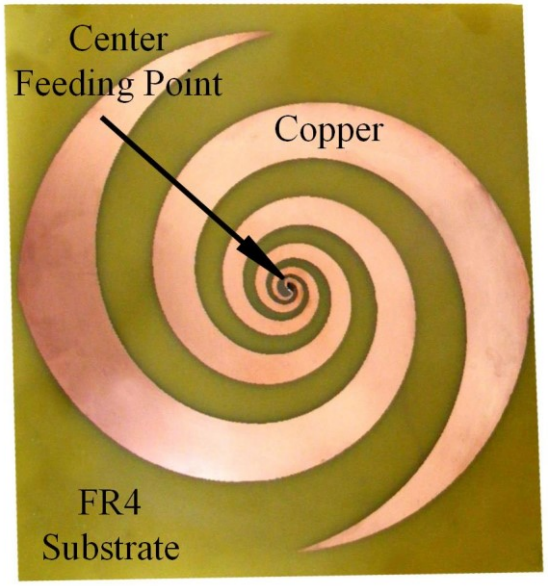

Figure 2-9 Fabricated planar equiangular spiral antenna

Figure 2-9 shows a planar spiral antenna on an FR4 substrate. It has a low profile design, compact size, and ultra-wideband characteristics. However, despite having some suitable characteristics for our application as well as low pulse distortion for transmission and receiver, spiral antennas are ultimately not good candidates for radar applications. The main drawback is their circular polarization characteristic. When the current flows along the spiral legs, the higher operating frequencies are radiated first due to having shorter wavelengths, after which the lower operating frequency range is radiated due to having longer wavelengths [21]. This lapse creates dispersions in the radiated pulse, thus making spiral antennas unsuitable for our purposes.

2.4.4 Log-Periodic Antenna

A proper design of a log-periodic antenna [22] provides an ultra-wideband operating band with uniform radiation behavior. Most log-periodic antennas have linear polarization and bidirectional radiation patterns. In order to design a UWB log-periodic antenna, the antenna's teeth should be calculated logarithmically to have uniform current

distribution and resonance frequencies corresponding to each half wavelength of the teeth. This type of antenna can be printed on a substrate to have a planar structure, low profile, and lightweight structure with a compact size.

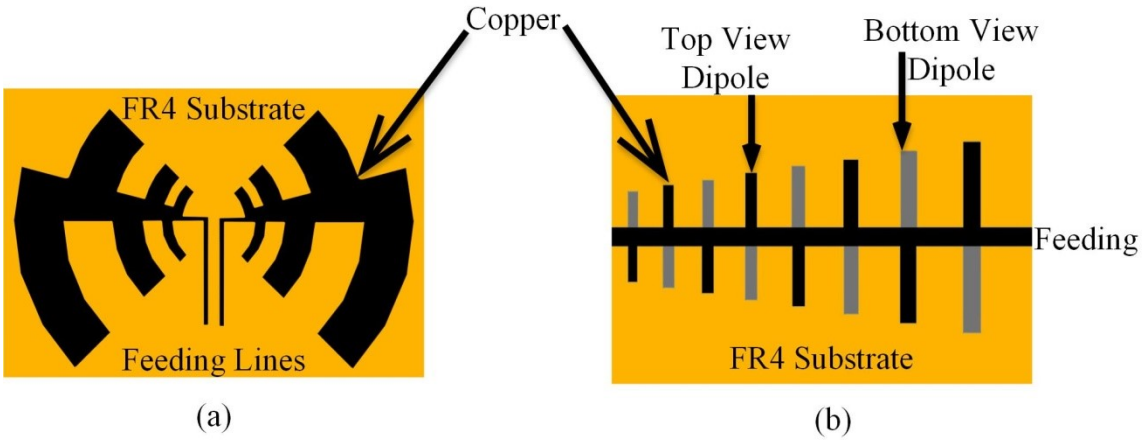

Figure 2-10 (a) Planar Log-periodic antenna with curved teeth and (b) planar Log-periodic with straight teeth [23]

Circularly curved teeth and a dipole array of planar log-periodic antennas [24] are depicted in Figure 2-10(a) and (b), respectively. As can be seen, the antenna teeth are printed on a substrate, with increasing distance and length between each adjacent tooth to create a uniform resonance frequency. The lowest resonance frequency in the antenna will correspond to the longest physical length of teeth, and the highest resonance frequency will occur due to the shortest physical length of teeth.

Even though the log-periodic antenna has some advantages, as mentioned above, and is also linearly polarized (unlike spiral antennas), log-periodic antennas do not cover a broad frequency range as spiral antennas do [6].

2.4.5 Vivaldi Antenna

The Vivaldi antenna is a planar slot antenna. It could have the forms of the coplanar Vivaldi antenna [25], the antipodal Vivaldi antenna [26] and the balanced antipodal Vivaldi antenna [27]. For all three Vivaldi antennas, their exponential tapered slot lines

create flare angles to cover a wide bandwidth of frequency, and the flat edges play a main role in creating radiation [28]. However, the antenna patch for the coplanar Vivaldi antenna is located on one side of the substrate, which makes it difficult to feed and match the input impedance of the antenna with a 50Ω SMA connector, as shown in Figure 2-11(a).

In response to this issue, the antipodal Vivaldi antenna with two patches on both sides of the substrate in opposite directions was introduced. This antenna is fed via microstrip to the double strip transmission line, with the aim of compromising the coplanar Vivaldi feeding issue, as shown in Figure 2-11(b). In designing a balanced antipodal Vivaldi, a second substrate is added on top of an antipodal Vivaldi that sandwiches the top patch between the two dielectric substrates. The same patch as the bottom patch is printed on top of the new substrate, as depicted in Figure 2-11(c). This technique is employed to suppress undesirable cross-polarized radiation in radar and communication applications.

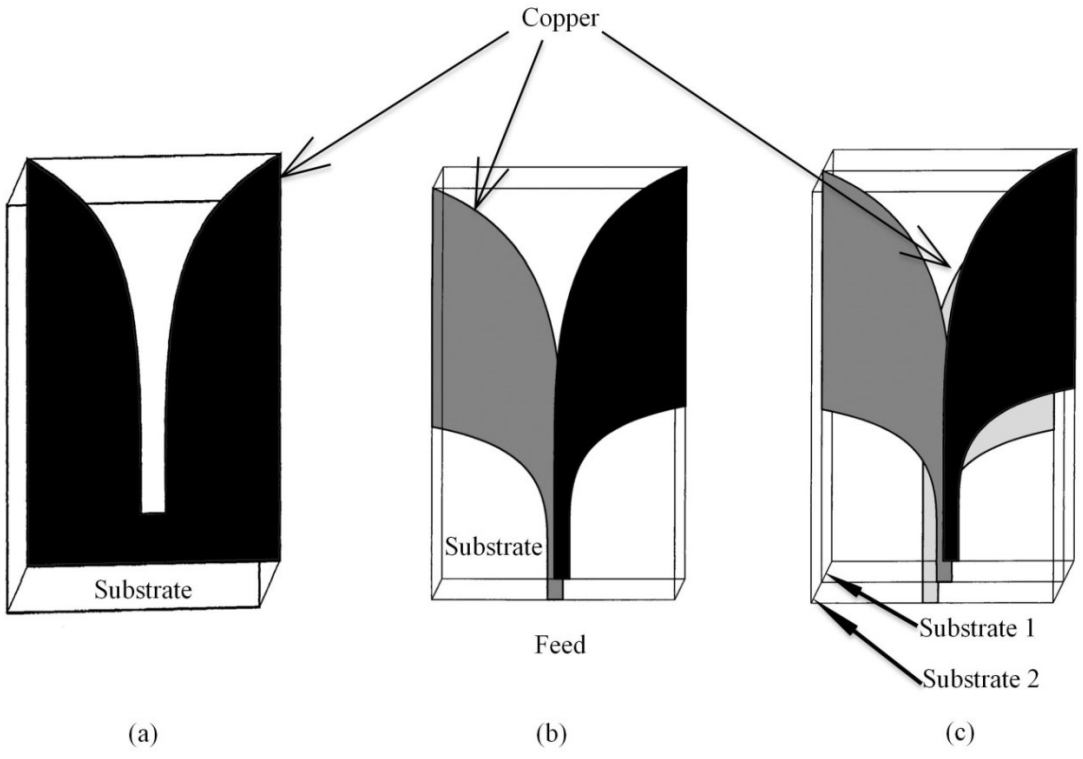

Figure 2-11 Three designs of the Vivaldi antenna [29]

Despite the fact that Vivaldi antennas have high directivity, a stable radiation pattern, acceptable group delay, and almost flat gain, they still suffer from a high rate of cross-polarization and feeding issue, which adversely reflects on the performance of the antennas and operating bandwidth.

2.4.6 Horn Antenna

The horn antenna is one of the most common antennas used in telecommunication engineering and subsurface probing. In these antennas, multiple cross-sections and ridge designs are flared to a wide opening, achieving linearly polarized broadband properties, very large gain and directive radiation patterns. Furthermore, horn antennas are capable of transmitting very narrow pulses due to its broadband characteristic, which makes them a potential candidate for radars and ground-penetrating radars. In Figure 2-12, a double-ridge horn antenna with an operational frequency of 700 MHz to 18 GHz and a gain range of 1.4 to 15 dBi is shown in Figure 2-12.

Figure 2-12 A Double-ridge horn antenna

Although horn antennas have suitable properties for most radar applications, they have high fabrication cost and are bulky; so they are not commonly used in commercial radar applications. The second drawback of horn antennas is the high rate of cross-talking between them and the ground, which increases the intensity of the late time ringing effect.

After having reviewed the electromagnetic characteristics and properties of the UWB antennas briefly described above in search of a suitable candidate for ground penetrating radar and short range communication applications, we consider a planar dipole antenna as a good starting point for our design.

Chapter 3 METHODOLOGY AND TECHNIQUES FOR UWB ANTENNA PERFORMANCE ENHANCEMENT

The methods and approaches reported in the literature for designing ultra-wideband planar antennas are discussed and presented in this chapter. These methods have been applied in order to enhance the performance of the planar antenna to its optimal point. First, the stepped notch technique is implemented to increase the bandwidth of a narrowband planar dipole antenna. Secondly, inductance and capacitance loading approach is employed to create additional resonance frequency in order to obtain a greater return loss for the antenna. Then, a double-layer Frequency Selective Surface (FSS) reflector is integrated with the antenna structure to increase antenna gain and directivity towards a desired target or object. Finally, a balun structure is presented for the feed of the planar dipole antenna to match the terminal connection with the input impedance of the antenna. These techniques are elaborated in the following sections.

3.1 Stepped Notches in Planar Dipole Antenna for Bandwidth Enhancement

Among all UWB antennas, planar structures, and specifically planar dipole antennas, have attracted considerable attention due to their low profile, broad bandwidth, flat gain, directive characteristic, simple structure, light weight, and low fabrication cost for wireless communication systems. In this thesis, a planar dipole antenna is selected for its potentials to enhance the performance compared to other planar antennas briefly reviewed in Chapter 2 such as planar monopole, Vivaldi, spiral and log-periodic antennas. A planar monopole antenna has a relatively low gain and an asymmetric radiation pattern. The planar dipole antenna with broadband capability has been studied in detail in the literature, and the advantages of this type of antenna are well known. Nevertheless, a simple printed dipole antenna without any modifications has a narrow frequency band. In addition, keeping the electrical size of the antenna small and

electromagnetic properties of the antenna (such as efficiency, gain, directivity, and radiation pattern) unchanged or even improved is also very challenging.

One technique for expanding antenna bandwidth is to use electrical or mechanical switching. In this approach, active components (e.g., PIN diodes, GaSa FET and RF microelectromechanical [30] systems) are integrated with the design of the antenna. The results for active components are promising for enhancing bandwidth, but it has drawbacks for radar applications. The late time ringing effect increases significantly, which leads to a poor image processing for the post-processing units.

Another approach for enhancing antenna bandwidth is to employ parasitic patches [31] and integrate them with radiating element of an antenna. This technique uses parasitic elements around the antenna patch and increases the operating bandwidth of the antenna significantly. The working principle for increasing the bandwidth is a mutual coupling between the radiating element of the antenna and parasitic patches that lower the Q value of the antenna. Additionally, in this mutual coupling, the current distribution on the antenna's radiator is manipulated, and with a proper design and geometry size of parasitic elements, additional resonance will be created [32]. The main disadvantages of parasitic patches techniques are increased size of the antenna structure, which is not ideal for applications with size restrictions. This technique also adds more complexity to the configuration of the antenna.

One of the most commonly used techniques for achieving maximum impedance bandwidth is to apply notches at proper locations of the radiating arm of the antenna. In this approach, electromagnetic coupling between the radiating element and the ground changes the surface current flow and lower Q value. Thus, by properly implementing the notches, the input impedance of the antenna can be matched in order to cover more bandwidth.

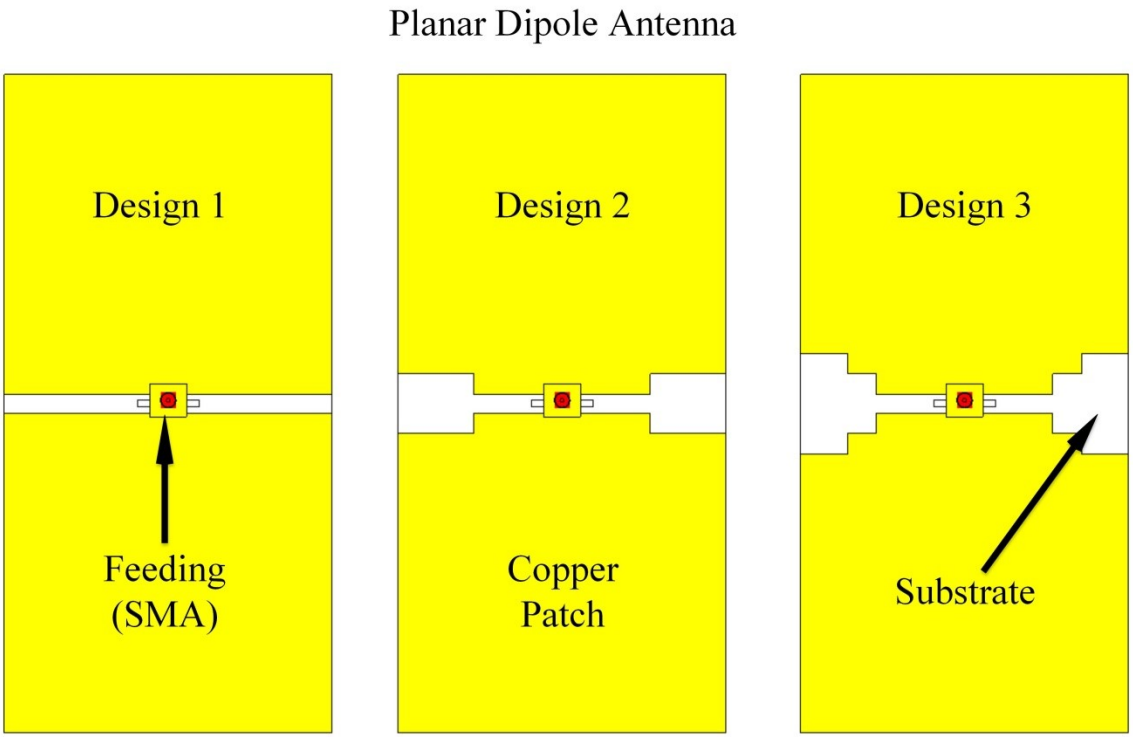

Figure 3-1 Three designs of the planar dipole antenna

Figure 1 shows the three designs of the planar dipole antenna. In Figure 3-1, design 1 shows a planar rectangular dipole antenna printed on a dielectric (in this example, FR4) substrate, where it is fed from the center via a 50Ω SMA connector. In Figure 3-1, design 2 has the same geometric size and layout as the first design, but a pair of notches has been etched out from each center corner of the dipole's arm. Finally, the third design has an identical geometry as the previous two designs, but the lower part of each arm towards the center of the dipole is shaped in a staircase manner, with step increments chosen for bandwidth enhancement and size reduction. These steps are absent in designs 1 and 2.

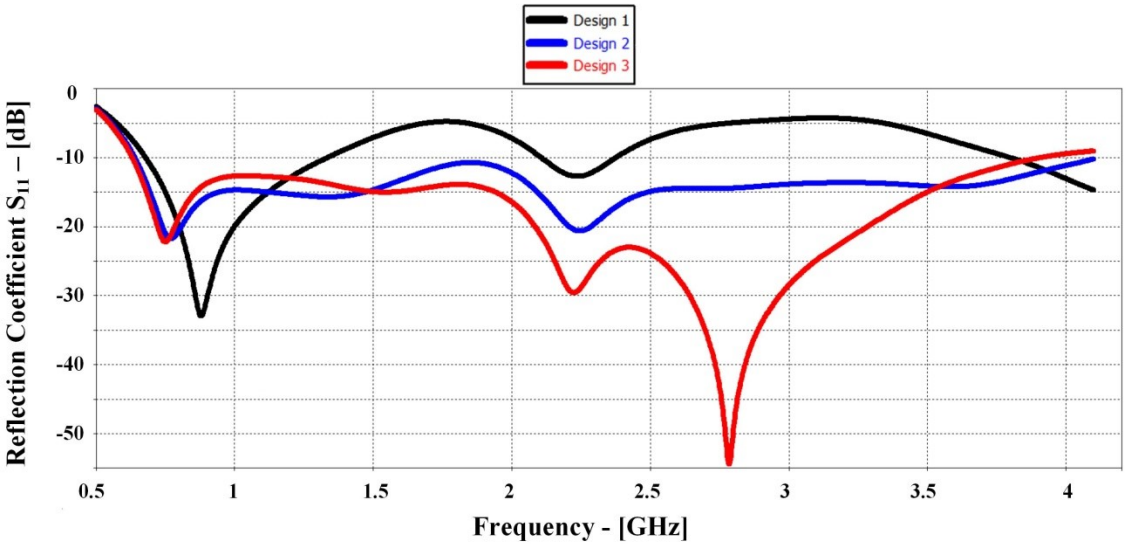

Figure 3-2 Return loss for three designs

Figure 3-2 illustrates the simulated return loss for the three designs. As can clearly be seen, the first design (black line) has one resonant frequency at 0.9 GHz corresponding to the total electric size of the dipole. It is basically a narrowband dipole antenna. The second design (blue line), with notches on the antenna patches, shows better impedance matching. The additional resonant frequency at 2.3 GHz makes the return loss greater. However, design 3 (red line) with its staircase shape has the best impedance bandwidth below -10 dB reference line among these three designs. Additional resonance is created at 2.8 GHz, due to an extra pair of notches.

3.2 Inductive and Capacitive Loading for Return Loss Improvement (LC-Loaded)

In recent years, there has been a growing demand for wireless sensors, local area networks (WLAN), mobile communication systems (GSM), Bluetooth, wireless (Wi-Fi), wireless local area networks (WLAN) and a wide variety of radar communication applications. In response to this demand, an antenna capable of covering different standard operating bandwidths to integrate all systems into one compact device while

maintaining its electromagnetic properties is very much desired. However, interference from one standard operating bandwidth to another one is a major issue preventing the realization of this goal. To address this issue, dual-band [33] and multiband antennas [34] with highly isolation between standard bandwidths have been introduced. Having a multiband antenna while maintaining compact size, low fabrication cost and the same performance as the original ultra-wideband antenna add even more challenges and complications for antenna designers. Capacitive and inductive loading technique is one suitable approach to achieving extra resonant frequencies and multiband antenna characteristics.

3.2.1 Capacitive and Inductive Loading Techniques

Depending on the antenna structure, different approaches have been introduced in the literature to load antennas. For instance, one of the most common techniques for planar monopole antennas is employing multiple strips to create several current paths on the strips. The current distribution on each strip corresponds to its own resonant frequency. Thus, by optimizing the size and location of the strips on the dielectric, desired resonant frequencies are obtained. The downsides of this technique are that it is difficult to adjust the operating frequency to the desired bandwidth, and it significantly increases the overall size of the antenna due to the large ground size [35].

One of the commonly used approaches in dual-band planar dipole antennas is to integrate two different dipole feeds through a single input terminal [36]. In another technique, to create an extra resonant frequency, a U slot is etched on the dipole's arms [37]. However, in these two approaches, the ratio of operating bands is greater than two [38]. In order to decrease this ratio, the geometric size of the U-shaped slots must be increased to adjust the resonant frequency of the slots. Hence, the slot will not fit in the dipole arms to achieve an appropriate ratio between working frequencies.

Another technique that has been recently developed is to simply load the antenna with resonant elements to create multiband planar antennas. One way is to use complementary split ring resonators (SRRs) on the antenna's arms. To implement SRRs on a planar

antenna structure, two or more concentric rings (which could be triangular, rectangular, circular, etc.) with different radiuses are etched on a substrate, as depicted in Figure 3-3 [39]. Short circuit connections are created between the slots to connect the center patch to the metallic sheet surrounding the whole ring structure. The current distribution then carries out high magnetic coupling across the slots created between the rings.

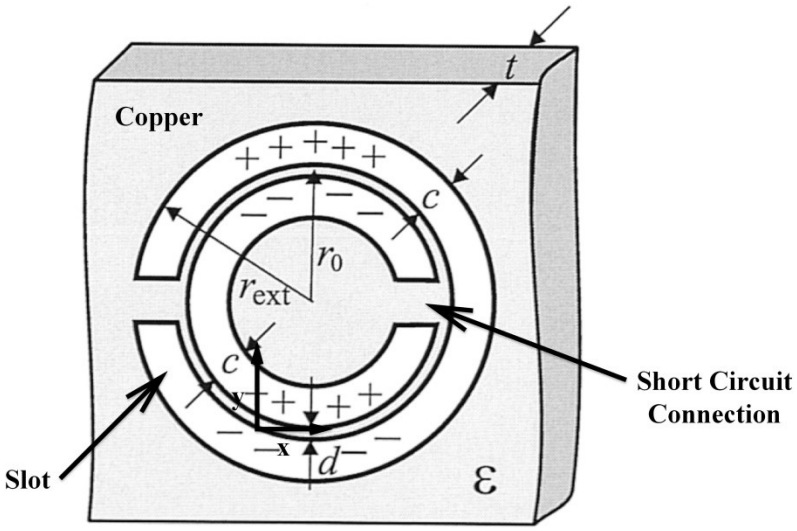

Figure 3-3 Edge coupled SRR one-cell unit [39]

The split rings generate negative permittivity and permeability and create strong distributed inductive and capacitive paths, which then create additional resonant frequency. Moreover, an SSR structure can be modeled as a parallel inductor and capacitor equivalent circuit. When SRR is exposed to an electromagnetic field perpendicular to the SRR structure orientation (e.g., an EM wave is along a z axis) with angular frequency of ω , an electromotive force is created around the structure, if the total size of the SSR is significantly smaller than the wavelength of the radiating frequency. The induced current across the slot edges develops a capacitance path and it is independent of the angular polar coordinate [39]. Hence, the currents that flow across both rings are identical. The entire SRR structure can be approximated as an LC in series, with a resonant frequency of ω_0 [40]:

$$\omega_0 = \sqrt{\frac{2}{\pi r_{avr} L_{total} C_{pul}}} \qquad \text{Equation 3-1}$$

where r_{avr} average radius of SRR, L_{total} is the total inductance of the rings, and C_{pul} is the capacitance per unit length. Figure 3-3 [39] shows an edge couple split ring structure.

3.3 Frequency Selective Surface (FSS) for Gain Enhancement

A typical frequency selective surface (FSS) is a two-dimensional planar structure with periodic metallic patches printed on the top of a dielectric substrate. FSS can be divided into two general categories of band pass filters and stop band filters, with each category branching out further to narrowband and wideband sub-category filters. The periodic metallic patches provide the filtering functions; their geometry sizes, shapes and distances between two adjacent periodic patches on a dielectric determine pass or rejection band characteristics as well as the desired operating frequency range. Brief literature reviews for pass band and stop band FSS are presented below.

3.3.1 Band-Pass and Band-Stop FSS

When a normal incident plane wave radiates to an FSS sheet, it creates a current flow on metallic patches, which are located on a dielectric medium (for the sake of theory discretion, a one-unit cell of an FSS sheet is explained). If the polarization of the electric field of the incident wave is perpendicular to the patch, a capacitive component will be constructed; when the electric field is parallel to the patch, an inductive component will be constructed [41]. Therefore, a one-unit cell of FSS which has both the parallel and perpendicular patches can be equivalent to an LC circuit in a series. The lumped inductance and capacitance values can be calculated from [42] and [43]. Therefore, the LC circuit creates a resonance frequency at f_0, which is calculated from Equation 3-2.

$$f_0 = \frac{1}{2\pi\sqrt{LC}} \qquad \text{Equation 3-2}$$

The examples below illustrate bandpass and bandstop filtering FSS.

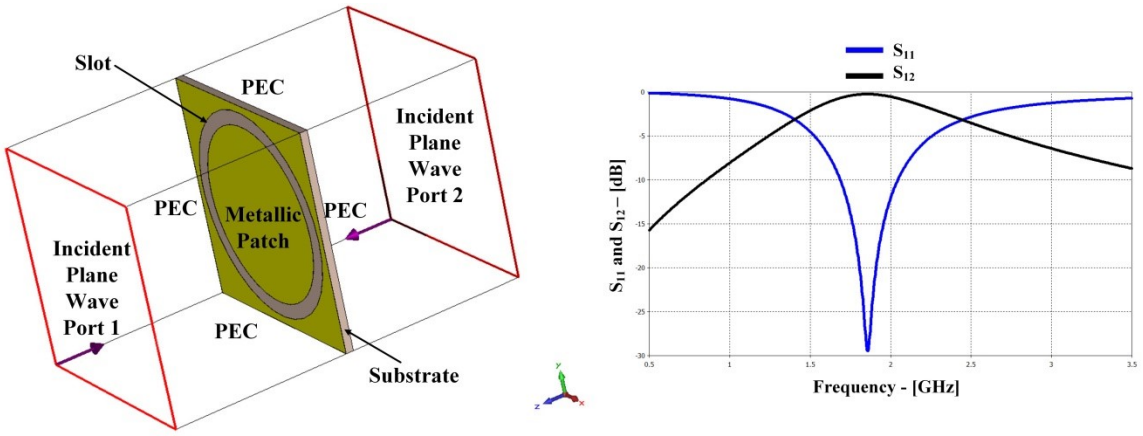

Figure 3-4 A unit cell band-pass filter (left) and S_{11} and S_{12} *of the unit cell (right)*

Figure 3-4 shows a unit cell of a band-pass filter made of a circular slot ring. The conductive patch is copper with an electrical conductivity of 5.8×10^{7} S/m on an FR4 substrate with 1.6 mm thickness and dielectric permittivity of 4.3. The substrate is 45 mm by 45 mm and the inner radius of the slot ring is 18 mm with a slot width of 3 mm. The unit cell is located between port one and two. The ports are radiating normal incident waves and strike the metallic patch perpendicularly. The simulated transmission coefficient and reflection coefficient of the unit cell are shown in Figure 3-5. It can clearly be seen that this FSS works as a band pass filter with a frequency range from 1.7 to 2 GHz.

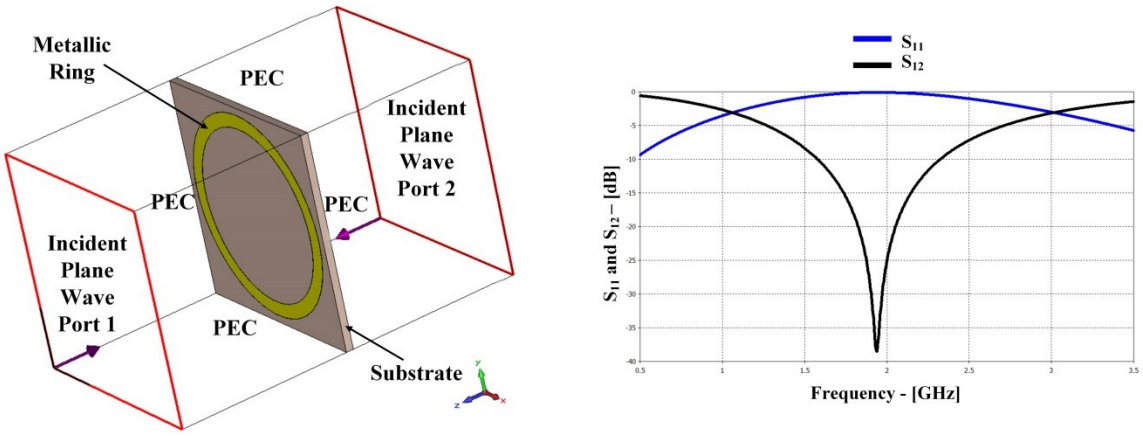

Figure 3-5 One-unit cell stop-pass filter (left) and S_{11} and S_{12} *of the unit cell (right)*

Figure 3-5 demonstrates a band-stop filter exposed to the perpendicular incident wave radiation. This unit cell has the same specifications and geometry size as the previous filter; but because it has a metallic ring instead of a slot ring, it works as a stop band filter, as shown in Figure 3-5. From the plot in Figure 3-5, the rejection band of the stop band filter is from 1.6 GHz to 2.3 GHz.

The band-stop filtering FSS is selected to be used in this thesis as a reflector for the proposed antenna for gain enhancement. Therefore, the next section explains operation principles of the FSS as a reflector.

3.3.2 Principles of FSS as a reflector

Typically, periodic structures in frequency selective surface (FSS) designs have narrowband characteristics. In order to extend the operating bandwidth of FSS structures to cover the desired UWB bandwidth, a second layer of frequency selective surface is designed to stack with the first layer. The design, geometry size and electromagnetic properties of layer one, layer two and stacked layers are described in section 4.3.

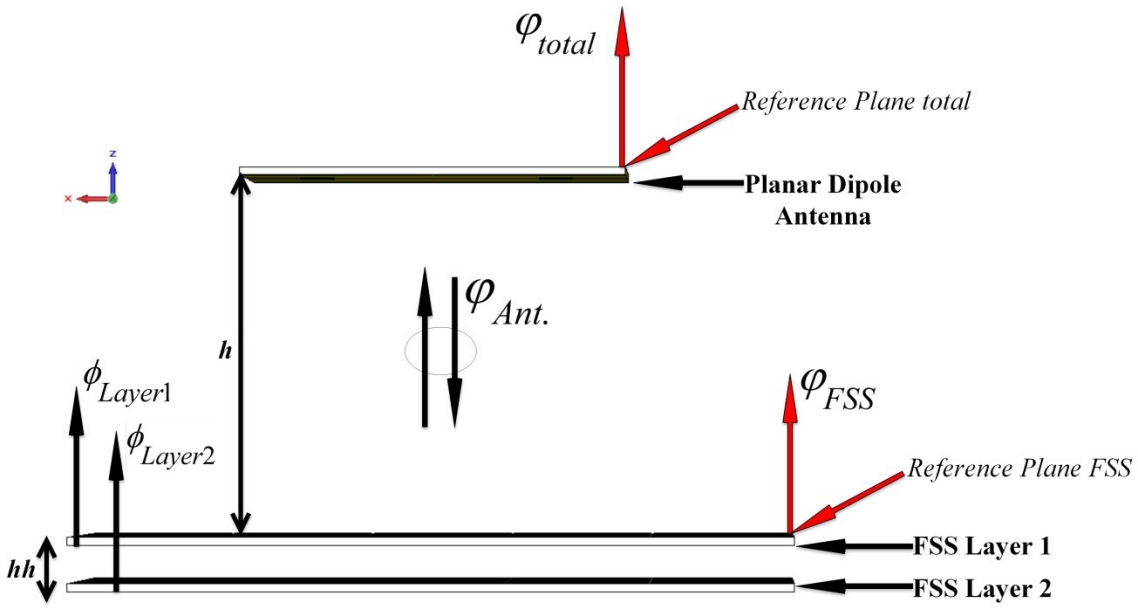

Figure 3-6 Double-layer FSS for gain enhancement

In principle, FSS reflects electromagnetic waves in a different manner than a simple copper sheet where reflects back the entire frequency range. In order to understand FSS behavior, a double-layer FSS is placed in front of a planar dipole antenna as shown in Figure 3-6. Layer-1 with a reflection phase of φ_{Layer1} is placed with a distance of h from the antenna. Layer-2 with a reflection phase of φ_{Layer2} is placed with a distance of hh behind the first layer. ϕ_{FSS} at the reference plane on the top of layer-1 can be found as

$$\phi_{FSS} = f\left(\phi_{Layer1}, \phi_{Layer2}\right) \qquad \text{Equation 3-3}$$

With the presence of FSS, the antenna back radiation is reflected backward towards the antenna by double-layer FSS and will add to the front radiated waves of the antenna. If they are in phase, both waves will combine constructively and the gain of the antenna will increase; otherwise they will subtract from each other, reduce the gain and then become bandstop. The combined phase can be written as:

$$\phi_{total} = \phi_{FSS} + \phi_{Ant.} \qquad \text{Equation 3-4}$$

$$\phi_{Ant.} = 2 \times \frac{2\pi f}{c} \times h \qquad \text{Equation 3-5}$$

where ϕ_{Ant} is the round-trip free-space propagation phase delay between the antenna and the *reference plane FSS* [57] which is controlled by the spacing h between the antenna and the double-layer FSS. In order to have in-phase reflection in front of the antenna and also phase coherence for all frequencies, the total reflection phase φ_{total} at the *reference plane total* should be zero or integral multiple of 2π for the all operating frequency bandwidth. As can be seen in Equation 3-5, the phase delay $\varphi_{Ant.}$ has a direct relation to the frequency and increases with f; hence the optimum reflection phase from both FSS layers will be obtained when φ_{FSS} decreases with the same ratio as the frequency. Section 4.3 will show the simulated reflection phase and measured transmission coefficient of the proposed double layer FSS.

3.4 Microstrip to Parallel Strip Transformer for Broadband Impedance Matching

An effective antenna feeding strategy is a crucial factor in antenna efficiency, radiation pattern, and operating bandwidth. There should be good impedance matching between the input impedance of the antenna and the feeding cable (for instance a coax cable with a SMA connector), as this prevents unwanted current reflection in the feeding port and transforms an unbalanced current into a balanced one at the antenna feeding line. A common approach to satisfying these points is using a transformer (balun) to match the antenna input impedance to cable impedance. Another approach is to convert an unbalanced current to balanced current distribution. The result is having a matched

transmission line that could lead to an antenna with an ultra-wideband operating bandwidth.

For radar applications, a variety of wideband balun structures are introduced in the literature, such as a wideband planar log-periodic balun [44], a wideband planar March balun [45], a wideband coplanar wave guide [46], a wideband microstrip to coplanar stripling [47], and a wideband microstrip to parallel strip balun [48].

The bandwidth of a log-periodic balun is related to the number of resonator sections. Thus, in order to design this type of balun to cover a wide operating band, a large structure is needed, which is not suitable for most radar applications. The March balun covers a wide frequency range but suffers from a high loss. The wideband microstrip to coplanar wave guide is a potential candidate, as it includes most of the desired properties for our application. However, this it is not suitable for our design due to the balun's structure. Likewise, although the microstrip to coplanar strip line shows very good matching with the input terminals of the antenna and behaves as a wideband transformer, it is also unsuitable for our purposes because it experiences high transition loss.

A wideband microstrip lines to parallel strip lines balun is employed in our design due to its wide frequency band and negligible loss, structure simplicity, low fabrication cost, small size, and low profile compared with other balun designs. Typically, a microstrip to parallel strip balun is employed to feed balanced antennas such as planar dipole antennas.

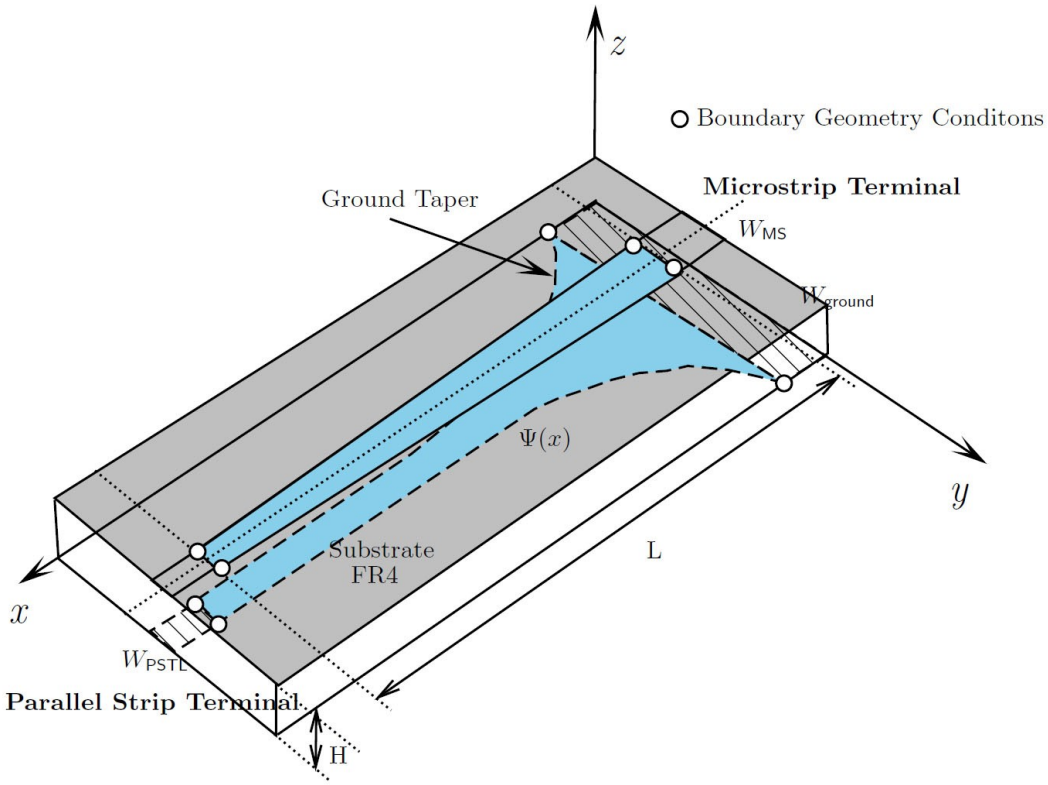

Figure 3-7 Microstrip to parallel strip tapered balun [49]

Figure 3-7 shows a microstrip to parallel strip tapered balun. As can be seen, the top transition line has a linear taper shape from the microstrip terminal to the parallel strip terminal. On the other side of the substrate (in this example, FR4), the ground transition line is tapered gradually from a finite ground plane at the microstrip terminal to the parallel strip terminal, with the same width as the top layer at this terminal. The electromagnetic properties of the transition between the two terminals are characterized by a taper technique conversion applied on the bottom layer introduced in [49]. Therefore, the reflected power through the balun depends on the impedance at any physical point along the balun structure.

Chapter 4 THE PROPOSED ANTENNA AND DESIGN

In this work, open complementary double-concentric split-hexagonal-ring resonators and chip resistors are integrated into a compact planar dipole antenna and form the proposed antenna for ground penetrating radar applications. It has broadband characteristics of classical dipole antennas, such as symmetric radiation patterns and consistent radiation efficient. It is fed with a broadband microstrip to parallel strip lines transformer (Balun) to achieve ultra-wideband impedance matching and balanced surface current distribution. Furthermore, a double-layer frequency selective surface (FSS) reflector is added for gain improvement and in-phase reflection, achieving a gain comparable to that of horn antennas.

4.1 The Proposed Antenna

The geometric design of the proposed antenna is shown in Figure 4-1, where Figure 4-1(a) shows the fabricated three-dimensional view of the overall design and Figure 4-1(b) illustrates one arm of the planar dipole with the staircase technique, respectively. The detailed dimensions of the proposed antenna are tabulated in Table I.

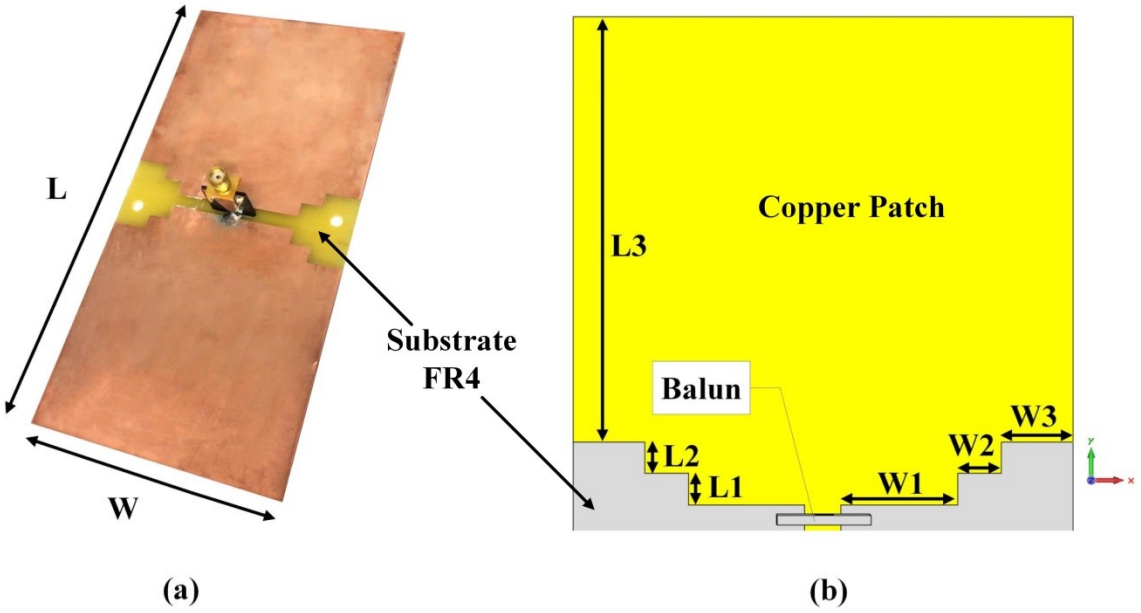

Figure 4-1 Fabricated proposed planar dipole antenna (a) and isometric view of the simulated antenna structure (b)

Table I Antenna dimensions

L	160 mm	**W**	80 mm
L1	5 mm	**W1**	18.6 mm
L2	5 mm	**W2**	7 mm
L3	68 mm	**W3**	11.5 mm

As shown in Figure 4-1(b), the lower portion of each arm of the proposed planar dipole is shaped in a staircase manner, with step increments chosen to be quarter wavelengths of different frequencies for bandwidth enhancement and size reduction. The simulated and measured reflection coefficient, gain, directivity, radiation pattern and half-power bandwidth of the planar dipole are presented and studied in the next chapter.

4.2 The Double Hexagonal Ring

In order to enhance bandwidth and obtain a greater return loss for the proposed antenna (especially at a low frequency end of the operating bandwidth between 1 to 2 GHz), open complementary double-concentric split-hexagonal-ring resonators (LC-Tank) are employed on each arm of the antenna. The geometric layout of the split-hexagonal-ring resonators is depicted in Figure 4-2.

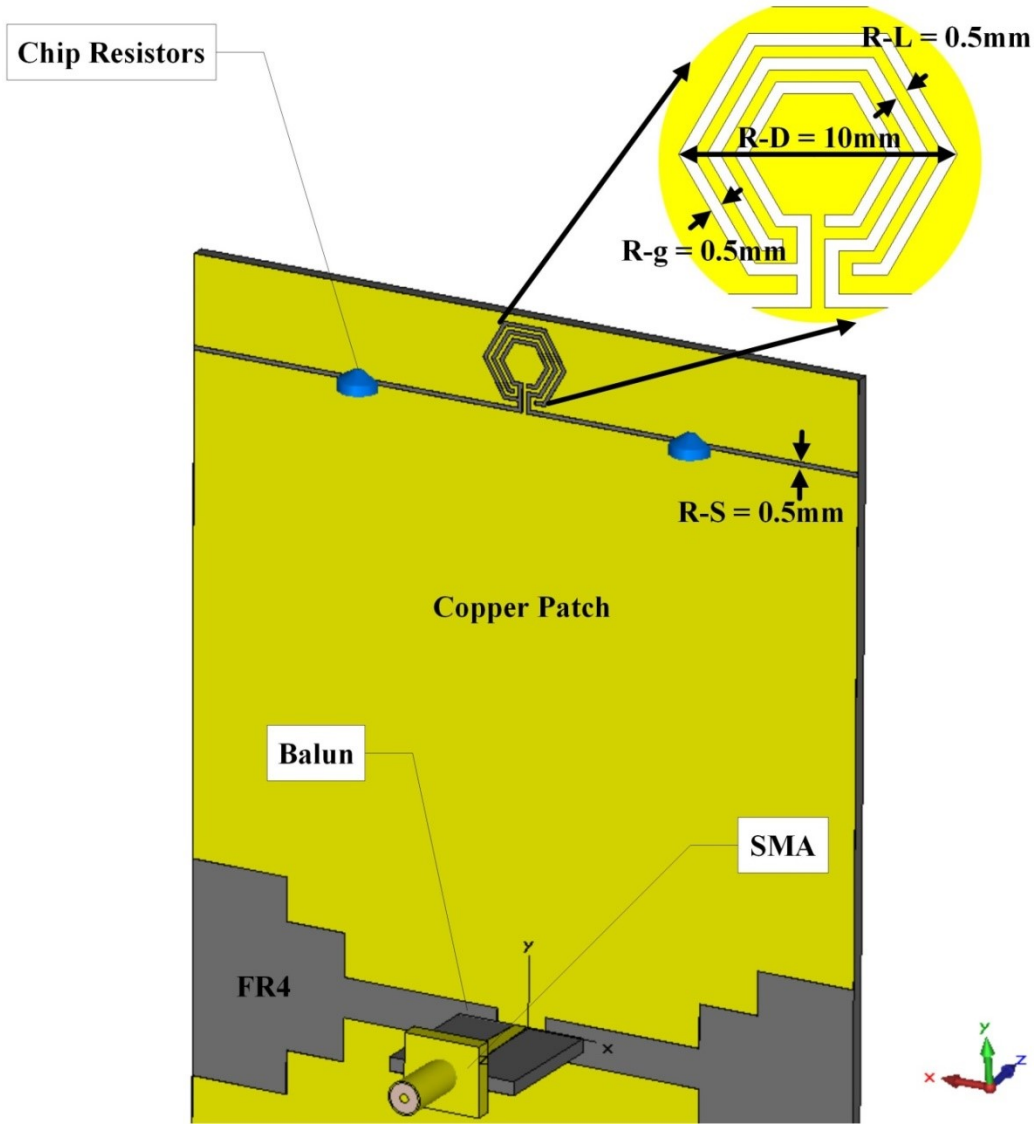

Figure 4-2 Zoom view of the double hexagonal ring layout

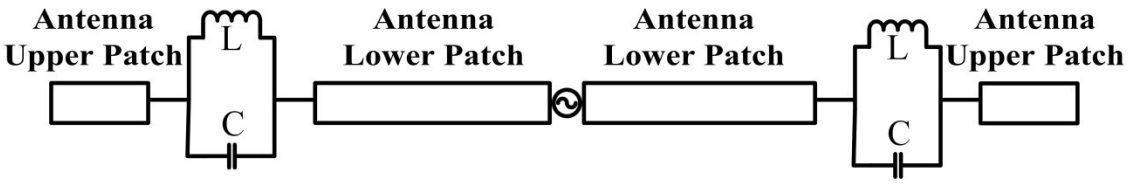

Figure 4-3 Equivalent circuit model of the proposed antenna loaded with LC-Tank

As illustrated by Figure 4-2, when the split-hexagonal ring is inserted into each arm of the printed dipole, it divides the antenna arm into two separate regions, leading to two current paths: an inductive path, where surface current flows along the thin strips of the hexagonal ring (R-S), and a capacitive path, where displacement current flows across the slots of the ring (R-G). Thus, the equivalent circuit of the split-hexagonal ring can be modeled as a series-connected parallel LC resonator (Figure 4-3) [50]. The resonance frequency of the ring resonator is determined in Equation 4-1 as,

$$f_r = \frac{1}{2\pi\sqrt{LC}} \qquad \text{Equation 4-1}$$

As the impedance of the ring resonator at its resonance frequency is very high, the current flows from the feeding point will see an open circuit at the ring resonator. However, if the ring resonator is located at approximately λ/4 from the feeding point at its resonance frequency f_r, an additional resonance can be realized.

The above design principle is adopted to create an additional resonance close to the first resonance of the planar dipole, and in turn provide a greater return loss at the low frequency end of the operational band. The ring resonators are designed to resonate at 770 MHz (20 MHz above the first resonance of the antenna) and are placed at appropriate locations near the end of the dipole arms ($\lambda/4$ from the feeding point at 770 MHz). The measured and simulated return loss of the antenna with and without rings are presented in the next chapter. The approach [51] that relates the geometric dimensions of the split-hexagonal ring to its equivalent LC values is adopted in this work to design the ring resonators.

To further improve the impedance matching at low frequencies of the printed dipole and also prevent unwanted reflection from the open end of the antenna (which causes a late time ringing effect), a pair of chip resistors (100 Ω each) are applied to each arm of the antenna and are placed in parallel with the split-hexagonal ring resonator (see Figure 4-2). The overall electrical size of the proposed planar dipole is only 0.33 $\lambda \times 0.16\ \lambda$ (80 $\times$ 160 mm^2), where λ is the wavelength corresponding to the lower limit of the operation band.

4.3 The Double-Layer FSS

To enhance the gain and radiation directivity of the proposed planar dipole antenna, a double-layer Frequency Selective Surface (FSS) is added as a reflector for the antenna. A unit cell of the FSS layer-1 is illustrated in Figure 4-4 (left), which has a resonant frequency of 1.75 GHz as shown in Figure 4-6. One unit cell of FSS layer-2 is illustrated in Figure 4-4 (right) and exhibits a considerably lower resonant frequency at 0.75 GHz as shown in Figure 4-6; it has the same overall size of the unit cell of the first FSS layer. This, in turn, alleviates the need for a larger FSS panel for the low-end frequency of the antenna.

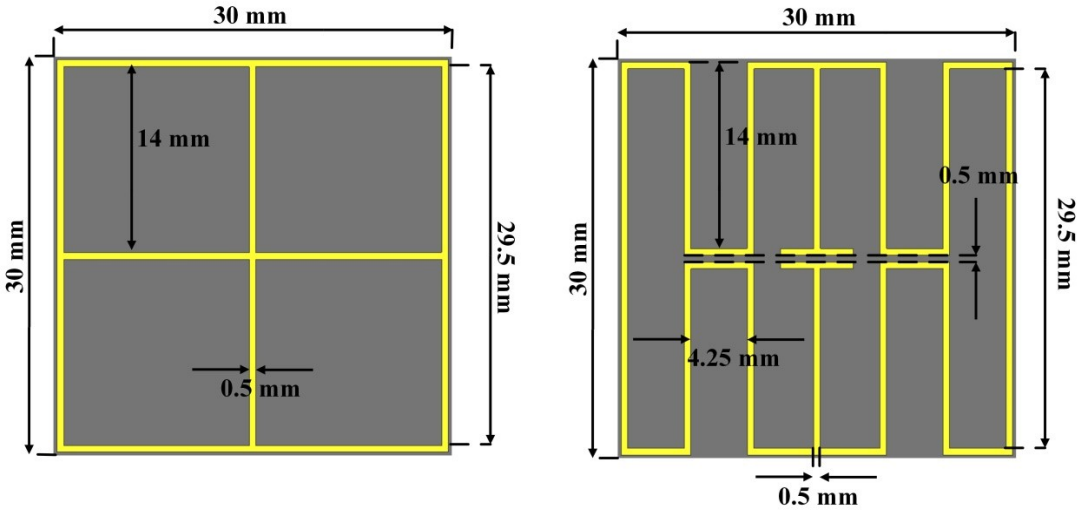

Figure 4-4 FSS layer-1dimensions (left) and FSS layer-2 dimensions (right)

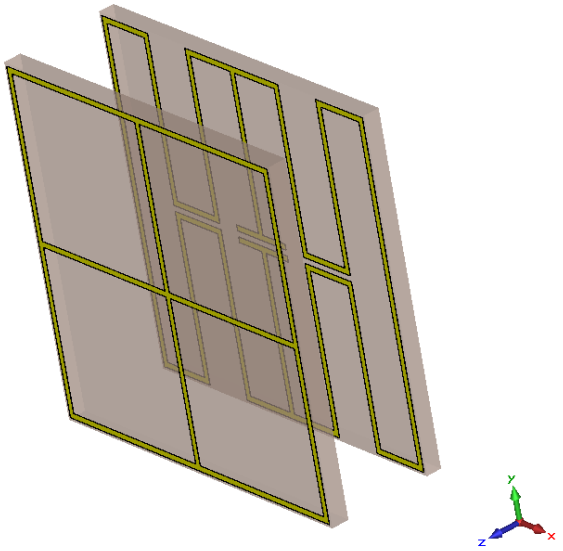

Figure 4-5 Double-layer FSS

The two layer FSSs are placed 8 mm apart and form the double-layer FSS which is illustrated Figure 4-5.

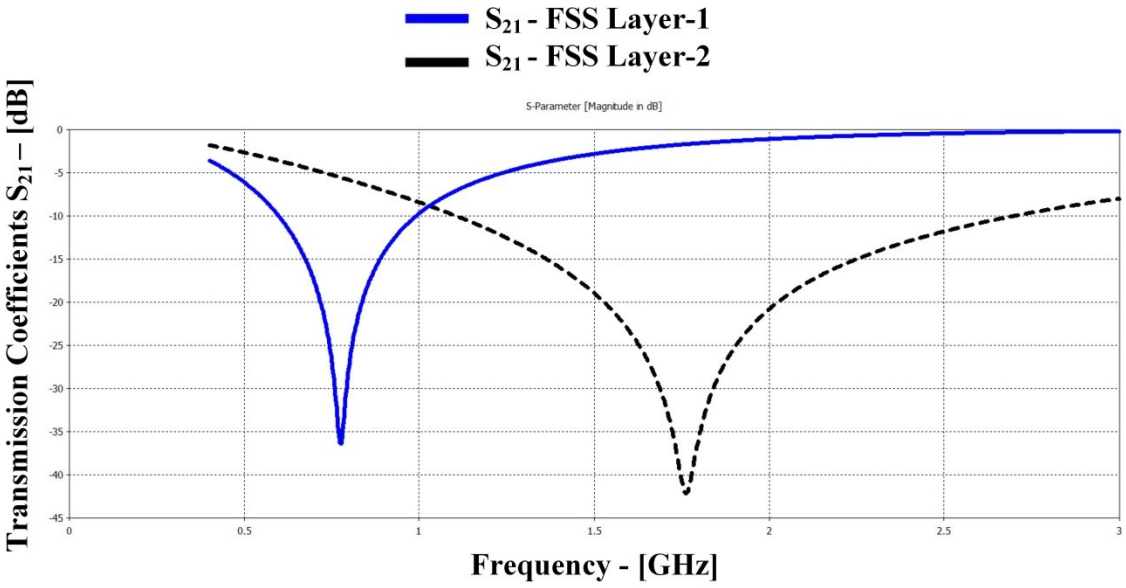

Figure 4-6 Transmission coefficients of FSS layer-1 (black) and FSS layer-2 (blue)

Figure 4-6 shows the transmission coefficients of the two FSS layers, respectively. Figure 4-7 shows the simulated reflection phase and transmission coefficient (S21) of the proposed double-layer FSS. As shown, the dual-layer FSS operates over a bandwidth of 132% from 0.64 GHz to 3.1 GHz, with a S21 of less than -10 dB; it provides effective in-phase reflection of the electromagnetic radiation from the planar dipole and thus coherent reflected waves at the front plane of the antenna [52]. In most designs reported so far, a minimum spacing of 1/4 wavelength is recommended between the antenna and its reflector sheet for good radiation directivity, gain, and interference isolation [53]. However, with the proposed double-layer FSS, the FSS reflector is located only 1/8 of the wavelength (60 mm) from the dipole antenna, resulting in a substantial height reduction of the design.

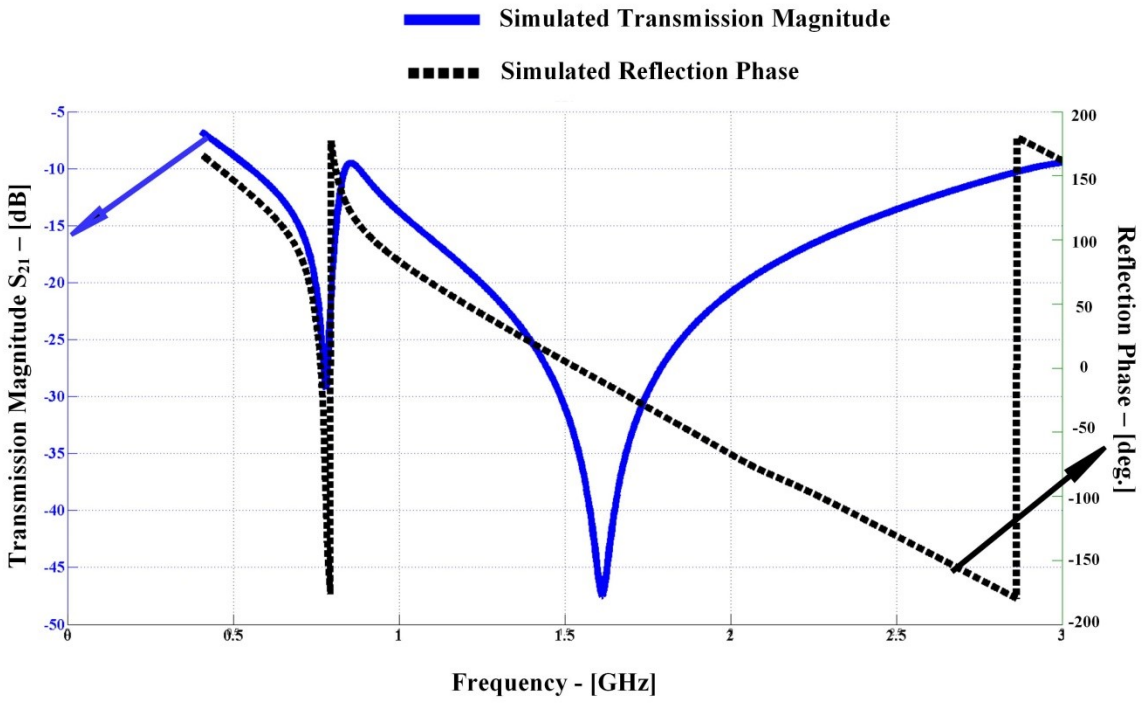

Figure 4-7 Simulated reflection phase (black) and simulated transmission coefficient of the double-layer FSS (blue)

To validate the simulation results, the proposed double-layer FSS was placed between a transmitter antenna and a receiver antenna in the anechoic chamber and then measured. On the transmitter side, a log-periodic antenna was employed, while on the receiver side,

a double ridge horn antenna was used. The transmitter and receiver antennas were placed face-to-face, with one meter separation between the two antennas. The size of the fabricated double-layer FSS is 270 mm by 210 mm Due to limited size of the FSS sheet, electromagnetic waves can propagate around the FSS reflector. Absorber walls were then added which extended from four sides of the double-layer FSS to eliminate the problem. Figure 4-8 shows the transmitter antenna pointed at the proposed double-layer FSS, with the absorber walls around it.

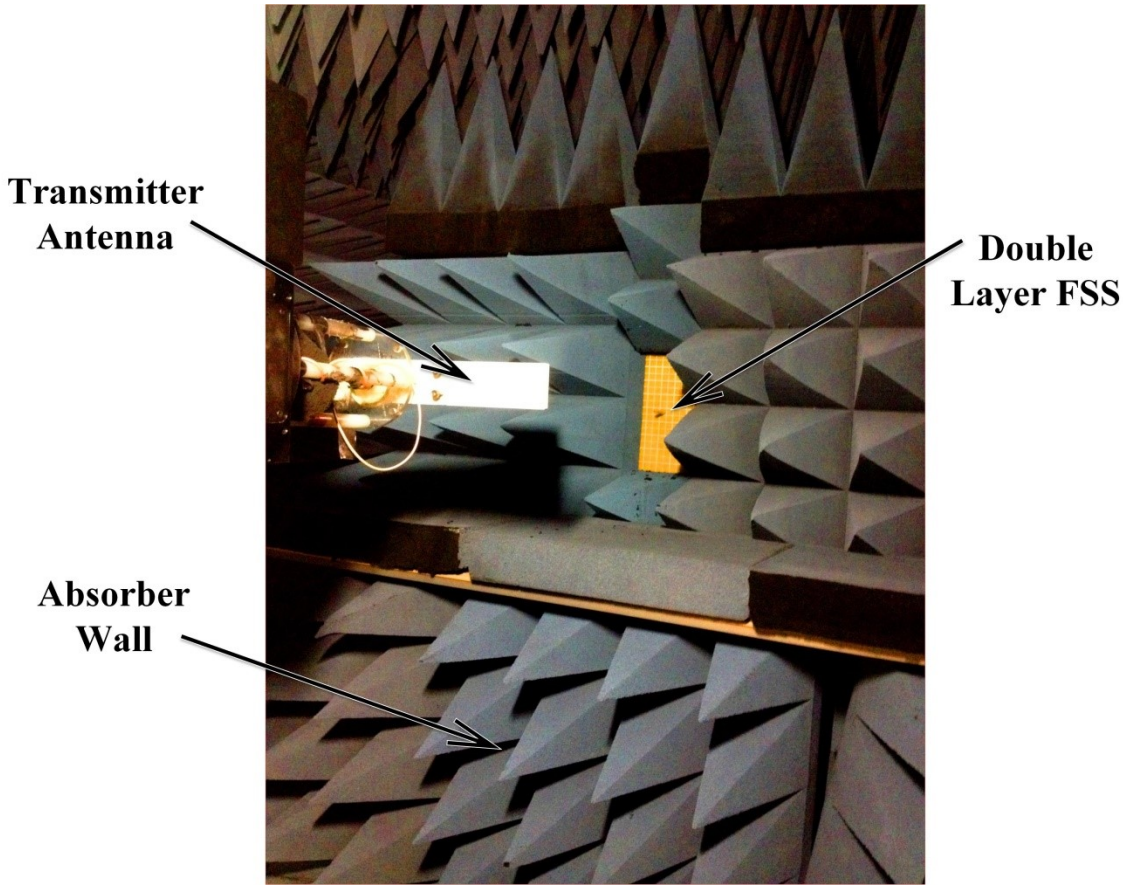

Figure 4-8 Double-layer FSS in anechoic chamber surrounded by absorber walls

The transmitter is connected to a vector signal generator (Agilent E4438C) and the receiver antenna is connected to a spectrum analyzer (Agilent E4440A). Both pieces of the equipment are capable of covering the desired bandwidth for this experiment (from 500 MHz to 3 GHz).

In order to measure the transmission magnitude (S21) of the proposed double-layer FSS, first, the received power at the receiver antenna without the double-layer FSS was measured at a desired frequency. Then, the received power at the receiver antenna with the double-layer FSS was measured at the same frequency point. The ratio of the two measured results is the transmission magnitude at one frequency. This process is then swept for the entire desired frequency range.

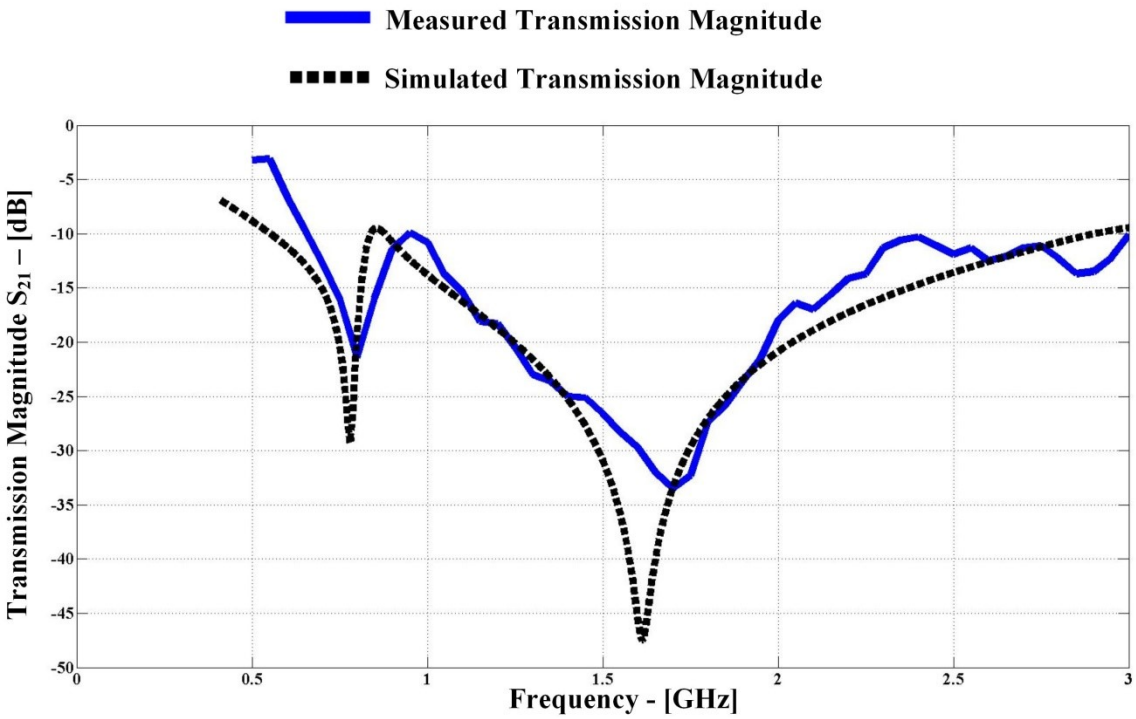

Figure 4-9 Simulation and measurement transmission magnitude (S21) results

Figure 4-9 shows both the measured and simulated transmission coefficient (S21) of the proposed double-layer FSS. The first resonance corresponds to that of layer-2 and the second to that of layer-1, and together they cover the entire desired bandwidth. There is an acceptable disagreement between the simulated and measured results, which are due to fabrication error, measurement errors and ideal setting of the simulations.

4.4 The Balun

To obtain a wideband impedance matching between a 50 Ω coax cable and input terminal of the planar dipole antenna, and also to yield a balanced current distribution on the surface of the antenna, a tapered shape balun [54] was adopted as shown in Figure 4-10 The tapered patches on the balun have a linear transition from the microstrip line to the parallel-plate line to reduce possible reflections.

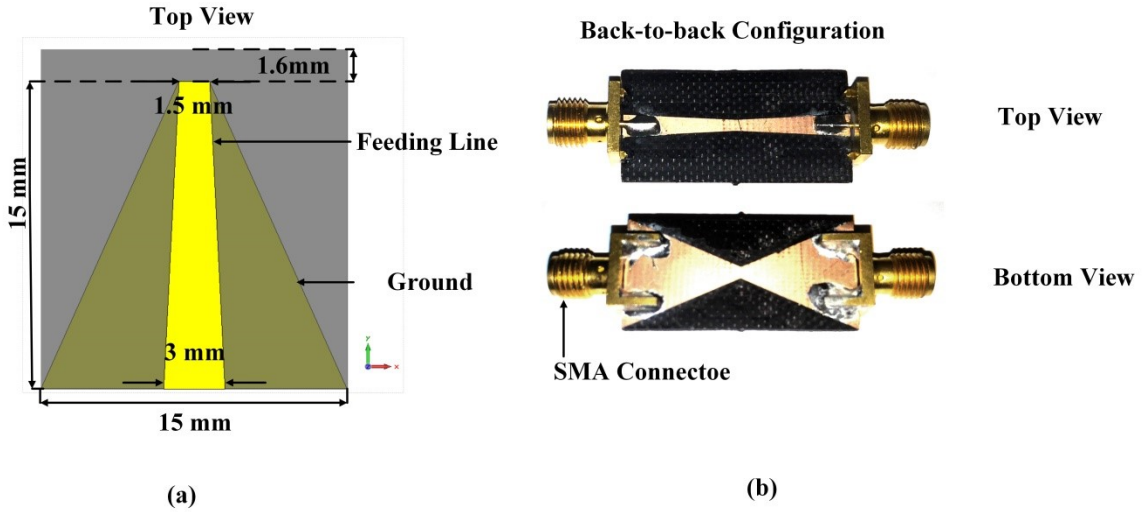

Figure 4-10 Geometric view of the presented balun (a) and back-to-back configuration of the fabricated balun (b)

The balun is fabricated on a 15 mm by 16.6 mm double-sided FR-4 substrate with a thickness of 1.6 mm. A rectangular opening of 15 mm by 1.6 mm was cut off in the center of the antenna's substrate for the balun to be inserted from the front side.

The proposed UWB antenna operates in a frequency range of 0.63GHz to 3.9 GHz. The balun should cover at least the same range of frequency. The return and insertion losses of the proposed balun design with a back-to-back configuration (see Figure 4-10(b)) were investigated. Figure 4-11 shows the measured S11 and S21 of the balun in a frequency range of 0 to 8 GHz. The measurement results indicate that the proposed balun exhibits a

greater than 14 dB return loss for the entire operational bandwidth of the dipole antenna, with an insertion loss of less than 2dB.

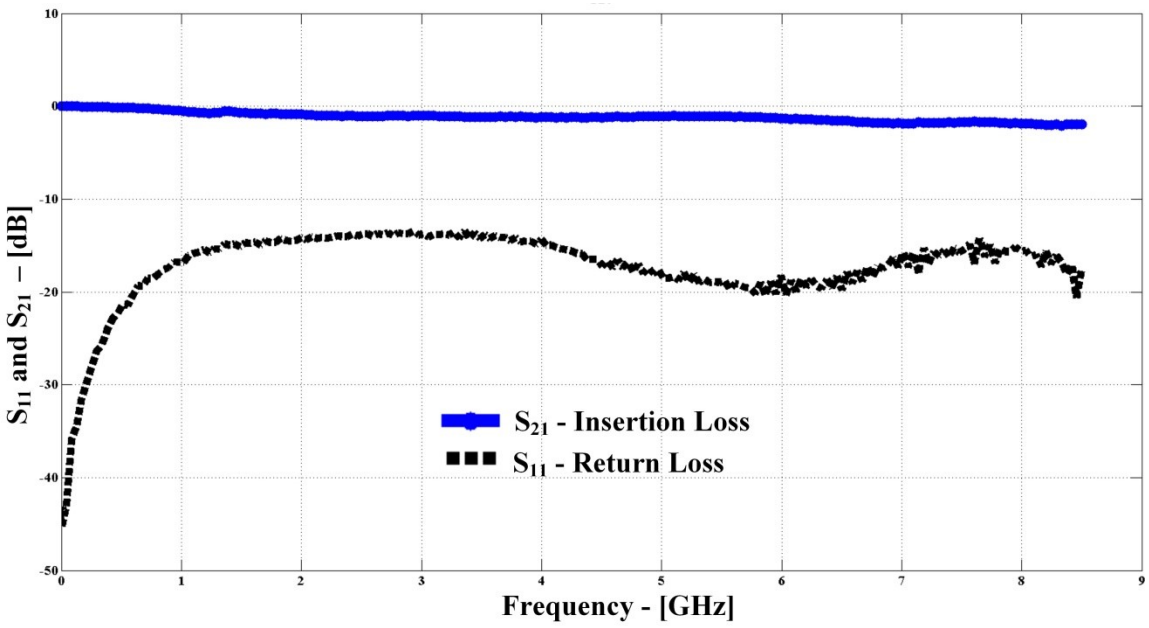

Figure 4-11 Measured return loss (S11- blue) and insertion loss (S21- black) of the proposed balun

Chapter 5 SIMULATIONS AND MEASUREMENTS

5.1 Simulation Tools

In this thesis, Computer Simulation Technology (CST) Microwave Studio (MWS) 2013 with educational license was employed to obtain all simulations the proposed antenna, the balun, and the FSS layers [55]. CST MWS is mature commercial electromagnetic CAD software and is especially suitable for large electromagnetic structures. The transient solver provides fast and accurate results of S-parameters, gain, directivity, efficiency, input impedance, etc.

5.2 Fabricating and Measuring Equipment

5.2.1 Milling Machine for Fabrication

All components of the proposed compact and high-gain UWB antenna presented in this thesis, including dipole antenna, FSS layer-1, FSS layer-2 and balun, are planar structures. They are all fabricated on single-layer FR4 substrates except for the balun, which needs to be fabricated on a double-layer FR4. After being finalized, from the simulations, the design layouts of the structures were drawn in AutoCAD and then converted to Gerber files to be readable for milling machines. The milling machine of MITS Electronics FP-21T in the Electrical and Computer Engineering Department at Dalhousie University is capable of fabricating Printed Circuit Boards (PCB) of the antennas. The maximum working area of the milling machine is 350 mm by 250 mm, which is suitable for building larger designs such as the proposed FSS layers one and two. Figure 5-1 shows the milling machine, MITS Electronics FP-21T. It is able to cut and drill copper off a substrate with a minimum pattern width of 0.1 mm and a resolution 4 micro millimeters.

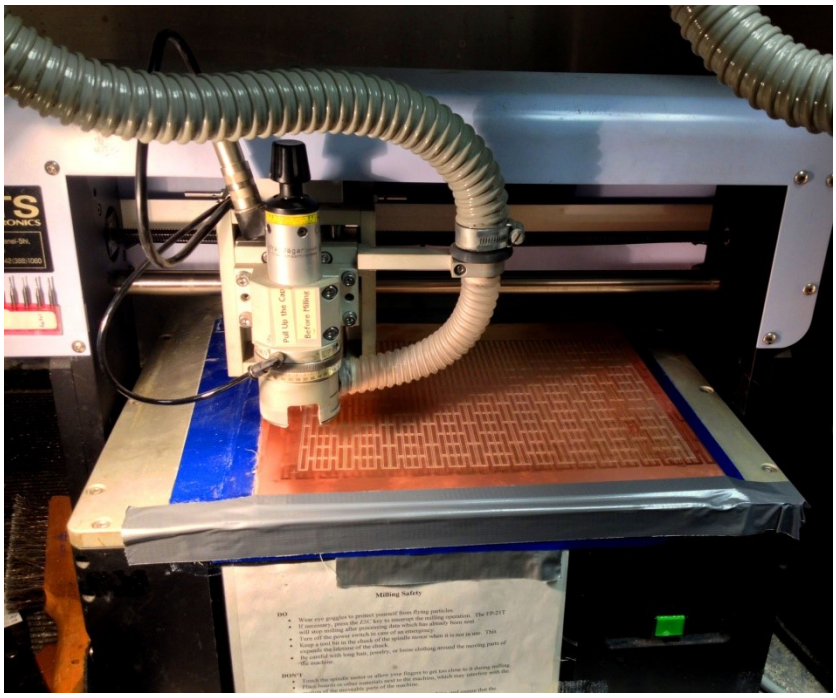

Figure 5-1 MITS Electronics FP-21T milling machine

5.2.2 Anechoic Chamber

Antenna measurements are performed in an anechoic chamber system using a NSI 700s 30 Near-Field scanner. The scanner is a spherical scanner, meaning a probe takes measurements all around the test antenna at an almost constant distance. This scanning process is ideal for antennas that are small, lightweight, and have an omnidirectional radiation pattern. The complete system is composed of an anechoic chamber, mechanical antenna/probe mounts, relevant controller units, a frequency analyzer/generator, and a computer installed with the control software.

Scanning takes place within the anechoic chamber. The chamber provides an ideal environment for antenna measurement by minimizing radiation interference. The metal exterior of the chamber acts as a faraday cage, preventing outside radiation sources from electromagnetically illuminating the chamber and interfering with measurements. Pyramid-shaped foam, known as absorbers, is installed on all the inside walls of the anechoic chamber to absorb electromagnetic waves impinging on them and to emulate

open space. Figure 5-2 shows an inside view of the anechoic chamber situated at the Microwave and Wireless Research Lab at Dalhousie University.

Figure 5-2 Anechoic chamber

Inside the anechoic chambers are also mechanical stands that hold and move the antenna and probe used for testing. The phi and theta motors rotate the antenna so that the probe can face the antenna at any unit angle around it. This allows the probe to collect data all around the antenna without having to actually move around the antenna. By rotating the antenna in one place using the two motors, the relative equivalent of having the probe move all around the antenna can be achieved.

5.2.3 Vector Network Analyzer

The electromagnetic waves are transmitted and received through the antenna and probe by the vector network analyzer (Agilent 8722ES), which covers the 50 MHz to 40 GHz

frequency range, as shown in Figure 5-3. The scanner rotators are controlled by the range controller box (second box from the bottom).

Figure 5-3 Vector network analyzer Agilent 8722ES

The bottom box is the data acquisition box. The whole system is hooked up to a PC that contains the necessary software (NSI 2000) to operate the system inside the anechoic chamber.

5.3 Results

In this section, all of the simulation and measurement results of the proposed planar dipole antenna with/without double hexagonal rings and chip resistors and double-layer

FSS are presented. The electromagnetic properties of the proposed design are discussed in terms of return loss, radiation pattern (electric and magnetic field), half-power beamwidth, and gain.

5.3.1 Antenna

The proposed planar dipole antenna without LC-tank (hexagonal rings) and chip resistors is shown in Figure 5-4. The antenna is fed from the front with the proposed wideband balun via an SMA connector.

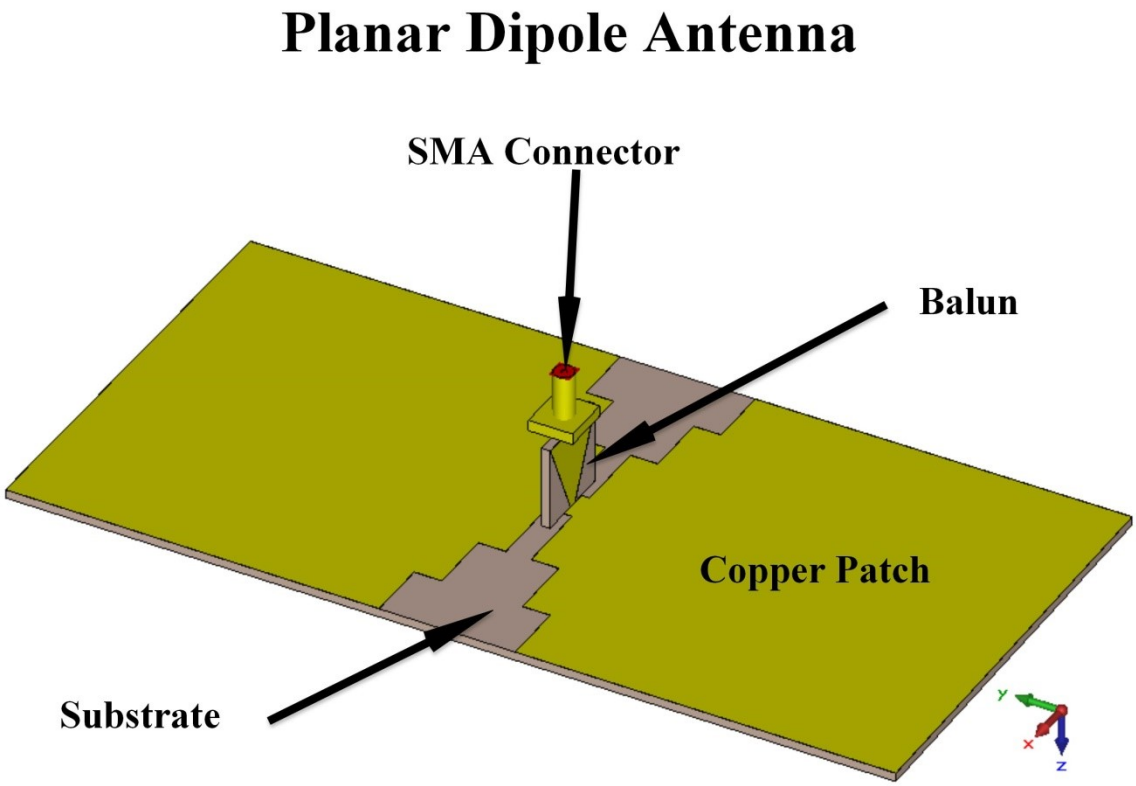

Figure 5-4 Proposed planar dipole antenna

To investigate the advantages of implementing the staircase technique for the proposed planar dipole antenna, a parametric study for the parameter W2 (see Figure 4-1) is shown in Figure 5-5. As can be seen, by changing the value of W2, the reflection coefficient of

the antenna will change, especially for higher frequency ranges. W2 changes the input matching of the antenna and thus the bandwidth enhancement for the presented antenna.

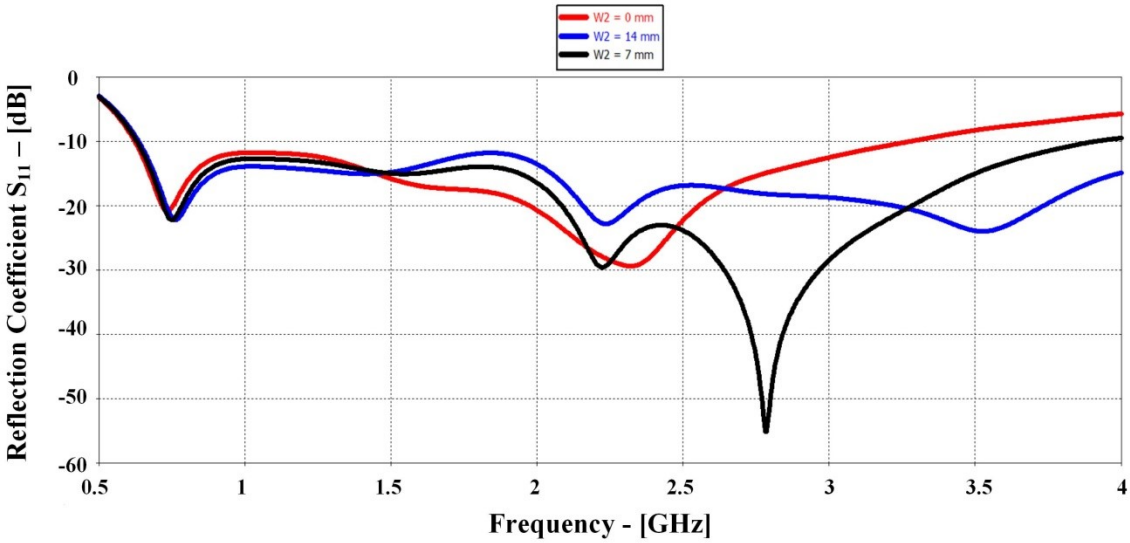

Figure 5-5 Reflection coefficient of the proposed antenna for different W2

5.3.2 Antenna with the copper sheet

Typically, in radar applications, the transmitter and receiver antennas face the ground. Thus, to isolate the antenna, prevent electromagnetic interference and increase the gain of the antenna, a reflector sheet is placed in front of the antenna, parallel to the ground. This will focus more radiation to the back, where the object is located. The proposed planar dipole antenna with a rectangular copper reflector is depicted in Figure 5-6.

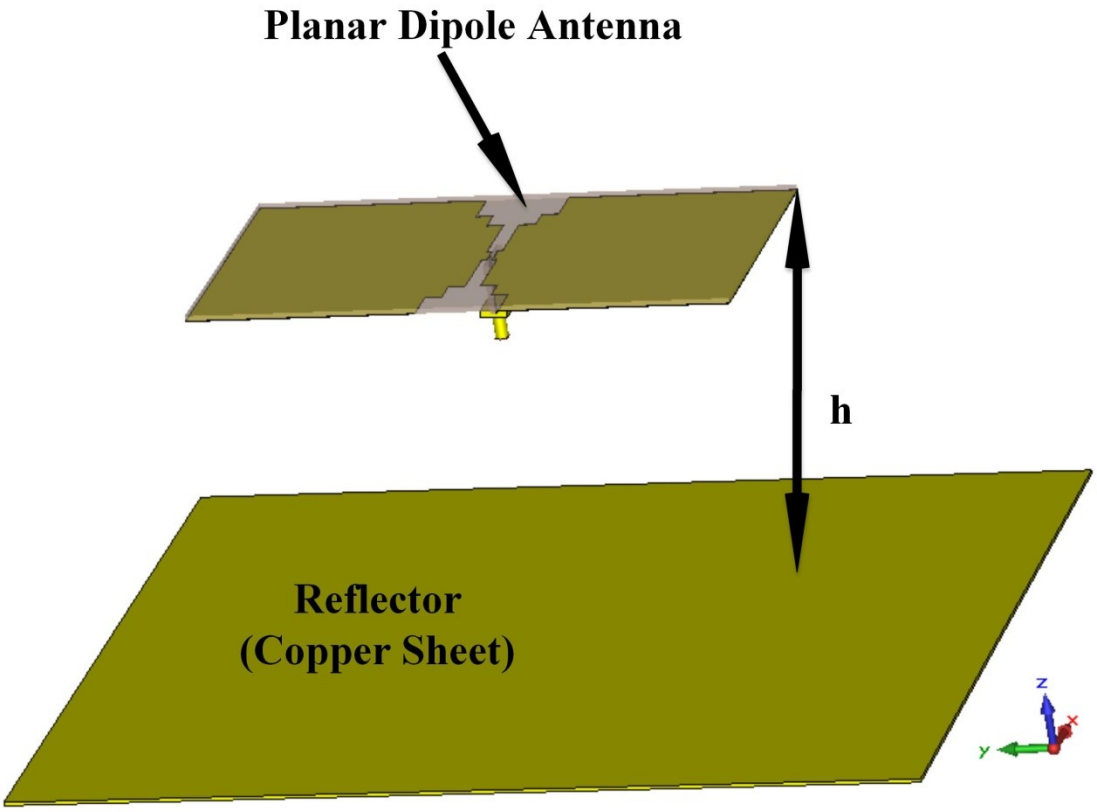

Figure 5-6 Proposed planar dipole antenna backed with a copper sheet

The rectangular reflector sheet, with an overall size of 210 mm by 270 mm, is placed at a distance of h from the antenna. Copper sheets are usually set at a distance near to a quarter of the wavelength ($\lambda/4$) of the antenna's lowest operation frequency. The value of h is swept from $\lambda/8$ to $\lambda/4$ in order to obtain the optimum lowest value for h. The simulation results of the reflection coefficient for parameter h are shown in Figure 5-7.

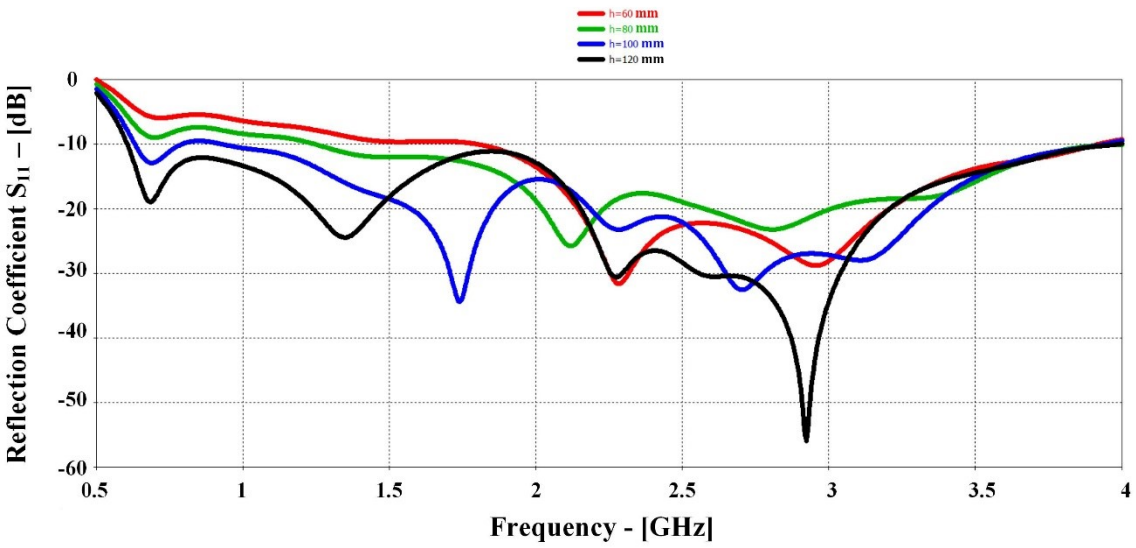

Figure 5-7 Reflection coefficient of the proposed antenna with copper sheet for parameter h

As shown, a return loss of higher than 10 dB is obtained for the entire desirable operational bandwidth of the antenna with $h = 120\ mm$, which corresponds to $\lambda/4$ at the lowest operating frequency ($630\ MHz$) of the antenna. With $h = 120\ mm$, a good agreement between the simulation return loss of the antenna and the antenna with the rectangular copper sheet is observed, as shown in Figure 5-8.

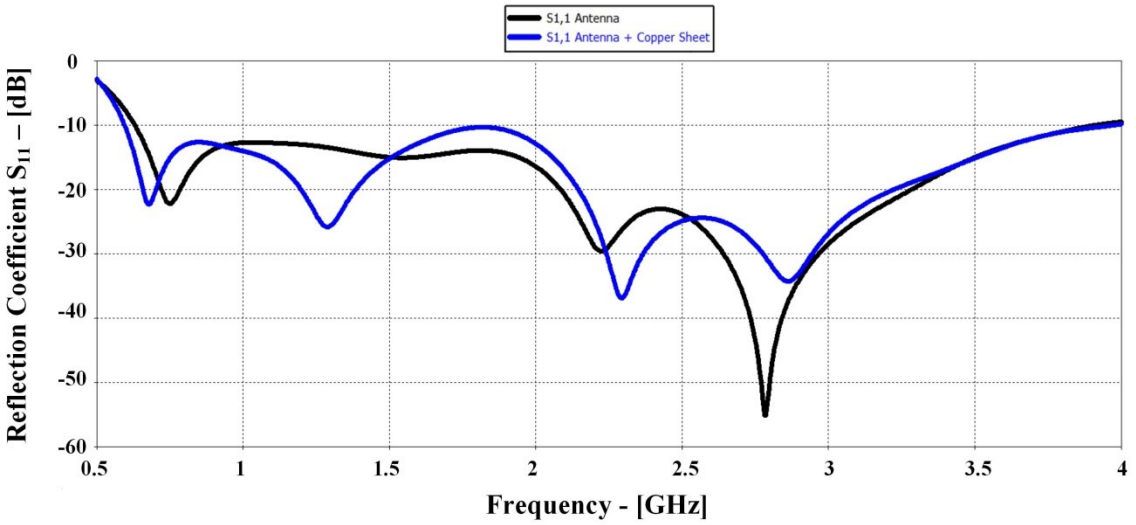

Figure 5-8 Reflection coefficient of the proposed antenna with and without copper sheet

The antenna patterns for electric and magnetic fields with and without the copper reflector were simulated over the operating band. The antenna patterns at 0.7 GHz, 1.3 GHz, 1.9 GHz and 3 GHz frequencies are plotted, respectively, in Figure 5-9 to Figure 5-12.

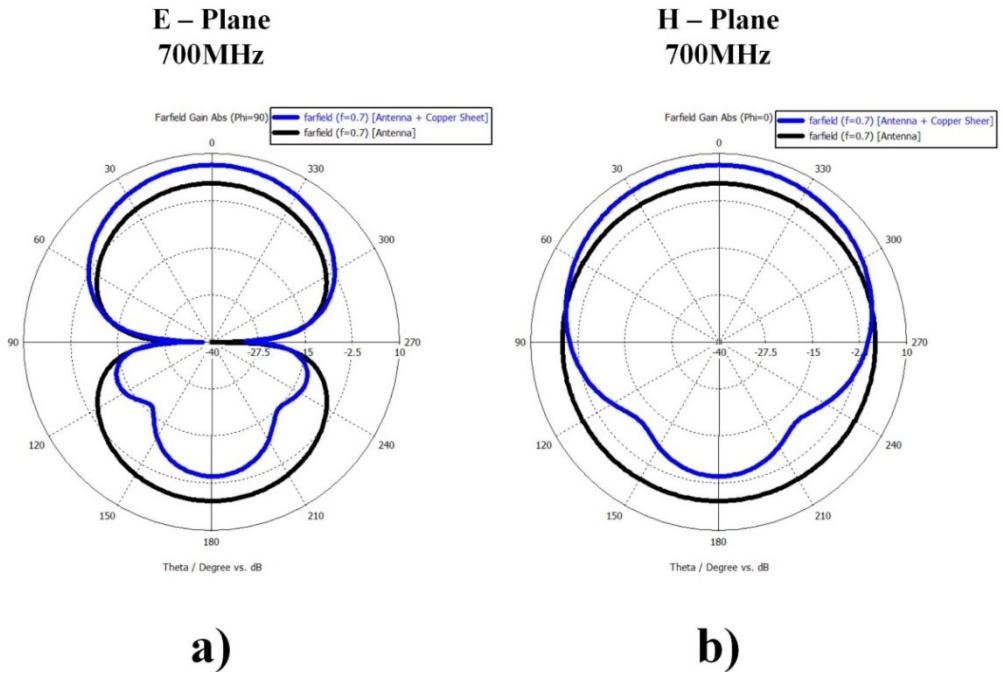

Figure 5-9 Simulated radiation patterns in (a) E-cut plane and (b) H-cut plane of the proposed antenna with and without copper sheet at 0.7 GHz

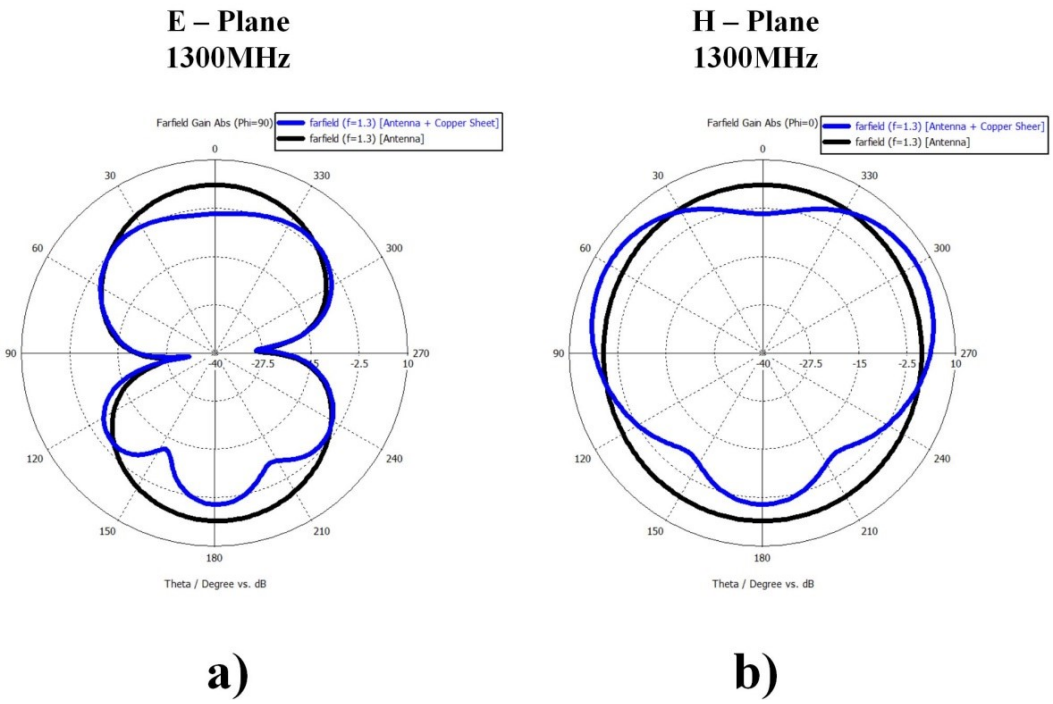

Figure 5-10 Simulated radiation patterns in (a) E-cut plane and (b) H-cut plane of the proposed antenna with and without copper sheet at 1.3 GHz

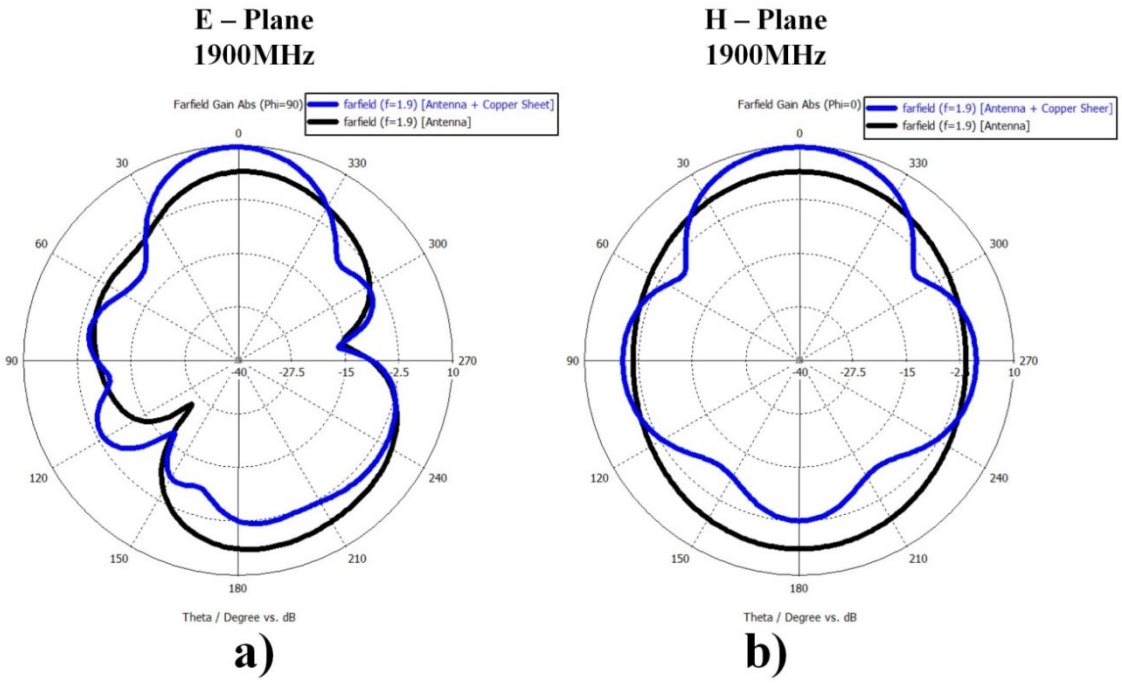

Figure 5-11 Simulated radiation patterns in (a) E-cut plane and (b) H-cut plane of the proposed antenna with and without copper sheet at 1.9 GHz

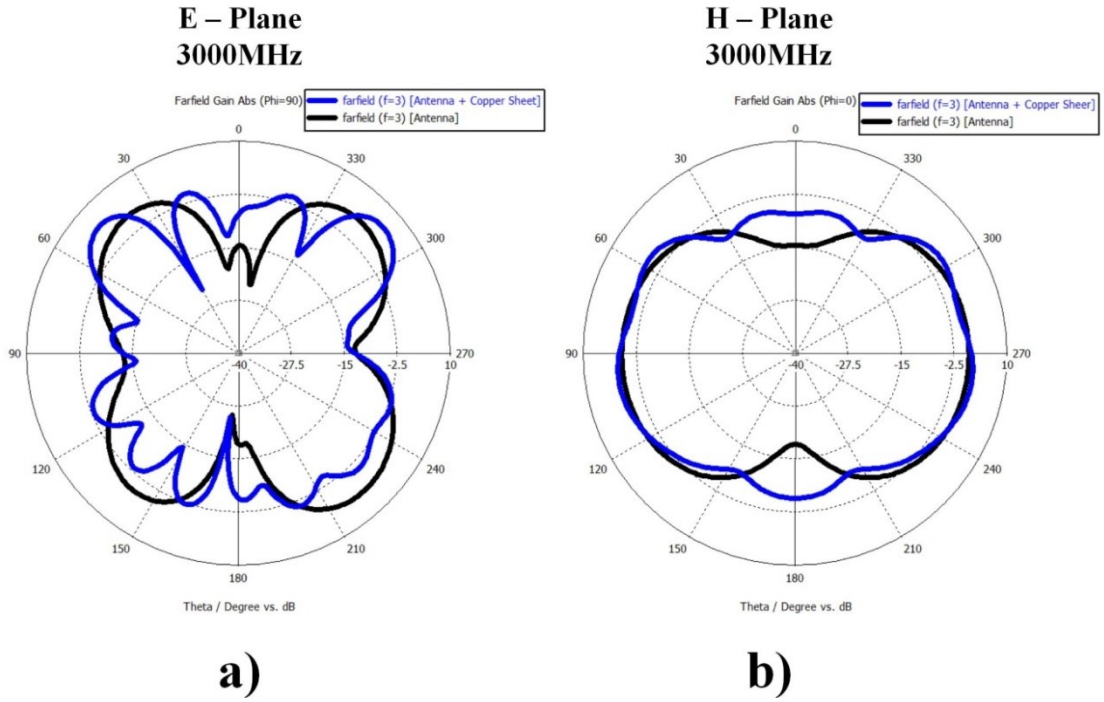

Figure 5-12 Simulated radiation patterns in (a) E-plane and (b) H-cut plane of the proposed antenna with and without copper sheet at 1.9 GHz

The antenna radiation patterns have a relatively low side lobe, with no tilting up to around 1.9 GHz. The copper sheet reflects radiation back and increases the gain of the antenna. The gain of the proposed antenna with and without the reflector sheet is plotted in Figure 5-13. The maximum gain improvement of 6dB is achieved at 1.7 GHz. However, this gain enhancement is not consistent for the entire operating bandwidth due to the wavelength changes with frequencies.

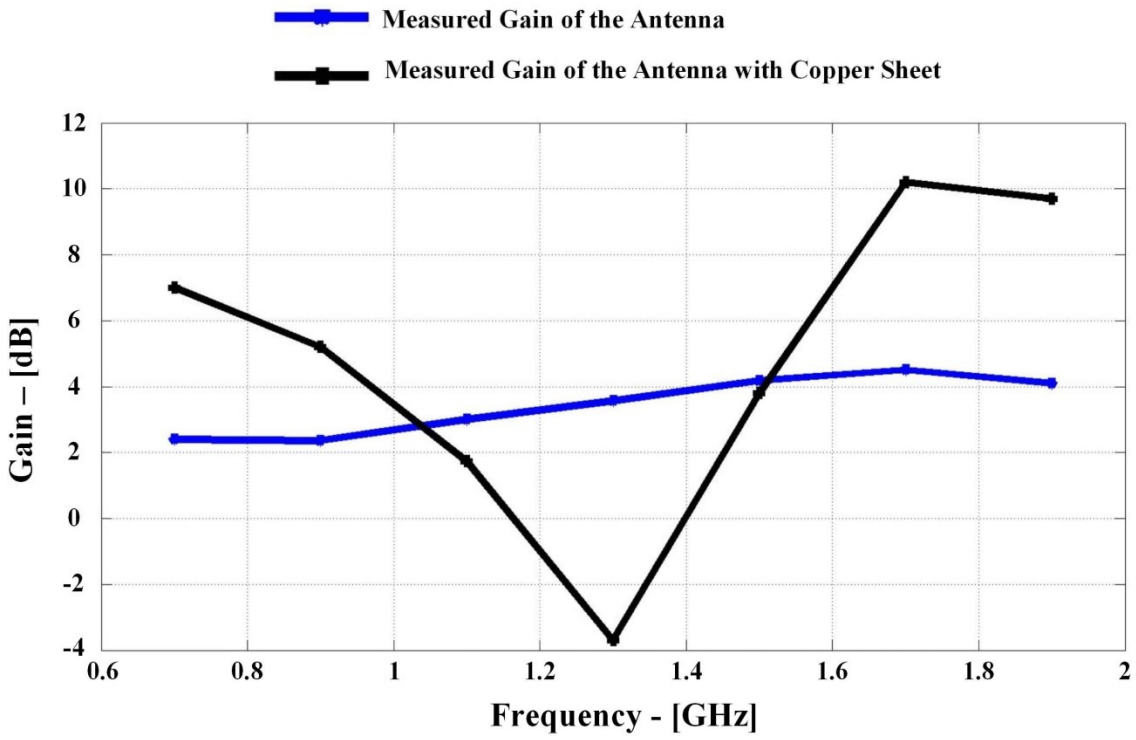

Figure 5-13 Simulated gain of the antenna with and without copper sheet

5.3.3 Antenna with double-layer FSS

As can be clearly seen from Figure 5-10 and Figure 5-13, the rectangular copper sheet is not a suitable reflector for the proposed planar dipole in terms of both radiation pattern and gain. Moreover, a 120 mm distance between the antenna and reflector is too large to render the antenna 'low-profile'. In order to decrease this distance and have in-phase reflection, with radiation present only on one side of the antenna with enhanced radiation

directivity and gain, a double-layer frequency selective surface is then employed to replace the copper reflector as shown in Figure 5-14.

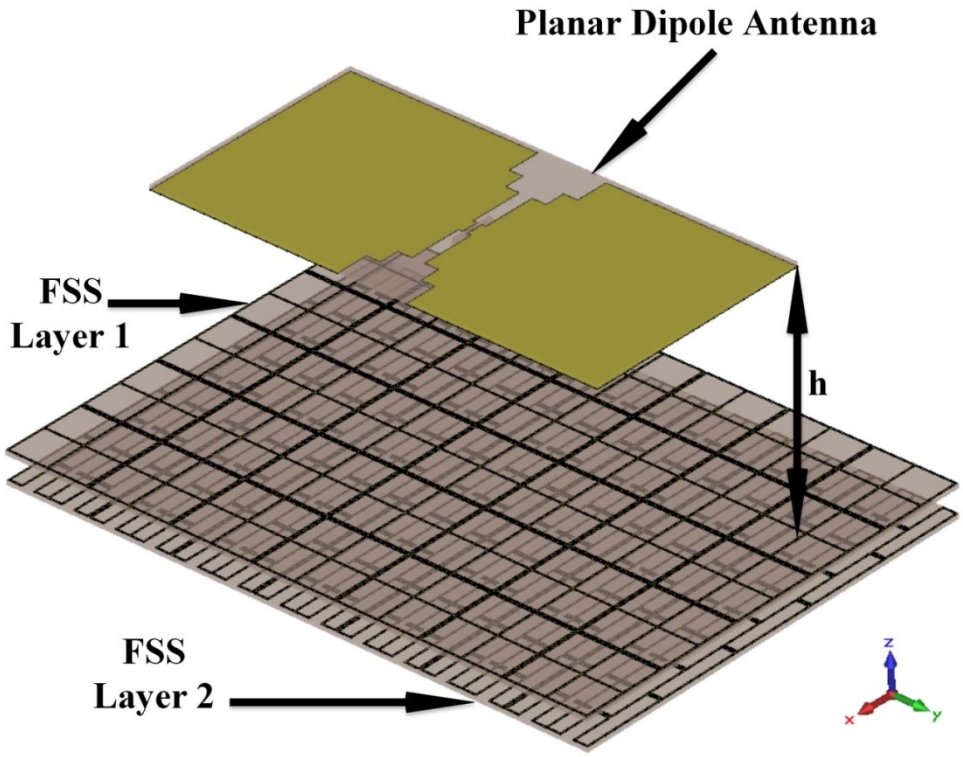

Figure 5-14 Proposed planar dipole antenna backed with double-layer FSS

The double-layer FSS consists of two separate layers with a spacing of 8 mm between them. Each layer has seven by nine unit cells of 30 mm by 30 mm each; with the overall size of 210 mm by 270 mm (the scattering parameters of layer-1 and layer-2 are studied in subsection 4.3). h is swept from 50 mm to 80 mm in order to obtain its optimum lowest value. The simulated return loss results for h are shown in Figure 5-15.

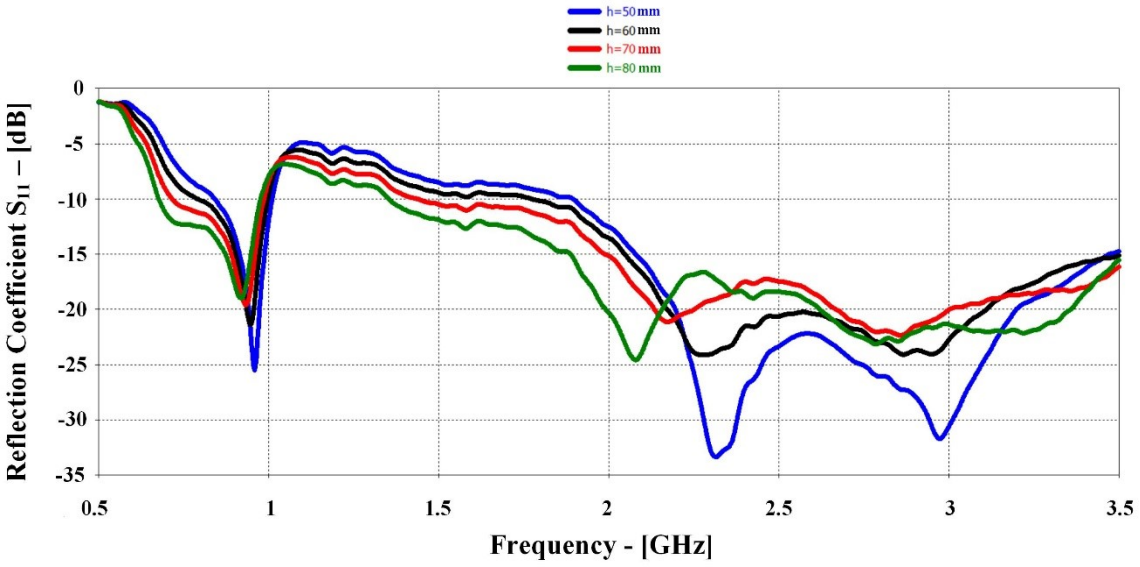

Figure 5-15 Reflection coefficient of the proposed antenna with double-layer FSS for parameter h

The return loss of the antenna is poor between 1 GHz to 2 GHz for different values of h. To resolve it, an additional resonance is created. The antenna is loaded with a resonant element (LC-Tank and chip resistors) on each arm of the antenna.

5.3.4 Loaded antenna with double-layer FSS

The open complementary double concentric split-hexagonal-ring resonators (LC-Tank) and chip resistors are now incorporated into the planar dipole antenna. By choosing the appropriate size and location for the LC-tanks, an additional resonance is created to yield greater return loss of the antenna. The theory, geometry design and equivalent circuit of this LC-loading technique are explained before in 3.2 and 4.2, respectively. The complete schematics of the proposed planar dipole antenna loaded with split-hexagonal-ring resonators and chip resistors, and backed with the double-layer FSS is illustrated in Figure 5-16.

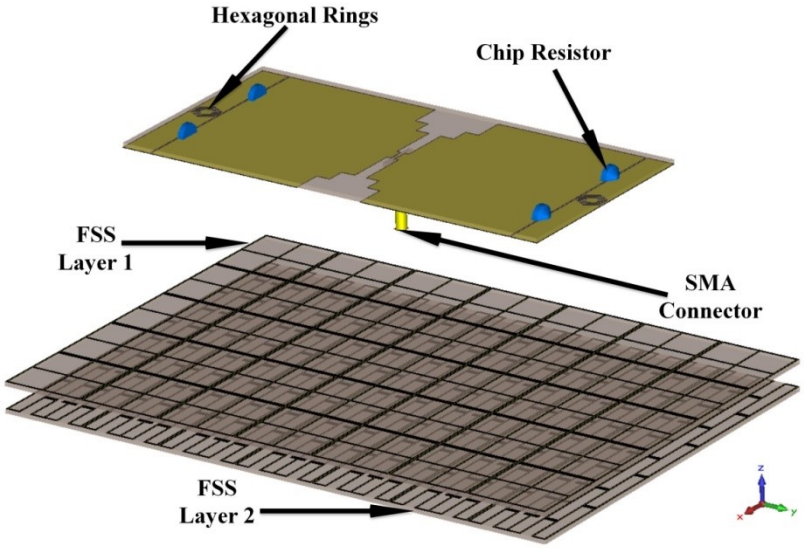

Figure 5-16 Loaded planar dipole antenna backed with double-layer FSS

The reflection coefficient of the antenna with and without the LC-Tanks are shown in Figure 5-17. The rings created an additional resonance for the antenna to cover the entire bandwidth.

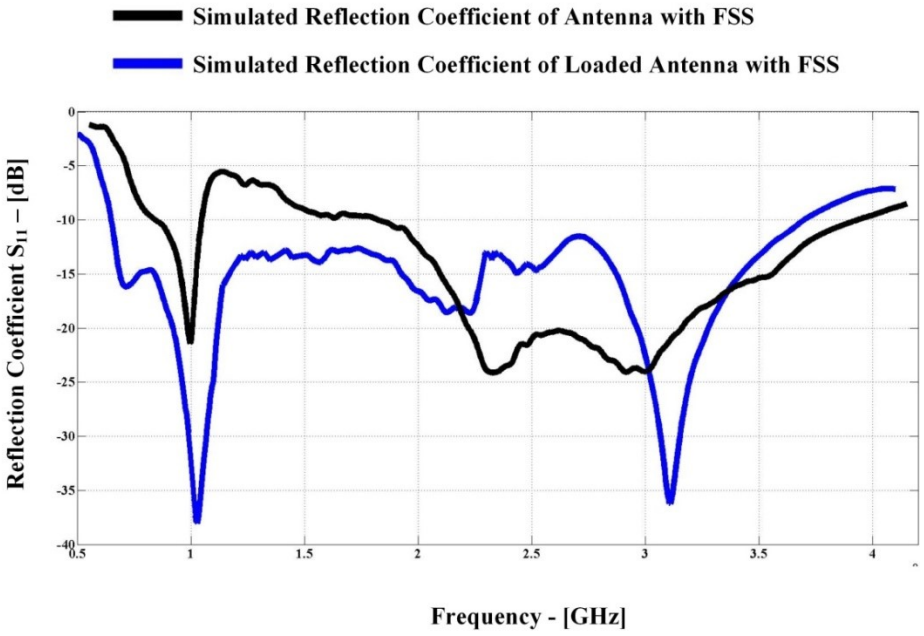

Figure 5-17 Reflection coefficient of the original antenna and loaded antenna with double-layer FSS

The reflection coefficient of the proposed loaded antenna backed with the double-layer FSS is compared with the reflection coefficient of the planar dipole antenna backed with the reflector copper sheet. The results of this simulation are presented in Figure 5-18.

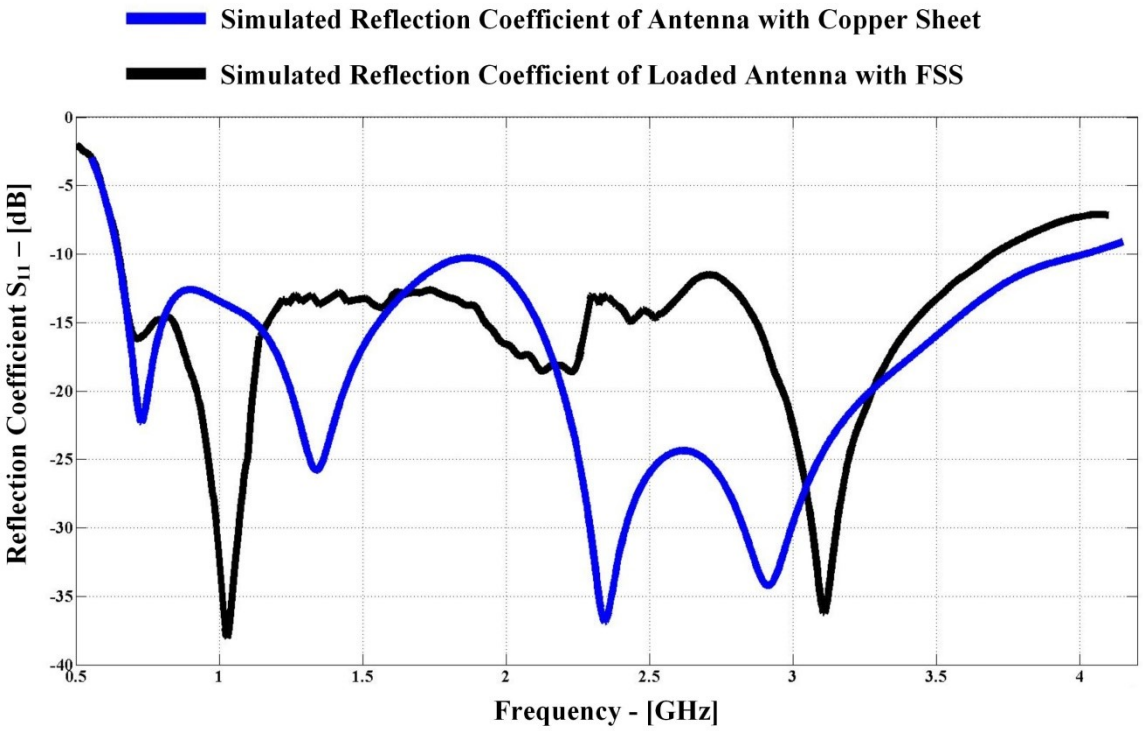

Figure 5-18 Reflection coefficient of the proposed antenna with copper sheet and proposed double-layer FSS

The simulation return loss shows 144% and 141% of the operating bandwidth for the planar dipole antenna with copper sheet and loaded planar dipole antenna with double-layer FSS, respectively. Both designs have the same starting frequency point at 630 MHz

Radiation patterns of the planar dipole antenna and the LC-loaded planar dipole antenna with the copper sheet and proposed double-layer FSS were simulated over the operating band, respectively. The antenna patterns at 0.7 GHz, 1.4 GHz, 1.9 GHz and 3 GHz frequencies are plotted, respectively, in Figure 5-19 to Figure 5-22.

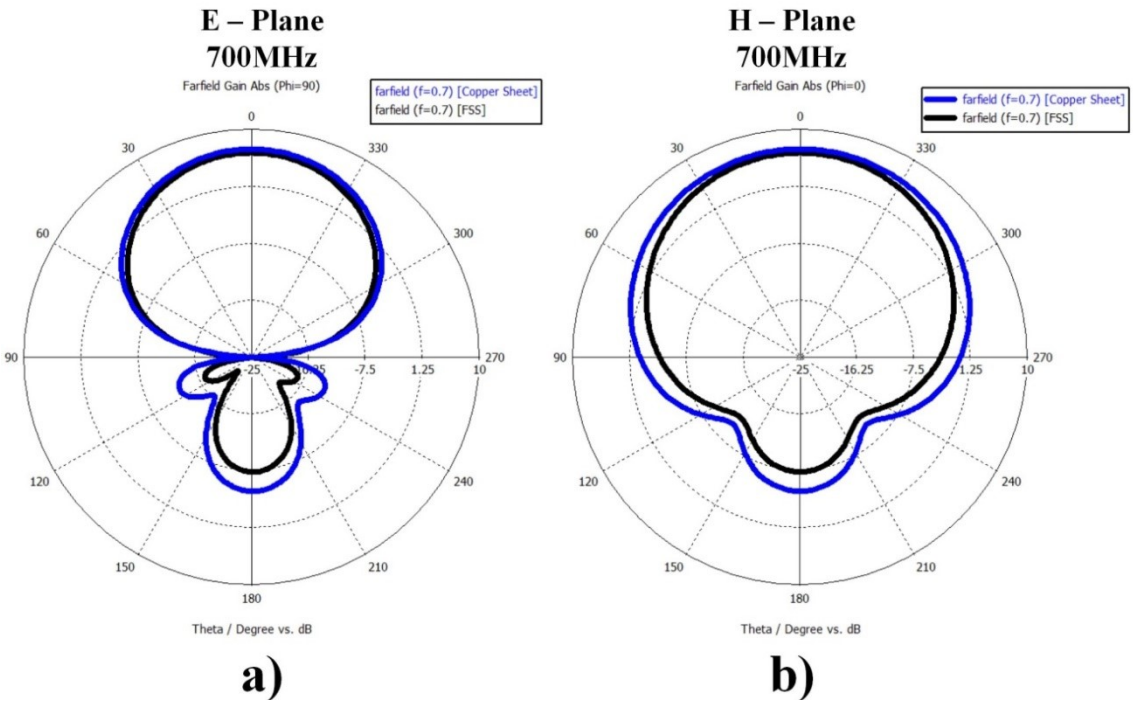

Figure 5-19 Simulated radiation patterns in (a) E-cut plane and (b) H-cut plane of the proposed antenna with copper sheet and double-layer FSS at 0.7 GHz

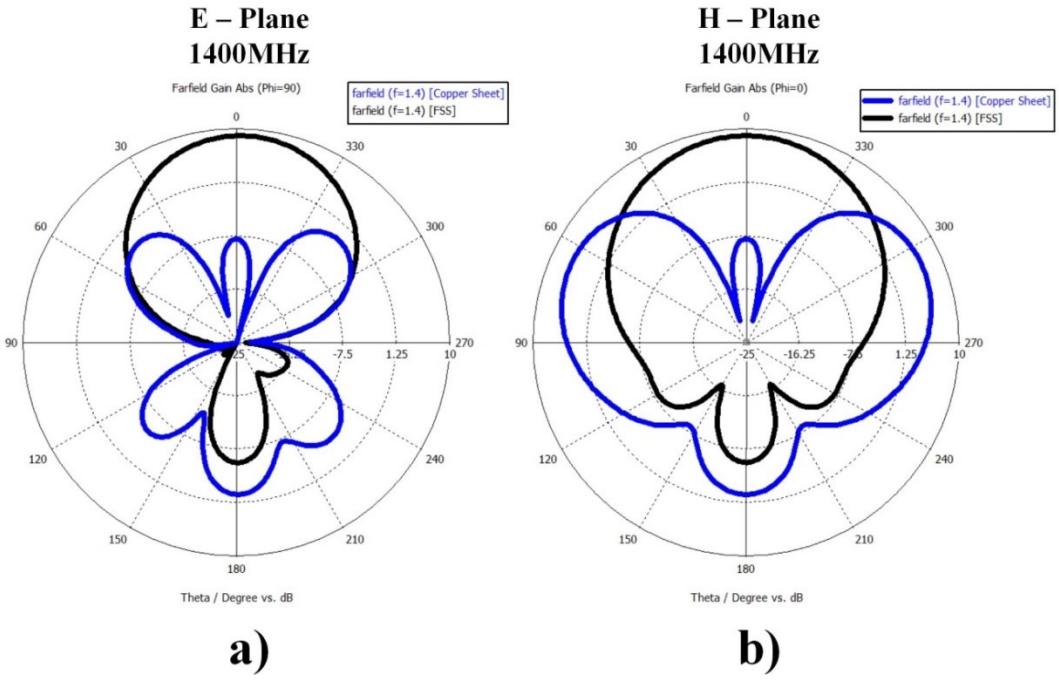

Figure 5-20 Simulated radiation patterns in (a) E-cut plane and (b) H-cut plane of the proposed antenna with copper sheet and double-layer FSS at 1.4 GHz

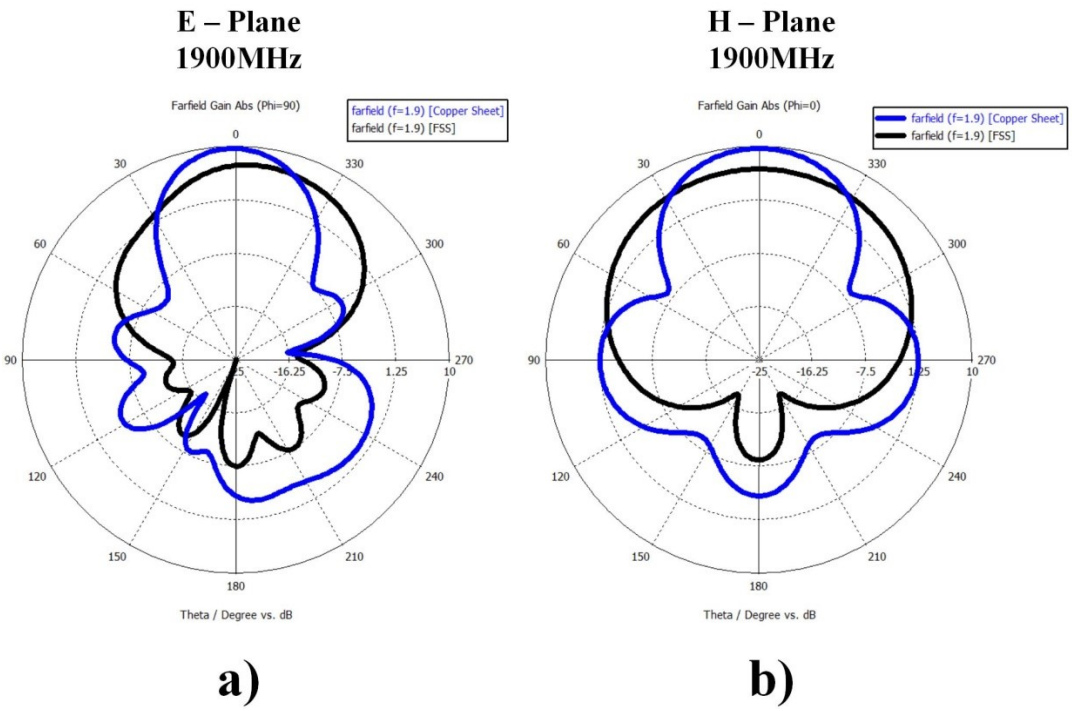

Figure 5-21 Simulated radiation patterns in (a) E-cut plane and (b) H-cut plane of the proposed antenna with copper sheet and double-layer FSS at 1.9 GHz

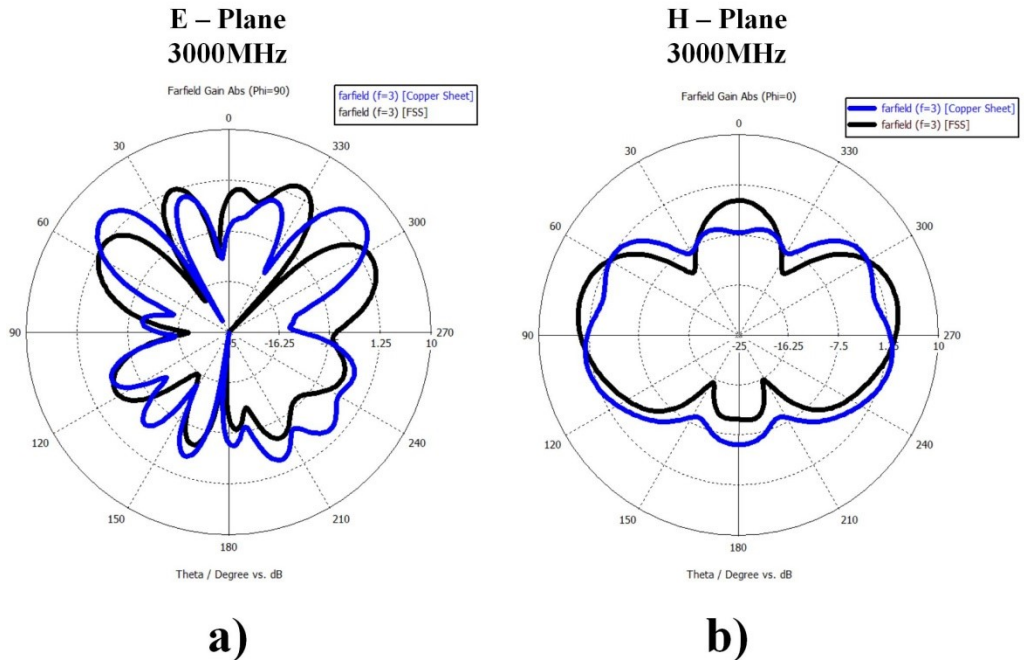

Figure 5-22 Simulated radiation patterns in (a) E-cut plane and (b) H-cut plane of the proposed antenna with copper sheet and double-layer FSS at 3 GHz

In comparisons of radiation patterns, it can be clearly seen that use of the double-layer FSS leads to a significantly better performance than with the copper sheet. Figure 5-20 shows that the antenna with the copper sheet reflector in the back has very large side lobe levels around 1.4 GHz. This drawback is due to out-of-phase reflections from the copper sheet and the cross-talk between the copper sheet and the antenna; they cause non-uniform, asymmetric and frequency dependent phase distribution at the maximum radiation direction of the antenna. Consequently, the out-of-phase reflection effects lead to a significant drop in the gain of the dipole antenna around this frequency (see Figure 5-13). The radiation patterns of the antenna with the copper sheet contrast sharply with proposed double-layer FSS; the latter gives a symmetric radiation pattern with a constant direction of maximum radiation. This characteristic is crucial for most radar applications [56].

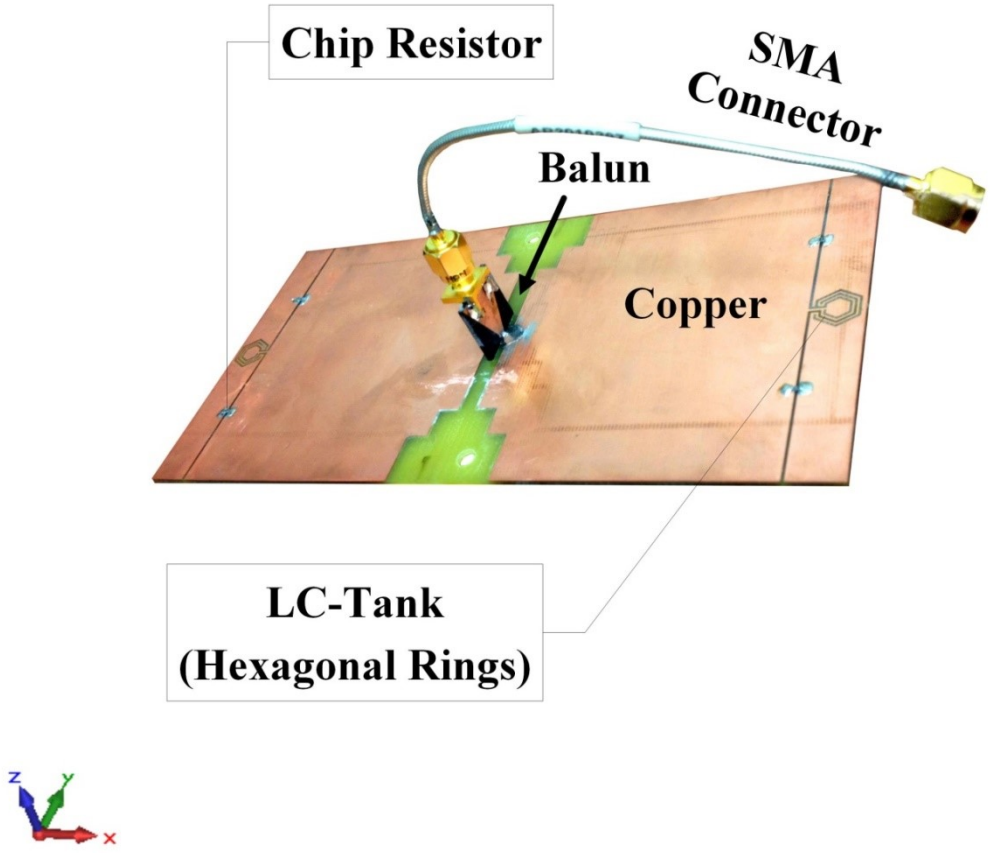

Figure 5-23 Fabricated planar dipole antenna loaded with LC-Tank and chip resistors

The proposed planar dipole antenna loaded with hexagonal rings (LC-Tanks) and chip resistors is fabricated on a FR4 substrate and fed via the proposed wideband microstrip line to parallel strip line transformer (balun). A rectangular cavity was etched out from the center of the antenna's substrate, and the balun inserted into this gap. The fabricated antenna fed with balun and an SMA connector is shown in Figure 5-23.

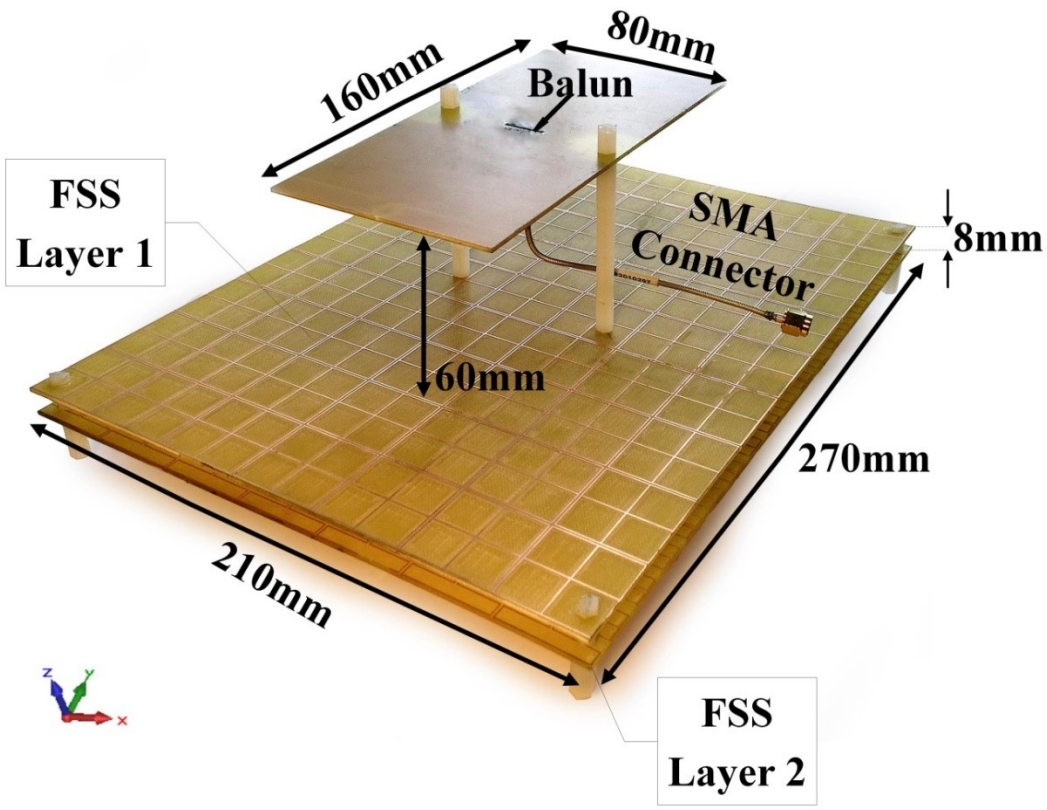

Figure 5-24 Fabricated loaded antenna with the proposed double-layer FSS

Both layer one and layer two were fabricated on FR4 substrate and stacked together with an 8 mm gap between them. The fabricated antenna and the double-layer FSS were assembled via two nonconductive (plastic) posts with a length of 60 mm. A prototype of the design is illustrated in Figure 5-24.

The measured and simulated reflection coefficient of the loaded antenna are shown in Figure 5-25, where a good agreement between the measurements and simulations is observed. The measured reflection coefficient was less than -10 dB over 0.63 GHz to 3.8GHz.

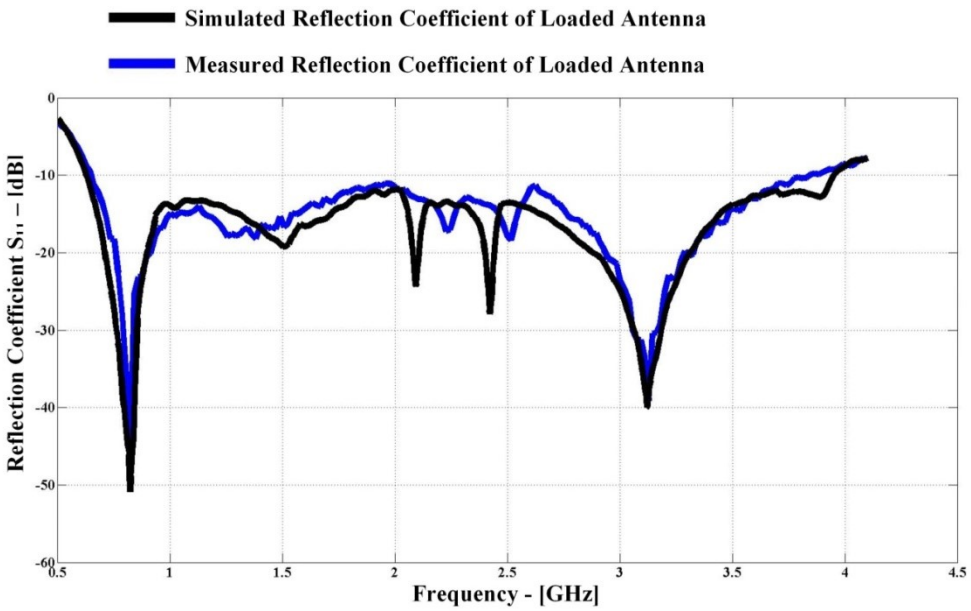

Figure 5-25 Simulated and measured reflection coefficient of the loaded antenna

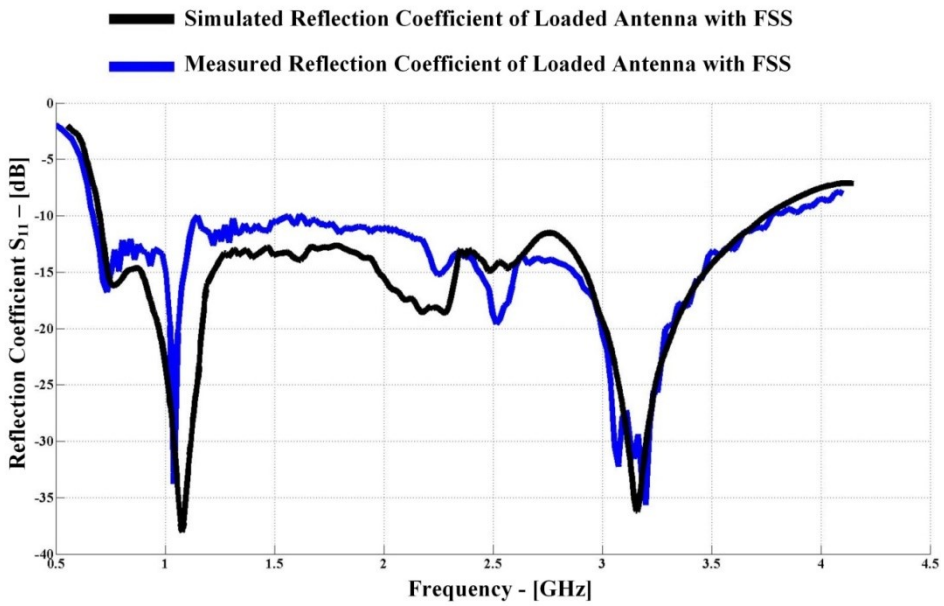

Figure 5-26 Simulated and measured reflection coefficient the loaded antenna with FSS

Figure 5-26 illustrates the simulated and measured reflection coefficient of the loaded planar dipole antenna with the dual-layer FSS reflector. The measured impedance bandwidth of the double layer FSS is from 0.65 GHz to 3 GHz (Figure 4-9). This correlates exceedingly well with the return loss of the antenna from 0.63 GHz to 3.8GHz. Acceptable differences between the simulated and measured results are seen and they are probably due to fabrication error and simulation assumption.

The measured and theoretical gain of the loaded antenna with and without the double-layer FSS reflector is shown in Figure 5-27, respectively. The measurement results validate that the proposed planar dipole antenna with the double-layer FSS performs efficiently and has the gain improvement. The measured gain of the antenna without the FSS ranges from 2.2 dBi to 4 dBi, while the measured gain of the antenna with the double-layer FSS reflector ranges from 6.2 dBi to 9 dBi. An average 4 dBi gain enhancement over the entire operational band of the antenna is observed, in contrast to the 2 dBi gain enhancement presented in [52].

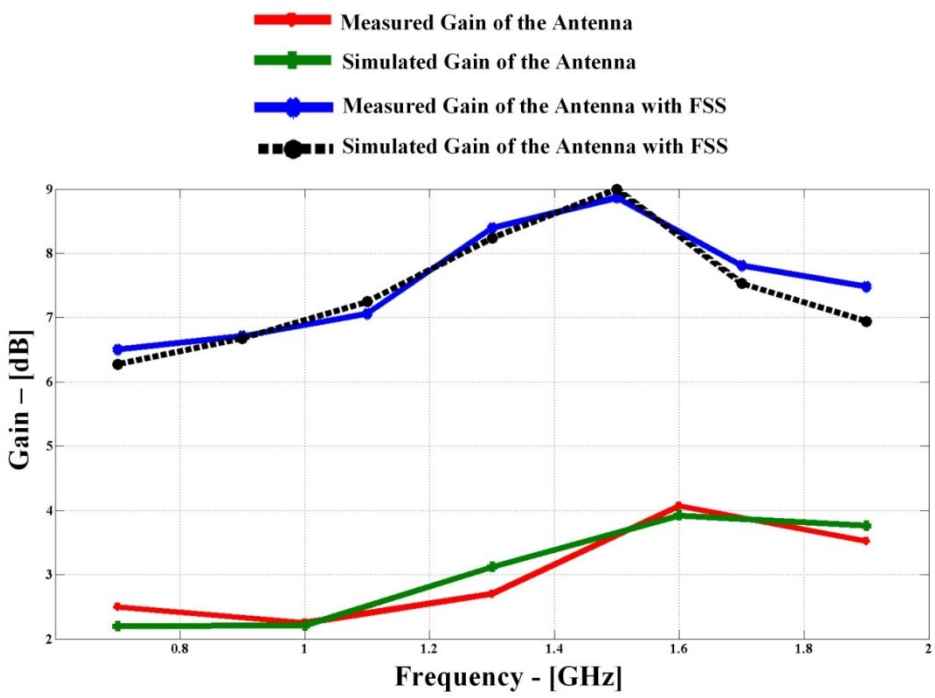

Figure 5-27 Simulated and measured gain of the loaded antenna with and without the proposed double-layer FSS

Figure 5-28 to Figure 5-30 depict the measured and simulated E-plane and H-plane radiation patterns of the proposed planar dipole antenna. Figure 5-31 to Figure 5-33 characterize the measured and simulated E-plane and H-plane radiation patterns of the proposed planar dipole antenna with dual-layer FSS at 0.7 GHz, 1.3 GHz and 1.9 GHz, respectively. There is good agreement between the simulation and measurement results, where the antenna has relatively low side lobe levels up to1.9 GHz. As the frequency increases above 2 GHz, the patterns tilt and have growing side lobes. The slight difference between the simulation and measurement results in radiation patterns may have been caused by the electromagnetic leaking of coaxial feeding wire and the drift errors of the scanner, which could not be taken into account in the simulations.

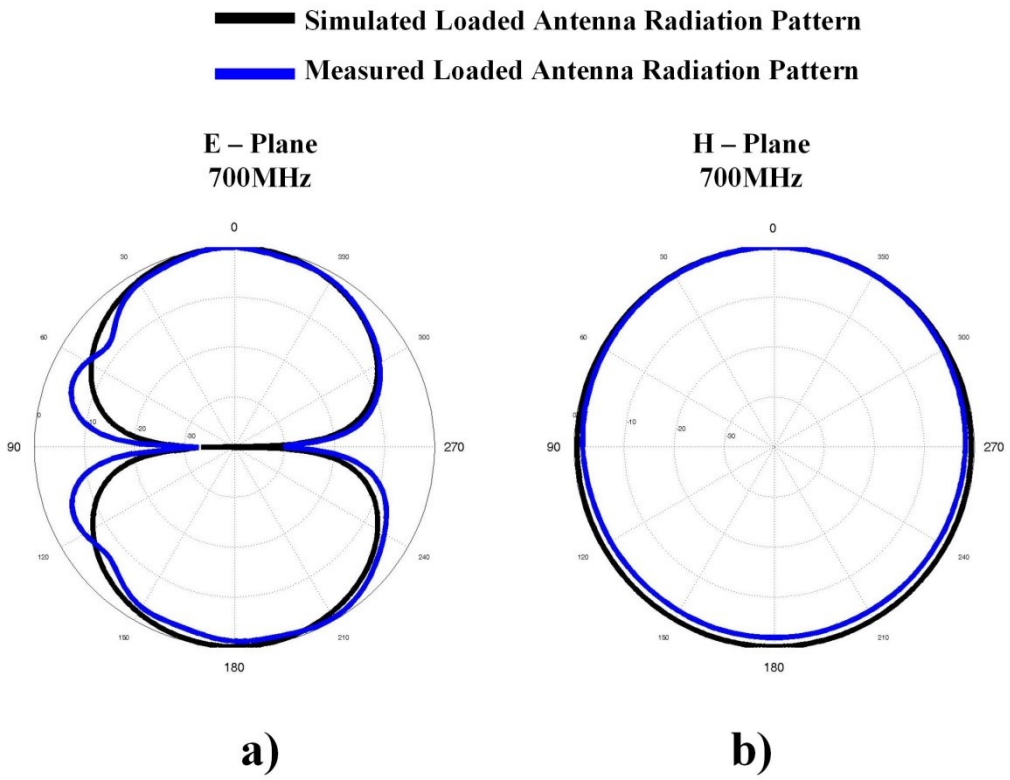

Figure 5-28 Simulated and measured radiation patterns in (a) E-cut plane and (b) H-cut plane of the loaded antenna at 0.7 GHz

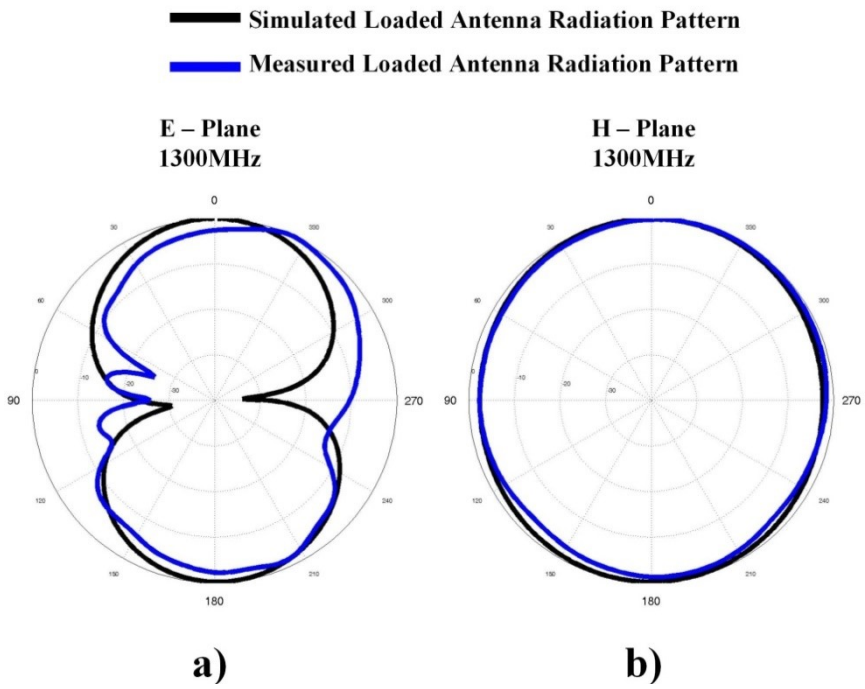

Figure 5-29 Simulated and measured radiation patterns in (a) E-cut plane and (b) H-cut plane of the loaded antenna at 1.3 GHz

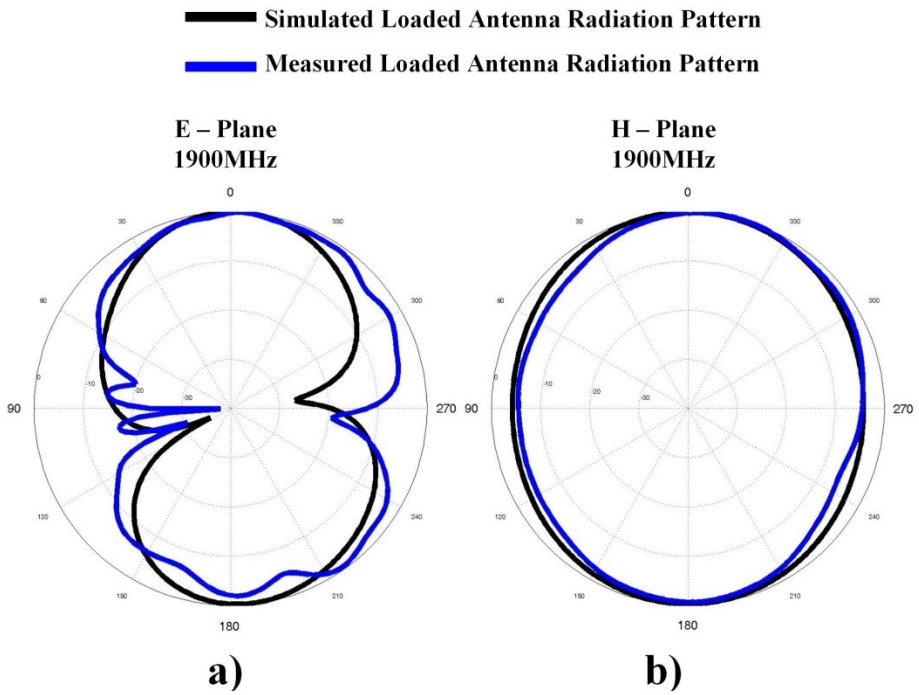

Figure 5-30 Simulated and measured radiation patterns in (a) E-cut plane and (b) H-cut plane of the loaded antenna at 1.9 GHz

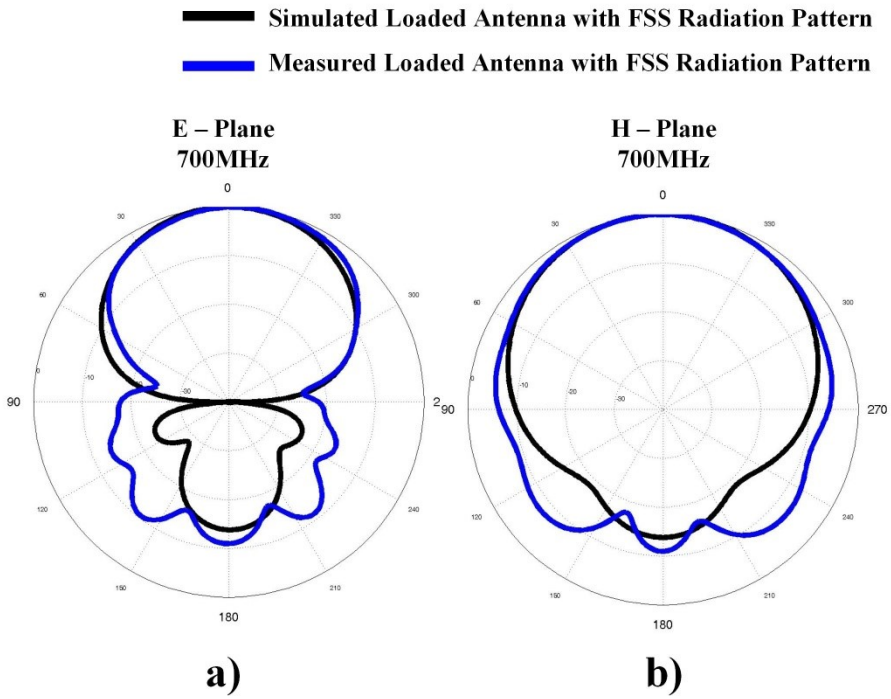

Figure 5-31 Simulated and measured radiation patterns in (a) E-cut plane and (b) H-cut plane of the loaded antenna with the double-layer FSS at 0.7 GHz

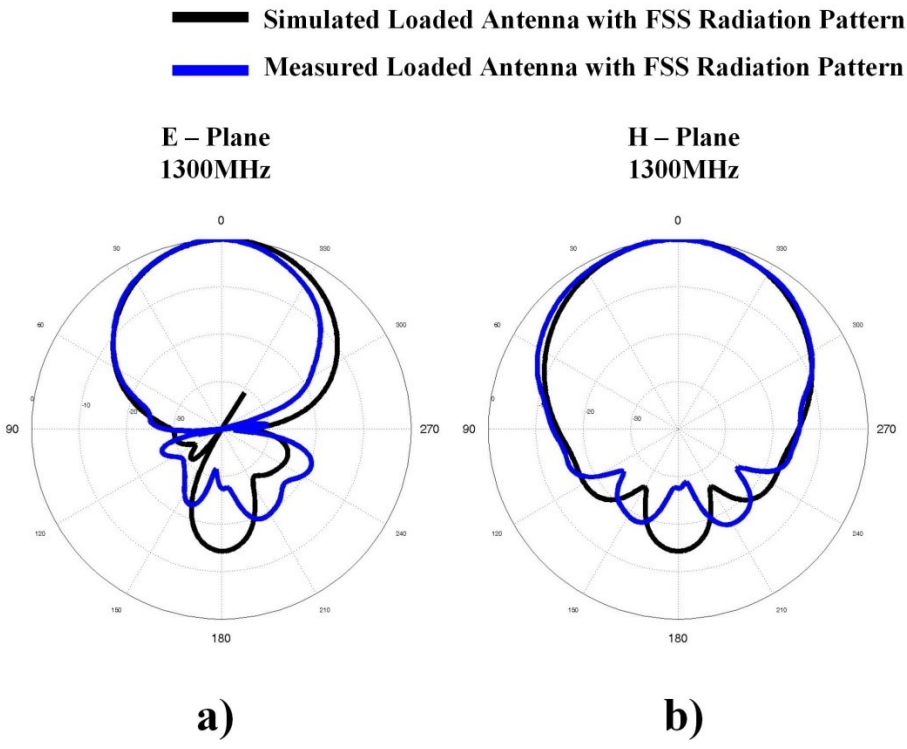

Figure 5-32 Simulated and measured radiation patterns in (a) E-cut plane and (b) H-cut plane of the loaded antenna with the double-layer FSS at 1.3 GHz

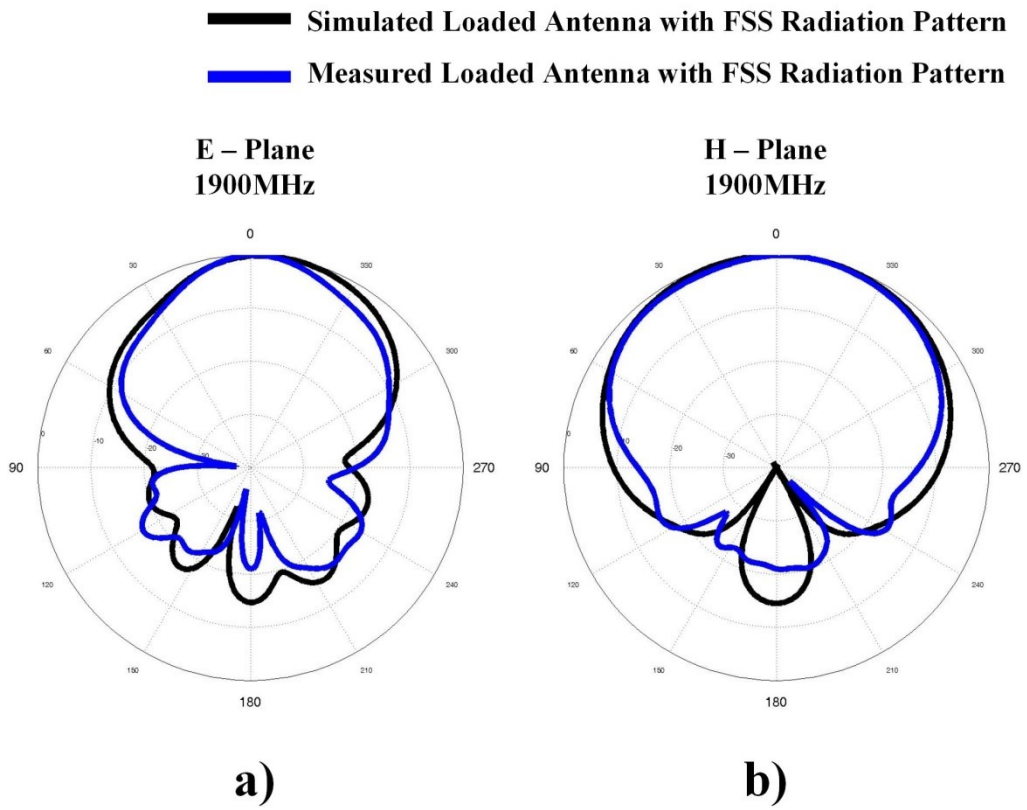

Figure 5-33 Simulated and measured radiation patterns in (a) E-cut plane and (b) H-cut plane of the loaded antenna with the double-layer FSS at 1.9 GHz

Table II lists the half-power beamwidth (HPBW) of different designs over a frequency range of 0.7 GHz to 1.9 GHz. The table illustrates a comparison among the antenna, loaded antenna with LC-Tank and resistors, antenna with copper sheet and loaded antenna with double-layer FSS. As can be seen, the HPBW for the loaded antenna decreases gradually over the operating bandwidth, and exhibits a good agreement with the design of the unloaded antenna. Despite the antenna with copper sheet having wider HPBW compared with the loaded antenna with FSS at the low operational frequency, the HPBW drops abruptly around 1.3 GHz and has narrow HPBW for the rest of operating bandwidth. In comparison, the loaded antenna with the double-layer FSS exhibits more linearly decreasing HPBW.

Table II Half-power bandwidth table [Angle]

Frequency [GHz]	**Antenna**	**Loaded Antenna**	**Antenna with Copper Sheet**	**Loaded Antenna with FSS**
0.7	81.7˚	82.2˚	71.9˚	68.2˚
0.9	76.4˚	77.6˚	74.8˚	60˚
1.1	70.2˚	72.3˚	83.5˚	63.3˚
1.3	64.2˚	66.8˚	28.5˚	51.2˚
1.5	58.4˚	61.6˚	28.5˚	45.3˚
1.7	53.6˚	57˚	34.2˚	61.2˚
1.9	51.1˚	55˚	36.4˚	53˚

Table III contains comparisons of operating bandwidth and size between the proposed loaded antenna and those presented in [56], [57], [52] and [58], respectively. A significant size reduction is observed with the proposed loaded antenna.

Table III Performance comparison between the proposed and referenced antennas

	In this work	**Reference** [56]	**Reference** [57]	**Reference** [52]	**Reference** [58]
Impedance Bandwidth	138%	128%	110%	122%	92%
Area (λ^2)	0.0598	0.1485	0.5336	0.1764	0.1075
Height (λ)	0.13	0.18	0.283	0.11	0.155

Chapter 6 CONCLUSION AND FUTURE WORK

6.1 Conclusion

In this thesis, LC-Tanks, chip resistors and a dual-layer FSS are incorporated into the planar dipole to construct a size-reduced, bandwidth and gain-enhanced UWB antenna for radar and communication systems. A microstrip to parallel plate transformer is used to feed the proposed UWB antenna, and provides impedance matching over the entire operational bandwidth of the antenna. The measurement results show that the proposed planar dipole antenna is a very good candidate for radar and communication applications that require directive radiation patterns, high gains, low fabrication cost, lightweight structures, and compact size.

6.2 Future Work

The proposed UWB antenna has good potential for mass fabrication for commercial ground-penetrating radar applications. For the future work, transmitter and receiver antennas can be simulated and measured in the presence of ground effects so performance of the entire system can be assessed in an environment that is close to real-life. As well, further experimental tests are needed in terms of the use of the antenna for impulse signal processing and image processing.

REFERENCES

[1] L. B. Conyers and D. Goodman, *Ground Penetrating Radar: An Introduction for Archaeologists*. Altimira Press, Walnut Creek, 1997.

[2] G. Grandjean, J. C. Gourry, and A. Bitri, "Evaluation of GPR techniques for civil-engineering applications: study on a test site," *Appl. Graph.*, vol. 45, no. 3, pp. 141-156, 2000.

[3] D. J. Daniels, *Ground penetrating radar*. vol. 1, let. 2004.

[4] R. S. Cloude and K. P. Papathanassi, "Polarimetric SAR interferometry," *IEEE Trans.*, vol. 36, no. 5, pp. 1551-1565, 1998.

[5] T. Khuut, *Application of Polarimetric GPR to detection of subsurface objects*. Ph.D. dissertation, Dept. Elect. Eng. Tohoku Univ., 2009.

[6] D. Uduwawala, *A comprehensive study of resistor-loaded planar dipole antennas for ground penetrating radar applications*. Stockholm, Sweden: Ph.D. dissertation, Dept. Elect. Eng., Royal Inst. of Tech., 2006.

[7] A. G. Roberto and G. D. Rogerson, "Ultra-wideband wireless systems," *Microw. Mag.*, vol. 4.2, pp. 36-47, 2003.

[8] N. Cravotta. (2002, Oct.) [Online] www.edn.com.

[9] I. Oppermann, M. Hamalainen, and J. Iinatti, *UWB Theory and Applications*. John Wiley & Sons, Ltd., 2004.

[10] M. Pausini, *Autocorrelation Receivers for Ultra Wideband Wireless Communications*. Ph.D. dissertation, Dept. Elect. Eng., Delft Univ. of Tech., pp. 10-12, 2007.

[11] Federal Communications Commission, "In the Matter of Revision of Part 15 of the Commission's Rules Regarding Ultra-Wideband Transmission Systems," 1st Rep. and Order in ET Docket 98-153, 2002.

[12] B. Allen and et al., *Ultra-wideband Antennas and Propagation for Communications, Radar and Imaging*. Wiley, 2007.

[13] D. K. Cheng, *Field and Wave Electromagnetics*, 2nd, Ed. Addison-Wesley, 1989.

[14] M. N. Sadiku, *Numerical Techniques in Electromagnetics*, 2nd ed. CRC Press LLC, 2000.

[15] IEEE Trans. on Antennas and Propag., Vols. AP-17, No. 3, May 1969; Vol. AP-22, No. 1, Jan. 1974; and Vol. AP-31, No. 6, Part II, Nov. 1983.

[16] M. Skolnik, *Radar Handbook*, 2nd ed. McGraw-Hill, 1990.

[17] C. A. Balanis, *Antenna Theory Analysis and Design*, 3rd ed. Wiley-Interscience, 2005.

[18] J. Powell, *Antenna Design for Ultra Wideband Radio*. M.S. thesis, Dept. Electron. Massachusetts Instit. of Tech. ,Cambridge, 2004.

[19] M. Karlsson, *Ultra-wideband Antenna and Radio Front-end Systems*. Norrköping, Sweden: M.S. thesis, Dept. of Sci. and Tech., Linköping University, 2007.

[20] V. F. Fusco, *Foundations of Antenna Theory and Techniques*. Edinburgh Gate, Harlow, Essex, England, Pearson Educ. Limited, 2005.

[21] S. Licul, et al., "A parametric study of time-domain characteristics of possible uwb antenna architectures," *IEEE 58th Vehicular Tech. Conf.*, p. 3110–3114, 2003.

[22] R. DuHamel and D. Isbell, "Broadband logarithmically periodic antenna structures," *IRE Int. Conv. Rec.*, vol. 5, pp. 119-128, Mar. 1957.

[23] A. T. Almutawa, *Log-Periodic Microstrip Patch Antenna Miniaturization Using Artificial Magnetic Conductor Surfaces*. M.S. thesis, Dept. Electron.,South Florida Univ., 2011.

[24] P. S. Hall, "Bandwidth limitations of log-periodic microstrip patch antenna arrays," *Electron. Lett.*, vol. 20, no. 11, pp. 437-438, May 1984.

[25] P. J. Gibson, "The vivaldi aerial," *the 9th European Microw. Conf.*, pp. 101-105, 1979.

[26] E. Gazit, "Improved design of the vivaldi antenna," *Proc. of Inst. of Elect. Eng.*, vol. 135, no. 2, pp. 89-92, 1988.

[27] J. Langley, P. Hall, and P. Newham, "Novel ultrawide-bandwidth vivaldi antenna with low crosspolarisation," *Electron. Lett.*, vol. 29, no. 23, pp. 2004-2005, 1993.

[28] M. Chiappe and G. L. Gragnani, "Vivaldi antennas for microwave imaging: Theoretical analysis and design considerations," *Instrum. Meas. IEEE Trans.*, vol. 55, no. 6, pp. 1885-1891, 2006.

[29] H. Azodi, *UWB Air-Coupled Antenna for Ground Penetrating Radar*. M.S. thesis, Dept. Electron. Delft Univ., 2010.

[30] A. C. Mak, C. R. Rowell, R. D. Murch, and C. L. Mak, "Reconfigurable Multiband Antenna Designs for Wireless Communication Devices," *IEEE Trans. Antennas Propag.*, vol. 55, no. 7, pp. 1919-1928, Jul. 2007.

[31] Y. Sung, "Bandwidth Enhancement of a Microstrip Line-Fed Printed Wide-Slot Antenna With a Parasitic Center Patch," *IEEE Trans. Antennas Propag.*, vol. 60, no. 4, pp. 1712-1716, Apr. 2012.

[32] M. H. C. Dias and J. C. A. Santos, "Practical design of a broadband modified monopole by the use of staircase parasitic rings," *Micro.& Optoelectronics Conf. (IMOC), SBMO/IEEE MTT-S Int. IEEE*, 2011.

[33] Lee, Wang-Sang, Dong-Zo Kim, Ki-Jin Kim, and Jong-Won Yu, "Wideband planar monopole antennas with dual band-notched characteristics," *IEEE Trans. Microw. Theory Tech.*, vol. 54, no. 6, pp. 2800-2806, Jun. 2006.

[34] Yong-Xin Guo, Chia, M. Y W, and Zhi Ning Chen, "Miniature built-in multiband antennas for mobile handsets," *IEEE Trans. Antennas Propag.*, vol. 52, no. 8, pp. 1936-1944, Aug. 2004.

[35] H. Wang and M. Zheng, "Triple-band wireless local area network monopole antenna," *Microw. Antennas & Propag., IET*, vol. 2, no. 4, pp. 367-372, Jun. 2008.

[36] V. Stoiljkovic, S. Suganthan, and M. Benhaddou, "A novel dual-band centre-fed printed dipole antenna," *IEEE Antennas and Propag. Society Int. Symp.*, vol. 2, pp. 938-941, Jun. 2003.

[37] C.-M. Su, H.-T. Chen, and K.-L. Wong, "Printed dual-band dipole antenna with U-slotted arms for 2.4/5.2 GHz WLAN operation," *Electron. Lett.*, vol. 38, no. 22, pp. 1308-1309, 2002.

[38] F. J. Herraiz-Martinez, L. E. Garcia-Munoz, D. Gonzalez-Ovejero, V. Gonzalez-Posadas, and D. Segovia-Vargas, "Dual-Frequency Printed Dipole Loaded With Split Ring Resonators," *IEEE Antennas Wireless Propag. Lett.*, vol. 8, pp. 137-140, 2009.

[39] M. Ricardo and et al., "Comparative analysis of edge-and broadside-coupled split ring resonators for metamaterial design-theory and experiments," *IEEE Trans. Antennas Propag.*, vol. 51, no. 10, pp. 2572-2581, 2003.

[40] W. Rotman, "Plasma simulation by artificial dielectrics and parallel-plate media," *IRE IEEE Trans. Antennas Propag.*, vol. 10, no. 1, pp. 82-65, Jan. 1962.

[41] B. Garima and et al., "Circular ring frequency selective surface: A novel synthesis technique," *IEEE Contemporary Computing (IC3), Sixth Int. Conf.*, 2013.

[42] R. J. Langley and E. A. Parker, "Equivalent circuit model for arrays of square loops," *Electron. Lett.*, vol. 18, no. 7, pp. 294-296, Apr. 1982.

[43] J. Kumud Ranjan, S. Ghanshyam, and J. Rajeev, "A SIMPLE SYNTHESIS TECHNIQUE OF SINGLE-SQUARE-LOOP FREQUENCY SELECTIVE SURFACE," *Progress In Electromagnetics Research*, vol. B, no. 45, 2012.

[44] M. Basraoui and P. N. Shastry, "Wideband, Planar, Log-Periodic Balun," *IEEE MTT-S Int. Micro. Symp. Dig.*, pp. 785-788, Jun. 1998.

[45] X. Lan, et al., "An Ultra-Wideband Balun Using Multi-Metal GaAs MMIC Technology," *IEEE Trans. Microw. Wireless Compon. Lett.*, vol. 20, no. 8, pp. 474-476, Aug. 2010.

[46] R. N. Simons, *Coplanar waveguide circuits, components, and systems*, Wiley, Ed. Vol. 165, 2004.

[47] Y. G. Kim, D. S. Woo, K. W. Kim, and Y. K. Cho, "A New Ultra-wideband Microstrip-to-CPS Transition," *IEEE/MTT-S Int. Microw. Symp.*, pp. 1563-1566, Jun. 2007.

[48] H. Shipun Anuar and et al., "Broadband microstrip-to-parallel strip transition balun with reduced size," *IEEE Microw. Conf. Proceedings (APMC), Asia-Pacific.*, 2012.

[49] P. L. Carro, J. De Mingo, P. Garcia-Ducar, and C. Sanchez, "Synthesis of Hecken-tapered microstrip to Paralell-Strip baluns for UHF frequency band," *Microw. Symp. Dig. (MTT), 2011 IEEE MTT-S Int.*, pp. 1-4, Jun. 2011.

[50] F. J. Herraiz-Martínez, G. Zamora, F. Paredes, F. Matin, and J. Bonache, "Multiband printed monopole antennas loaded with OCSRRs for PANs and WLANs," *IEEE Antennas Wireless Propag. Lett.*, vol. 10, pp. 1528-1532, 2001.

[51] J. D. Baena and et al., "Equivalent-circuit models for split-ring resonators and complementary split-ring resonators coupled to planar transmission lines," *IEEE Trans. Microw. Theory and Tech.*, vol. 53, no. 4, pp. 1451-1461, 2005.

[52] Y. Ranga, L. Matekovits, K. P. Esselle, and A. R. Weily, "Multioctave frequency selective surface reflector for ultrawideband antennas," *IEEE Antennas Wireless Propag. Lett.*, vol. 10, pp. 219-222, 2011.

[53] B. Wu, Y. Ji, and G. Fang, "Analysis of GPR UWB half-ellipse antennas with different heights of backed cavity above ground," *IEEE Antennas Wireless Propag. Lett.*, vol. 9, pp. 130-133, 2010.

[54] S. A. Hamzah, M. Esa, N. Malik, and M. Ismail, "Broadband Microstrip-to-Parallel Strip Transition Balun with Reduced Size," *Microw. Conf. Proc. APMC, Kaohsiung, Taiwan, Asia-Pacific*, pp. 172-174, Dec. 2012.

[55] (2013) Computer Simulation Technology-Microwave Studio. [Online]. http://www.cst.com

[56] A. Elsherbini and K. Sarabandi, "Compact Directive Ultra-Wideband Rectangular Waveguide Based Antenna for Radar and Communication Applications," *IEEE Trans. on Antennas and Propag.*, vol. 60, no. 5, pp. 2203-2209, May 2012.

[57] L. Ge and K. Luk, "A Magneto-Electric Dipole for Unidirectional UWB Communications," *IEEE Trans. Antennas Propag.*, vol. 61, no. 11, pp. 5762-5765, Nov. 2013.

[58] Q. Shi-Wei and Et. Al., "Wideband and unidirectional cavity-backed folded triangular bowtie antenna," *IEEE Trans. Antennas Propag.*, vol. 57, no. 4, pp. 1253-1263, 2009.